Elaboration, Propriétés optiques et applications de suspensions colloïdales de nanobâtonnets de LaPO4

Jongwook Kim

▶ To cite this version:

Jongwook Kim. Elaboration, Propriétés optiques et applications de suspensions colloïdales de nanobâtonnets de LaPO4. Matériaux. Ecole Polytechnique X, 2013. Français. NNT : . pastel-00948255

HAL Id: pastel-00948255
https://pastel.hal.science/pastel-00948255

Submitted on 18 Feb 2014

Thèse présentée pour obtenir le titre de

DOCTEUR DE L'ECOLE POLYTECHNIQUE

Spécialité : Science des Matériaux

Par

Jongwook KIM

Elaboration, optical properties, and applications of colloidal suspensions of LaPO₄ nanorods

Soutenue le 26 septembre 2013, devant le jury compose de:

Corinne Chanéac	Collège de France	Rapporteur
Franck Artzner	Université de Rennes	Rapporteur
Jean-François Tassin	Université du Maine	Examinateur
Michel Lequime	Institut Fresnel, Marseille	Examinateur
Khalid Lahlil	Ecole Polytechnique	Examinateur
Jacques Peretti	Ecole Polytechnique	Examinateur
Thierry Gacoin	Ecole Polytechnique	Directeur de thèse

Acknowledgements

First and foremost, I express my sincerest gratitude to my advisor, **Thierry Gacoin**. A strong motivation for me to come back to France and start my thesis at PMC was the memory of my Master internship with him. He had let me learn how to do "re-search", and had shared an exceptionally huge amount of time discussing together to complete a meaningful project on Plasmonics in a limited time. Since I returned to the group, he has given me such a considerate support during the whole three years of my thesis study. Also, he has trusted me as a colleague working together and as a dear friend. My dissertation is a fruit of the uncountable moments brainstorming ideas, developing arguments, and writing papers always together with Thierry.

The same gratitude is extended to my co-advisor, **Jean-Pierre Boilot**. His insightful guidance has led me to find the right direction and often let me step back and contemplate on the critical issues that I had missed. I might become an engineer but not a scientist without his help. Thanks also to his warm words and humors that have constantly encouraged me. I wish to thank **Khalid Lahlil** who always stayed beside me handing down a lot of chemical synthesis skills. The good beginning of this thesis was attributed to his previous work developing the nanorod synthesis methods also with Rodolphe Deloncle and Sara Belei. I must express my heartfelt thanks to **Jacques Peretti** who has gladly tutored me all about optics. Most of the experiments, calculations, and the application studies could have been developed through his instructive guidance. And a special thanks goes to **Lucio Martinelli** who has been immensely helpful for setting-up the optical experiments.

I would like to express my deepest appreciation to **all the research staffs of the PMC laboratory**. I regret I cannot list all the names here because I got so much help and inspiration from too many of them. Everyone readily and kindly invested time and shared ideas when I asked help. What I have learned at PMC is not only the theoretical knowledge and the experimental techniques. But it has been a joyful and exciting experience working in the same place with them learning how they cooperate together, how they sacrifice for the colleagues especially for the young trainees like me, and how long they keep their curiosity and enthusiasm for research until even after the retirement. I could not have asked a better model of a research family. And I could establish a very positive vision for my future as a scientific researcher thanks to all of them.

I am also grateful to **Michiel Hilbers** and **Fred Brouwer** at Amsterdam University for their thoughtful collaboration and allowing me to learn and use the powerful laser confocal microscope, to **Charles Baroud** and **Etienne Fradet** at LadHyX for the friendly discussions and experiments together on the microfluidic measurement, to **Alexandrou Antigoni** at LOB for her guidance on the fluorescence optical microscopy, and to **Eric Grelet** at CRPP Bordeaux for his instruction when studying and experimenting on liquid crystal systems during the first period of my thesis.

Table of Contents

Introduction

On the earth, there exist thousands of mineral compositions and as many different physical, chemical, and mechanical properties they consist of. Minerals have been exploited to utilize such a variety of properties for making proper materials and devices. A fundamental difference of minerals compared to amorphous inorganic or organic materials is that they have a crystalline atomic structure. A certain crystallinity of a mineral composition provides a unique physical property that is often anisotropic along the crystal axes. Polarization, birefringence, ferromagnetism, and ferroelectricity are representative examples of such directional properties obtained by crystalline materials. An important condition for using the anisotropic properties of minerals is that they should be a single crystal that is hard to obtain. Polycrystals, amorphous crystals, or bulk powders and solutions of small crystalline particles lose their anisotropic properties on the macroscopic scale and only exhibit isotropic characteristics due to the random orientation of their building blocks. Many interesting directional properties of minerals have been overlooked for this reason. If one can organize the orientation of the tiny single crystals constituting such bulk materials, it would be possible to reveal and practically use their anisotropic properties. Furthermore, if such collective orientation can be actively controlled in the soft state, it would also be possible to modulate such anisotropies reversibly. The figure below schematically shows this idea that many directional optical, electrical, and magnetic properties could be manifested from organized structures of crystalline particles.
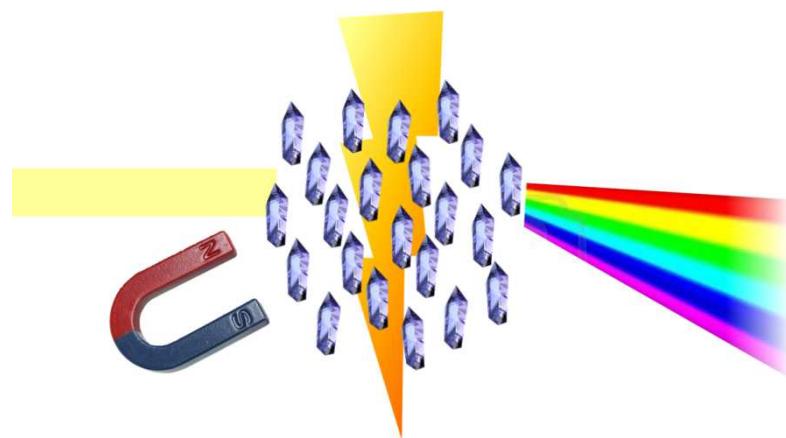
Recent development of nanotechnology has provided a lot of solutions for the fabrication and assembly of nanoscale materials. Now it is available to synthesize nanoparticles with various chemical compositions and different shapes and to make their organized structures. Nevertheless, the way of assembling mineral nanocrystals orienting their axes all together is still to be explored. Actually, many researches have focused on exploiting the new properties

originating from the size and the organized structure in the nanoscale, but without paying enough attention to the intrinsic anisotropy of the nanoparticles. Moreover, most self-assembly techniques are oriented to make a solid organized structure relying on the solvent depletion process that is irreversible. In this thesis, we attempt to control the collective orientation of mineral nanoparticles in a reversible manner to make maximum use of the anisotropic properties in addition to what may come from the organized structure. Mineral nanocrystals having both physical and morphological anisotropy are synthesized in form of colloidal suspensions. The oriented-assembly of these nanocrystals is obtained while maintaining the soft liquid state. This provides an example of how resulting anisotropic properties can be applied in practical devices and scientific studies.

For that purpose, we focused on the liquid crystalline (LC) behavior of colloids. LC behavior – the spontaneous orientation of the anisotropic constituents involved by their thermodynamic interactions – has been observed from diverse liquid substances composed of organic molecules, colloids or biological systems. By means of LC behavior, colloidal mineral nanocrystals get a chance to be organized in the soft liquid state. In chapter 1, a brief theory and some experimental examples of mineral liquid crystals (MLC) are introduced. Looking deeply into the existing MLC materials, it is examined how to design a new system making up for the weak points of MLCs that had limited their real application. The base material of this project selected after a tentative experimental study is lanthanum phosphate ($LaPO_4$) nanorods, a rare-earth mineral compound displaying interesting optical properties. In Chapter 2, an elaborate experimental work to prepare LC suspensions of colloidal $LaPO_4$ nanorods is presented. With the objective of making a well-performing LC system, i.e. obtaining a highly organized and controllable soft state, the synthesis method is carefully optimized. Then the analytic studies on this new MLC system are followed verifying its capability for applications in optical devices. The main anisotropic property of our material is birefringence, which enables to modulate the polarization of light. Chapter 3 is dedicated to demonstrate how to observe, understand, and make use of the large birefringence exhibited from the oriented $LaPO_4$ nanorods structures. As it was aimed, an active electro-optical device is made to reversibly control the orientation of particles thus to adjust the amount of birefringence as intended. A new method of directed-assembly of nanorods is also presented by using a phase tuned colloidal suspension. The observed results, with some unexpected features, are examined by a theoretical model reporting a new aspect of the organized system combining the intrinsic and structural anisotropies together.

Another interesting and less common anisotropic property of the $LaPO_4$ system is polarized photoluminescence. Indeed, $LaPO_4$ is an efficient host of other luminescent lanthanide elements such as europium (Eu), cerium (Ce), and terbium (Tb). In Chapter 4, we find out that Eu doped $LaPO_4$ nanorods exhibit photoluminescence that is polarized in a peculiar way distinct to the polarized emission of other luminescent materials. Thanks to the orientation control achieved ahead, the unique polarized luminescence of $LaPO_4$ nanorods could be observed and analyzed in details. As a final task of this thesis research, a novel method to utilize it as a marker of orientation and flow measurement is investigated.

Chapter 1

Liquid Crystalline Assembly of Colloids

Self-assembly of micro- or nano-sized colloidal particles by their packing entropic dynamics during the depletion of solvent has been thoroughly studied since decades. Besides, another interesting self-assembling phenomenon that is independent of the solvent depletion, i.e. maintaining the soft liquid state, is the liquid crystalline (LC) assembly. LC assembly has been paid much less attention in the field of colloid science, and is a main issue of this thesis study. Thanks to the fact that it is only due to the thermodynamic interactions between freely-moving particles inside the liquid medium, LC assembly is reversible and has a chance to be actively controlled involving light transmission control by an external electric field. Basically the LC systems focused on in this study is only the lyotropic colloidal LCs that have a distinct difference with the thermotropic LCs composed of anisotropic organic molecules. **Figure 1.1** schematically shows the arrangements of rod-shaped particles in a free-space with different volume fractions (Φ). In the lyotropic LC system, such anisotropic particles spontaneously align when they are confined in a limited space with Φ over a certain range forming nematic (with the orientational order) and even columnar (with both orientational and positional order) phases. It is true that we are more familiar with the organic LCs than colloidal LCs because organic liquid crystals are now deeply penetrated in our daily lives in form of electronic LC display (LCD) devices. Colloidal LCs, especially mineral liquid crystals (MLC), are relatively less studied in the materials research of today. Why? The reason is discussed in this chapter with some representative examples of natural and synthetic MLCs that exhibit satisfactory LC behavior. Then it is discussed how the long-lasted limitations of MLCs could be overcome using the methods and materials that are carefully developed in this thesis research.
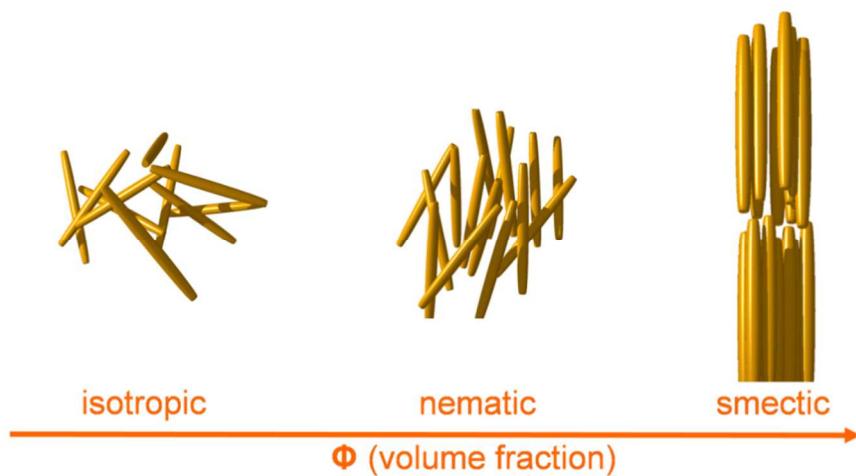
Figure 1.1. Phase transition of hard rod system according to the volume fraction change.

1.1. Mineral Liquid Crystals

In the early 20th century, Zocher[1] demonstrated that LC behavior could be observed in mineral colloidal suspensions of vanadium pentoxide ribbons. And the pioneering theoretical work of Onsager[2] provided the explanation on the spontaneous nematic ordering of long hard rods in the middle of the 20th century opening a large field of investigation. In addition to fundamental issues related to self-organization of nanoparticles and their LC behavior, research on inorganic compounds opens the way toward devices that would take benefit from intrinsic properties of minerals such as large refractive index, absorption dichroïsm, ferroelectricity or ferromagnetism... Although still limited to a few number of compounds, some colloidal suspensions of anisotropic inorganic nanoparticles are now known to exhibit LC behavior such as nematic ordering, thus being referred to as mineral liquid crystals (MLCs).[3-4] During the last two decades, Rutile[5-6], Boehmite[7-8], Goethite[9-12] and CdSe/CdS quantum dots[13-15] in rod-like geometry, and Gibbsite[16-18], Laponite and Bentonite[19-20] in shape of clay platelets have been the subject of numerous investigations. In contrast to the vast use of organic LCs today, practical applications of those MLCs are still very limited due to the difficulty in the synthesis of suspensions with appropriate properties up to high particle volume fraction. Although different MLC systems have already been studied as listed above, there is still a large place for research on new compounds with optimized properties in terms of LC behavior, dielectric constant and anisotropy, and optical transparency, the latter concerning color and light scattering properties up to high volume fractions.

1.1.1. Onsager's hard rod model

LC behavior of colloidal systems can be explained in a purely entropic regime – as a sort of lyotropic system – because colloidal particles have their size typically in the range of several tens of nanometers to several micrometers. In this size range, particles are 'too heavy' to

exhibit significant thermal effect which is distinct to the organic LCs that are mostly thermotropic systems. A simple and robust model which predicts such a lyotropic phase behavior of colloidal systems was proposed by Lars Onsager in 1949.[2] This conceptual model system is composed of hard rod without interaction with each other and confined in a limited volume of space. This theory considers a competition between two entropic terms, one of which is orientational entropy and the other is packing entropy (**Figure 1.2**). In the isotropic phase, rods are randomly angled with each other so that the orientational entropy increases. However, a large volume around a rod is excluded ($V_{ex} = 2DL^2$) from the center-of-mass of another rod approaching it decreasing the packing entropy. On the contrary, in the nematic phase where the rods are oriented parallel decreasing the orientational entropy, the excluded volume of a rod becomes very small ($V_{ex} = \pi D^2L$) increasing the packing entropy. The hard rod system undergoes isotropic↔nematic phase transition as shown in **Figure 1.2** involved with the trade-off between the two entropic terms that are determined by the rods' spatial density in volume fraction (Φ). Onsager's mathematical description concludes a simple relation noted as $\Phi_{iso\text{-}nem} \sim 4D/L$, predicting inversely proportional relation between the phase transition density ($\Phi_{iso\text{-}nem}$) and the rod aspect ratio (L/D).
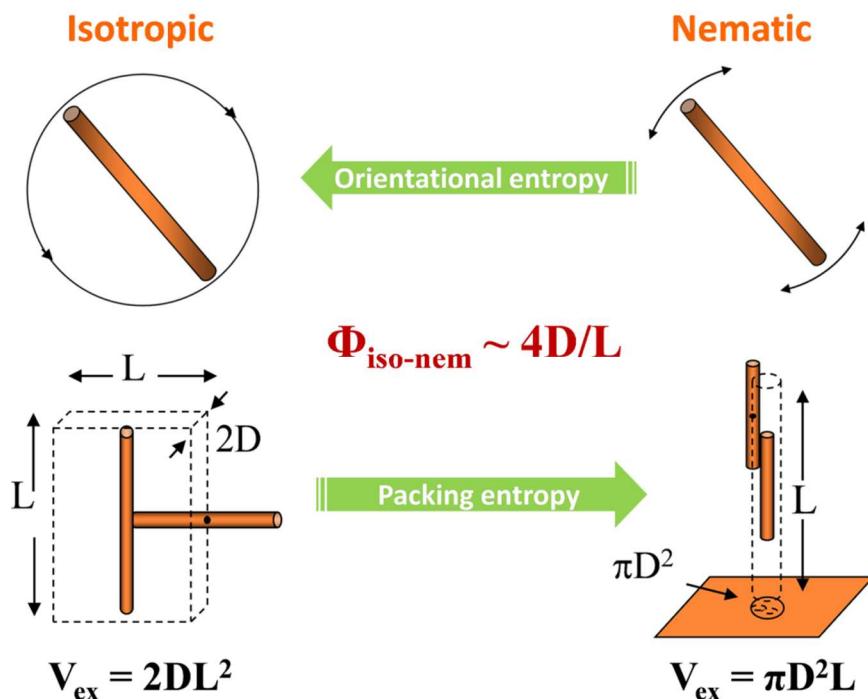
Figure 1.2. Schematic illustration of the orientational entropy and packing entropy of hard rod in the isotropic and nematic phases.

In real systems, composed of colloidal particles dispersed in a solvent, electrostatic interactions between charged colloidal particles make the phase transition behavior more complicated than in the simple hard rod model. Nevertheless, many colloidal LC systems have been shown to qualitatively follow this theoretical model, and the deviating values of

$\Phi_{iso-nem}$ could be corrected by introducing polydispersity and the effective diameter of charged rod (D_{eff}) in the calculation.[2]

1.1.2. Gelation vs. LC behavior

If only the Onsager's theory is considered, one can expect it easy to prepare liquid crystalline suspension of anisotropic colloidal particles simply by increasing the particle density. However, it is not true because the model is applicable in the real system only when the particles do not aggregate. Regardless of the anisotropic geometry, colloidal particles in a liquid medium are interacting with the attractive van der Waals force[21] and the electric double layer repulsion. DLVO theory (named after Derjaguin, Landau, Verwey and Overbeek) describes the balance between these forces dependent upon the ionic force of the medium.[22] In general, particles aggregate fast when the double layer repulsion is screened by high ionic force of the medium surrounding them. At low ionic force, there exist a substantial repulsion between particles and the aggregation rate is limited by the probability for two particles to overcome this repulsive barrier by thermal activation.[23] A stable colloidal suspension is prepared only when this rate of aggregation is kept very (or infinitely) long enough to make the suspension stand well-dispersed for apparently long time. In case where particles have anisotropic form and are concentrated to incorporate LC phase behavior, maintaining this stable regime becomes extremely difficult[24] and gelation is what can be more generally observed from the real systems as many examples are shown in **Figure 1.1**.[25]
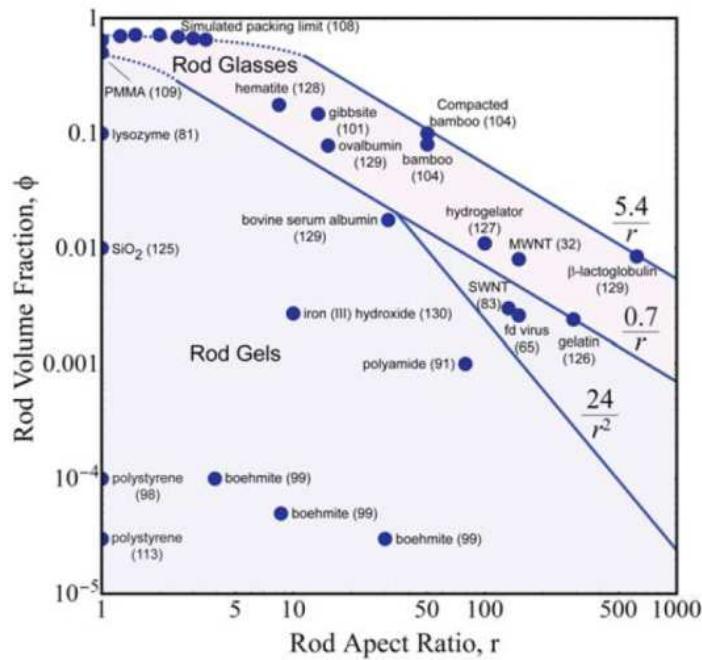
Figure 1.3. Map of the volume fraction, aspect ratio space of rod suspensions, gels and glasses reported. *Figure taken from the reference paper* [25].

Indeed, the rod percolation threshold density implying the gelation point of a colloidal rod suspension is described as $\Phi_{percolation} \sim 0.7D/L$[26-27]. This is 6 times lower than the LC phase transition density ($\Phi_{iso-nem} \sim 4D/L$) by the model of Onsager.[2] This is the reason why there exist a very few number of colloidal systems where LC behavior is not interrupted by gelation that quenches the mobility of individual particles. Thus to make a LC system, an outstanding colloidal stability accompanied by a high interparticle repulsion is essential, or the particle surface should be protected by a functionalized molecular layer that provides steric hindrance in the region where the attractive interaction dominates. Some successful examples of MLCs reported satisfying these conditions are introduced at below.

1.1.3. Synthetic mineral liquid crystals

Vanadium pentoxide ribbons (V_2O_5)

Aqueous colloidal suspension of V_2O_5 ribbons is the firstly reported mineral liquid crystal system by Zocher[1] in 1925, at the same period when the organic liquid crystalline molecules were discovered. Using polarization microscopy, he observed small birefringent domains in the V_2O_5 suspension and inferred the aligned structure of anisotropic particles inside these domains, which are called "tactoids". V_2O_5 have a great potential in the field of electrochromism, sensors, and batteries. Therefore, controlling their anisotropic electronic properties through the liquid crystalline property in the soft suspension had stimulated many researchers during the last decades.[3, 28]
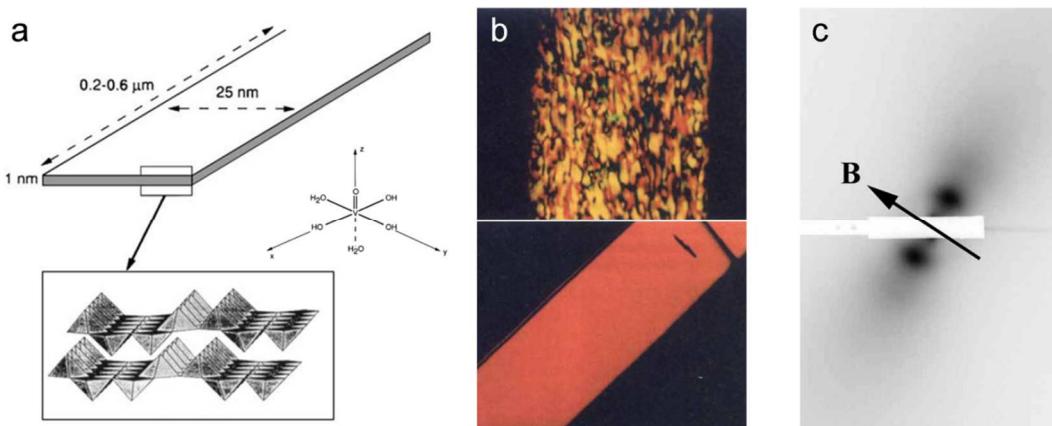
Figure 1.4. (a) Schematic molecular geometry of V_2O_5 ribbons. (b) Polarization optical micrographs of the aqueous V_2O_5 ribbon suspension at rest (top) and under applied magnetic field (bottom) (c) SAXS pattern of the magnetically aligned phase *Figure taken from the reference paper* [3]

V_2O_5 ribbons are very thin molecular layer as shown in **Figure 1.4.a**. Due to such a highly anisotropic geometry, their aqueous colloidal suspension shows isotropic-nematic phase transition at low volume fraction, Φ at ~0.7%. In the spontaneously aligned nematic phase, the mesoscopic nematic domains viewed in the macroscopic scale are randomly oriented rendering the typical Schilieren texture as shown in **Figure 1.4.b**-top. When $\Phi > 1.5\%$, sol-gel transition occurs in this suspension and it turns into a birefringent gel phase where the individual particles lose their mobility. At the density between these values ($0.7\% < \Phi < 1.5\%$) the purely nematic suspension maintains fluidity, so that the interesting re-alignment effects under external magnetic field are observed. **Figure 1.4.b**-bottom shows the single nematic domain induced by the external magnetic field in the same sample shown in the top image where the orientation was initially textured. It was reported that a magnetic field ~1T was sufficient to make such a fully aligned single domain. And this single domain nematic sample is well suited for small angle X-ray scattering (SAXS) analysis, which has long been a powerful technique to study mineral liquid crystals.[29-30] The SAXS pattern in **Figure 1.4.c** is an evidence of the purely nematic phase of the V_2O_5 ribbon suspension as no Bragg peaks or diffraction lines were observed.[28]

Goethite (α-FeOOH)

Goethite particles have been widely used as yellow color pigments since 30000 years ago such as in cave painting. When tuned as LC suspension, they also show a very interesting phase behavior and magnetic field-induced alignment.[3, 9-10] In spite of the high polydispersity of the synthetic goethite particles in rod-like geometry (**Figure 1.5.a**), it has been reported that they form highly positionally ordered LC phases that are intuitively hard to be formed in a polydisperse system. **Figure 1.5.b** shows a dense colloidal suspension ($\Phi=16\%$) of goethite rods prepared in a capillary tube, with which three distinctly different birefringent phases are separated by sedimentation.[12] Here, the top layer (I) is a typical nematic phase, but the two bottom layers are respectively smectic (II) and columnar (III) phases.
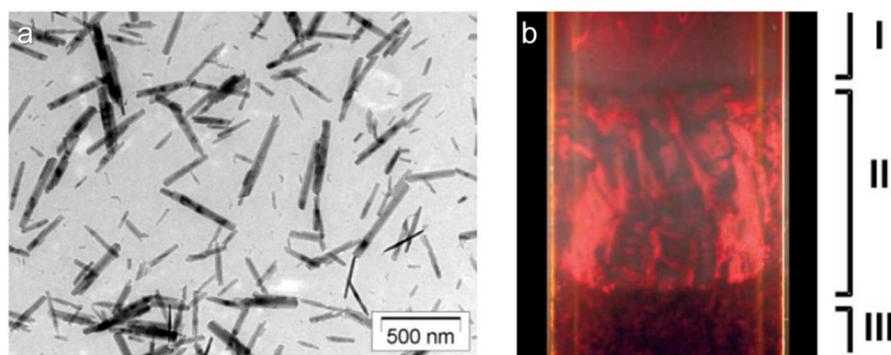
Figure 1.5. (a) TEM image of goethite nanoparticles. (b) Phase separation in a capillary tube of aqueous colloidal goethite nanoparticle suspension into nematic-I, smectic A-II, and columnar-III phases. *Figure taken from the reference paper* [12]
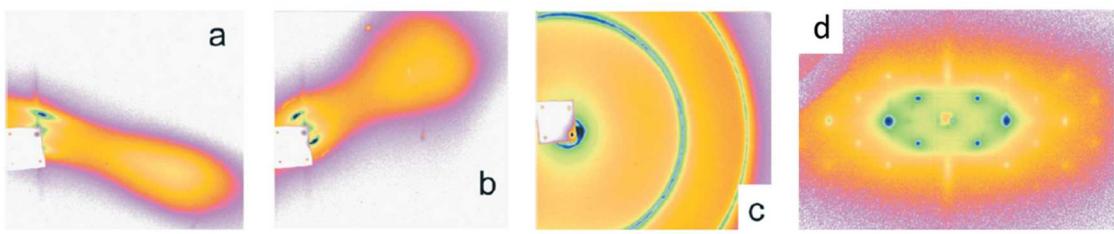
Figure 1.6. SAXS patterns of different liquid crystalline phases of goethite nanoparticle suspension: (a) nematic, (b) smectic-A, (c) columnar, (d) 2D columnar. *Figure taken from the reference paper* [12]

Polarization optical microscopy is convenient to directly observe aligned LC phases, however, it is not appropriate in distinguishing different ordered phases. As stated above, SAXS is a powerful method in the case of identifying these LC phases such as nematic, smectic and columnar. Distinct SAXS patterns from the goethite suspension sample are shown in **Figure 1.6**, which were obtained from a single domain samples adjusted by applying external magnetic fields of less than 1 tesla.[11]

Rutile (TiO₂)

TiO$_2$ particles have widely been used as white color pigment like with the above example of goethite as yellow pigment. In the recent decades, TiO$_2$ have become one of the most important materials in high-tech industries due to its photocatalytic performance such as in solar cells. For this reason, many synthetic methods of TiO$_2$ nanoparticles in different form and crystalline structure have been developed.[31-33] There exist three main types of crystalline structure of TiO$_2$ nanoparticles which are anatase, brookite, and rutile. Rutile nanoparticles usually have long rod-like geometry due to the anisotropic crystal growth rate as shown in **Figure 1.7.a**.[5]
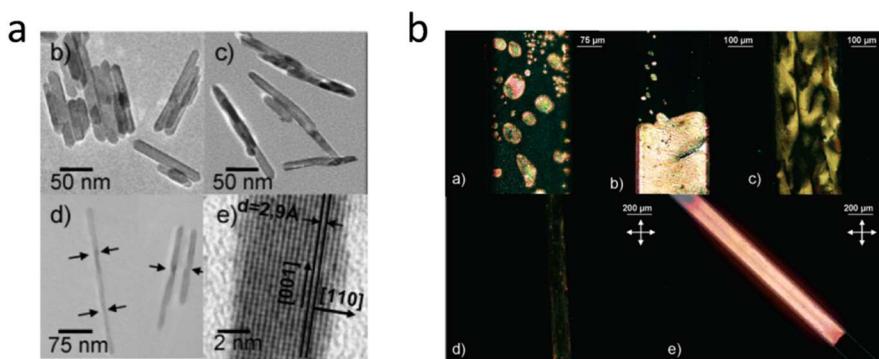
Figure 1.7. (a) TEM images of rutile nanorods. (b) Phase separation of aqueous colloidal rutile nanoparticle suspension in a capillary tube and the directional birefringence from the shear-aligned state in a flat capillary tube. *Figure taken from the reference paper* [5]

When carefully synthesized and densely dispersed in water, rutile nanorods also show LC behavior such as phase transition and separation (**Figure 1.7.b**). Dessombz *et al*, have shown these nanorods could have been aligned applying shear force on the suspension, and made an aligned film of rutile nanorods by spin-coating as shown in **Figure 1.8.a**.[5] Photocatalytic ability of this film was examined by monitoring the decomposition of methylene blue under polarized UV light (**Figure 1.8.b**). It was found that the photocatalytic ability was the most efficient when the irradiation was polarized along the quadratic axis of the rutile nanorods (**Figure 1.8.c**).[6] This is a good example of exploiting a useful anisotropic physical property from a mineral liquid crystal system.
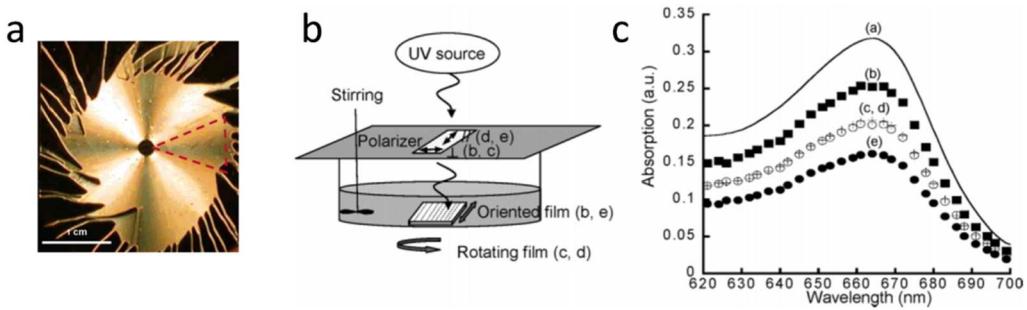
Figure 1.8. (a) Spin-coated film of radially aligned rutile nanorods. (b) Schematic of aniotropic photocatalytic property study by measuring the UV light absorption of methylene blue solution with an aligned rutile nanorods film. (c) Photocatalytic absorption spectra according to the angle between the polarizer and the rod orientation direction. *Figure taken from the reference paper* [5]

Quantum dots (CdS/CdSe)

Synthetic method and the efficient luminescent properties of semiconductor quantum dots were discovered in the end of 20th century.[34] These inorganic crystals composed of CdS/CdSe have a great potential in all the fields involved with luminescence such as display technology and bio-markers in which there already exist many applied technologies commercialized. These nanocrystals can be synthesized in shape of highly monodisperse rods with a very tiny size – typically ~10nm in length – as shown in **Figure 1.9.a**.[13] Such a small size and monodispersity is exceptional compared to other inorganic crystalline nanorods. And thus it may be interesting in the aspect of LC behavior considering the aspect ratio-dependent model of hard rod system and thermotropic property of small molecular systems. LC behavior of these quantum dot nanorods are clearly observed as shown in **Figure 1.9.b**. Distinct to the other mineral liquid crystal systems, the LC phase transition was found to be dependent both upon the particle density (Φ) and the temperature due to their small size.[15] Therefore, it is a both thermotropic and lyotropic LC system.
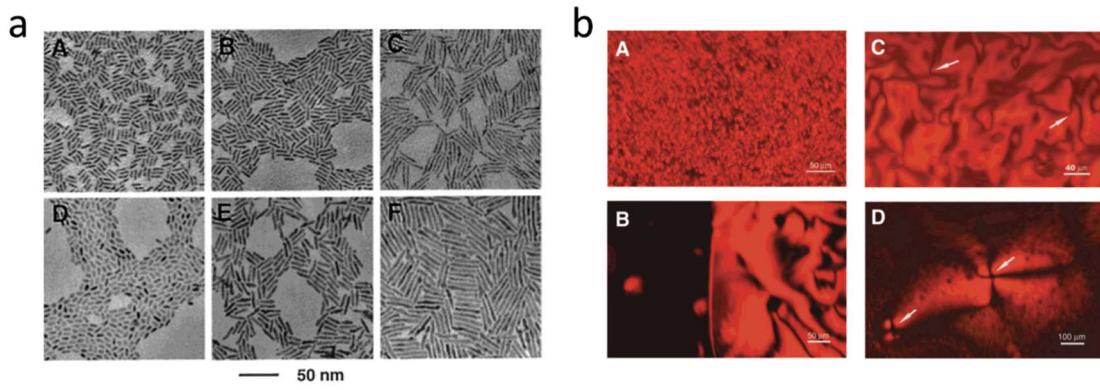
Figure 1.9. (a) TEM images of monodisperse CdSe nanorods with different aspect ratio. (b) Liquid crystalline phase textures of CdSe nanorod suspension observed under polarizing microscope. *Figure taken from the reference paper* [13]

Controlling the orientation of quantum dot nanorods using LC behavior is interesting because they exhibit anisotropic non-linear optical properties. Photoluminescence (PL) and electroluminescence (EL) of quantum dot nanorods are linearly polarized[35]. Therefore, if the orientation of these particles are controlled using their LC property, the bulk luminescence could be modulated. It can also be possible to increase PL or EL efficiency when making quantum dot based display devices which is an emerging issue of today. Such an idea of controlling polarized luminescence of nanocrystals in the bulk scale by using the organized LC phase is one main concept of this thesis study, and will be discussed in Chapter 4.

1.1.4. Natural samples

Tobacco Mosaic Virus (TMV)

TMV is the firstly discovered virus that has a shape of rigid nanorod with a length of ~300nm and a diameter of ~18nm due to its single stranded RNA structure. For many reasons, e.g. easiness of gram scale production and non-infectiousness to animals, it has a great impact in many fields of scientific research including the studies on the colloidal liquid crystalline (LC) system. It can be said that the pioneering experimental study on the colloidal liquid crystals had been led using TMV decades before most studies on synthetic mineral liquid crystals.[36] And it has been known as a representative model system following very well the Onsager's hard rod model in detail.
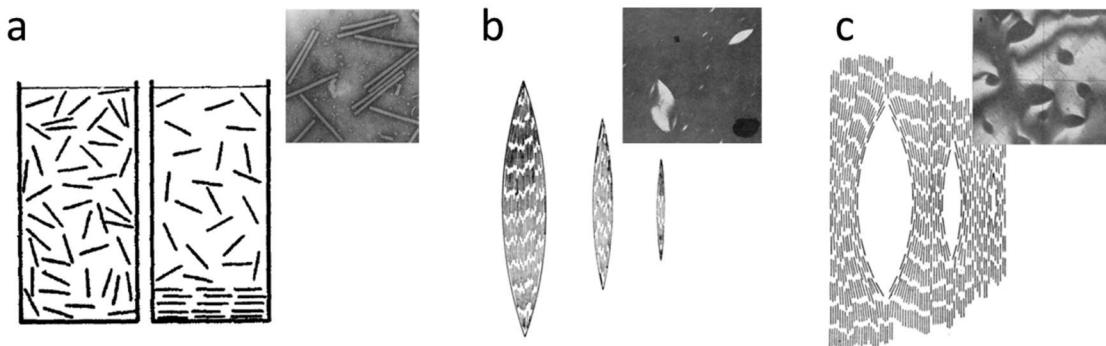
Figure 1.10. (a) Schematic single phase and separated two-phase suspensions of TMVs and the SEM image of TMVs-inset. (b) Schematic assembly and of TMVs in the tactoid structure and its optical micrographs, (c) The same in the anti-tactoid structure. *Figure taken from the reference paper* [36-37]

The SEM image in **Figure 1.10.a** shows the rod-like shape of TMVs. The length of TMV is more or less polydisperse, yet the diameter is almost the same for all viruses as it is defined by the helical structure of RNA. Though it is a biological system, the colloidal behavior of TMV suspension is alike with that of rigid particles. The surface charge of these viruses reaches a long range enabling well-dispersed suspension in a pH-tuned suspension. Moreover, TMVs have very high dispersion stability even re-dispersible after close packing in the dried state, which is hardly possible in mineral systems. The density-dependent two-phase (iso-nem) separation of the system was observed and analyzed together with the X-ray analysis on the organized phases providing the experimental verification of the Onsager's theoretical model studied in the same period (in 1950s). Many detailed researches about the lyotropic LC behavior have been followed using TMVs until today.[38]

Indeed, the size and shape of TMV is very alike with the $LaPO_4$ nanorod demonstrated in the next chapter. Knowing that TMV is one of the best colloidal LC systems, it could be estimated at the beginning of this thesis that $LaPO_4$ nanorod suspension might also show prominent LC behavior. This was finally found to be true and will be discussed in the next section.

Clays

Various types of clay particles such as montmorillonite family have a thin layered structure. These clays have a unique swelling and exfoliation property and that is often used in many industrial products such as paints, softeners, and composite materials.[39] The LC behavior is not only limited to rod-shaped particles but also available for these nano-sheets. Langmuir observed that clay suspensions separate into isotropic and birefringent phases. However, it has long been unclear if this birefringence came from the spontaneous nematic ordering. In contrary to the rod particle suspensions, strong gelation property of clay suspensions make themselves undergo sol-to-gel transition before observing iso-nem transition on the whole

ionic force range. It was in the recent period that researchers clearly observed the LC organization of clay particles from bentonite, laponite[3, 40], and nontronite[41] suspensions.
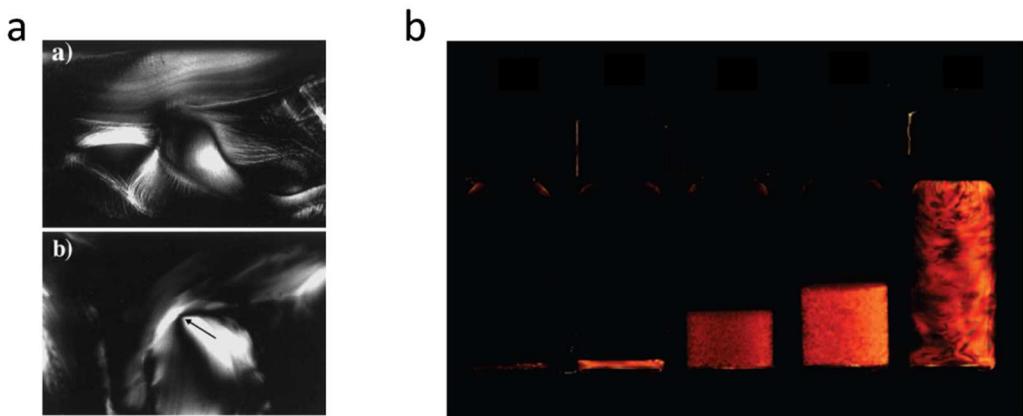
Figure 1.11. (a) Polarization optical micrographs of aqueous bentonite suspension in nematic phase. (b) Bulk phase separation of aqueous nontronite suspension with a gradual increase of particle concentration (from 0.5%-left to 1%-right). *Figure taken from the reference paper* [3, 41]
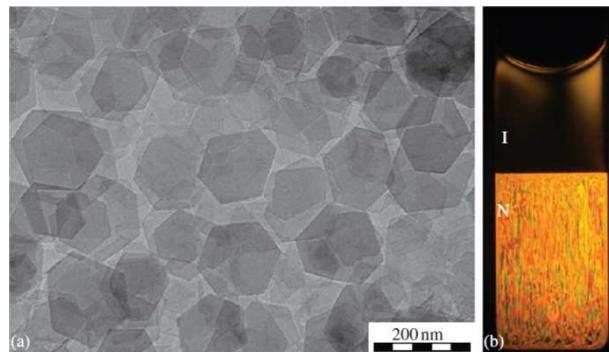
Figure 1.12. SEM image of synthesized gibbsite particles and their phase separated suspension. *Figure taken from the reference paper* [18]

On the other hand, synthetic clays that have a form of platelets exhibit more remarkable LC behavior, of which gibbsite is one representative example. As the synthetic method is engineered to obtain much less polydisperse particles than natural clays, these nano-platelets show a prominent LC behavior as shown in **Figure 1.12**.[17-18, 42-43]

1.2. Strategy towards device application

In the general aspect of the assembly of anisotropic nanoparticles, a variety of synthetic methods and assembling techniques have been developed until today. Now a remaining task

will be to scale-up the assembly of these nano-objects beyond the macroscopic device area, and to find the intelligent way of utilizing the assembled structure. In this regard, there still exist so many technical problems and a lack of real applications into devices. The exemplary materials listed above are all representative colloidal liquid crystalline systems elaborated by the pioneers of MLCs. If there is one thing left to be desired, it would also be their applications for practical devices. It is true that very few and limited applications have been realized using those materials in spite of the long history of either theoretical or experimental researches on MLCs. The first reason for it would be the rapid development of organic LC materials in recent decades and their commercialization for many practical devices such as liquid crystal displays (LCD). The key property of LCs – generating birefringence to modulate light polarization – was more easily achieved with organic LCs than with MLCs because they are pure molecular systems. On the other hand, mineral colloids have some disadvantageous intrinsic properties such as the difficulty in synthesizing monodisperse particles and in stabilizing their dispersion which have long limited the application of MLCs. Moreover, the size of the particles often larger than the visible wavelength gives rise to a considerable loss of light and low optical contrast by light scattering. At this point, it is required to grasp the weak points of MLCs and to overcome them by materials engineering ultimately to disclose the unique advantageous anisotropic properties of organized mineral systems that are too valuable to be abandoned.

1.2.1. Characteristic requirements

Provided the anisotropic morphology of particles, the most critical factor for a successful preparation of colloidal LC suspension is the dispersion of particles. For the satisfactory dispersion of the final product suspension, first, the particles must not be aggregated during their synthesis step. Once particles are aggregated during synthesis they would very hardly get chance to be dissociated afterward because crystallization reaction between the surfaces of closely associated particles make them chemically fused. Secondly, the long term dispersion stability should be maintained. Colloidal stability depends totally on the surface chemistry and the ionic composition of the dispersion medium. There exist generally two ways to control this: (1) optimize the effective surface charge density of bare particles by controlling ionic concentration of the medium, (2) functionalize the particle surface with charged surfactants, ligands, or polymers to provide additional interparticle repulsion or steric hindrance.

As it is a key property of LC systems in general, obtaining and controlling large amount of birefringence by the organized structure was a main objective launching this project. Also, high transparency and low scattering aspect at the target wavelength (λ) should be accompanied to do not lose the incident light to be modulated. Structural form birefringence is promoted by the high aspect ratio of the particle shape. Thus long rod-like morphology is favorable. Transparency depends on the light absorption determined by the band-gap of the material, so high band-gap mineral material would effectively exclude absorption loss. Scattering strongly depends on the size of the particles as Rayleigh scattering intensity is proportional to the 6th power of the particle size. Thus the size of the long-axis of the particles

should be smaller than λ. Mono-crystalline structure of each individual particle would be also helpful for minimizing scattering loss. Moreover, it would eventually be beneficial if some other physical properties other than birefringence can be exploited by using inorganic anisotropic particles. Therefore, additional anisotropic properties originating from the crystalline structure would be welcomed.

1.2.2. Searching for a proper material

Previously to this thesis study, a post-doctoral research (*by Dr. Rodolphe Deloncle*) had been conducted to find a proper material that satisfies the above characteristic requirements. This work is briefly summarized here to explain why lanthanum phosphate ($LaPO_4$) was finally selected at the end of his post-doc study for being continued in this thesis study.

Goethite (α-FeOOH), Boehmite (γ-AlOOH), and Rutile (TiO_2)

At the beginning, these three mineral colloidal particles that had already been reported as MLC materials were tested as there synthetic method had already been revealed. Firstly Goethite particles were synthesized of $Fe(NO_3)_3$ precursor solution following the method reported by Thies-Weesie et al.[44] The method was easily reproducible and the synthesized particles had a lath-like form with L (length) = 150nm, W (width) = 20nm, and D (thickness) = 10nm (See **Figure 1.13**). As described above, these particles exhibit strong paramagnetic property thus being capable to be oriented under external magnetic field. However, these particles were not appropriate for general optical applications because they had a yellow color due to the significant absorption in the visible range. Thus goethite was abandoned.
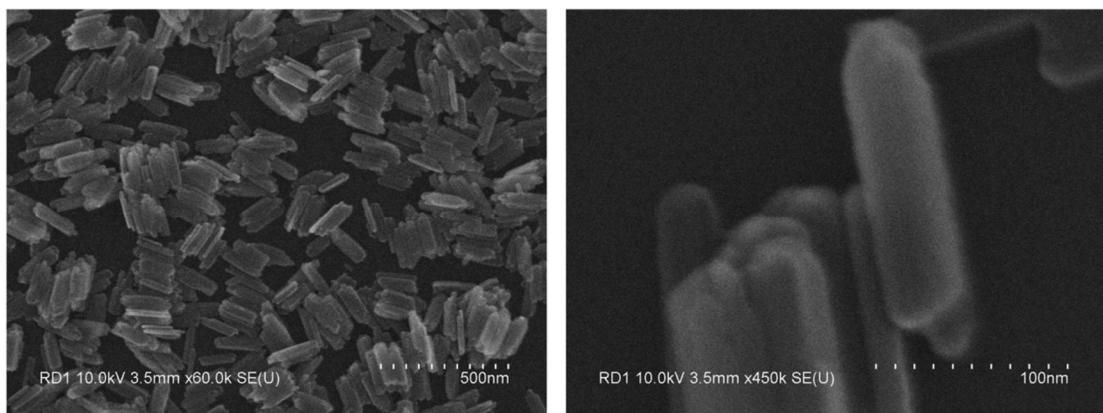
Figure 1.13. SEM images of lath-like Goethite particles synthesized following the method described in the reference [44].

The secondly tested material was boehmite. It was verified from the beginning that Boehmite nanoparticles without impurity have no visible color. Three different synthetic methods reported were tested: (1) rapid hydrothermal synthesis, (2) slow hydrothermal synthesis, (3) solid-phase hydrothermal synthesis. The first method was abandoned because the product particles size was too small. The second method following the report of Buining and Lekkerkerker[45] was quite reproducible and almost the same rod morphology that was shown in their paper was obtained (**Figure 1.14.a**). The third solid-phase method[46] had also given rod shaped particles very efficient for gram-scale mass production (**Figure 1.14.b**). A great advantage of slow hydrothermal synthesis was that nanorods after the synthesis were not aggregated as shown in **Figure 1.14.a**. A dilute colloidal suspension (Φ < 0.5%) have shown flow birefringence and a substantial transparency, a sign for possible preparation of an MLC system with it.
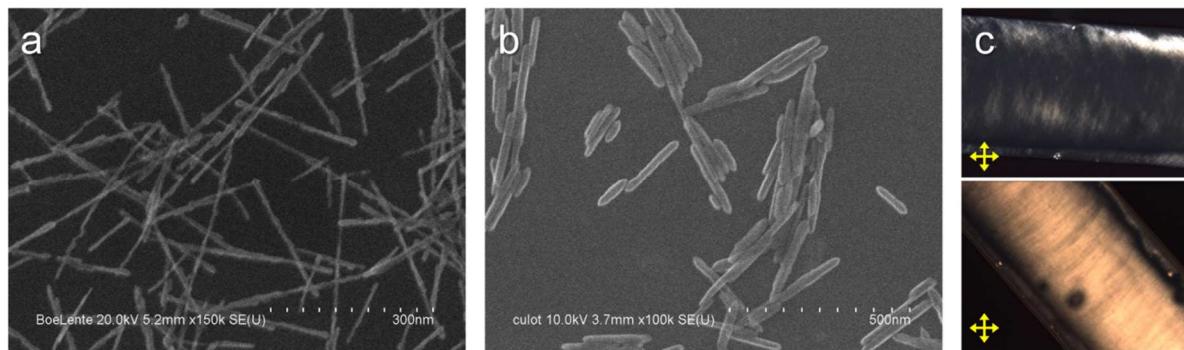
Figure 1.14. SEM images of boehmite nanorods synthesized by slow hydrothermal method[45]-(a) and solid phase hydrothermal method[46]-(b). (c) Polarization optical micrographs of the (a) suspension in a glass capillary tube placed parallel and 45° to the polarizers.

However, a problem arose from the colloidal dispersion stability. As already reported, this boehmite suspension has a strong tendency to rapidly form gels due to the electrostatic interactions together with the high aspect ratio of rods.[27, 47] Much effort was put to avoid this problem by surface functionalization using diverse polymers and silanes such as poly-vinylpyrrolidone (PVP) or 3-methacryloxypropyl trimethoxysilane (TPM), but we could not succeed to make a stabilized suspension of individually dispersed boehmite nanorods without gel formation. Besides, it was possible to make dense suspensions of somewhat aggregated boehmite nanorods by diluting the centrifuged rod gels. Though the dispersion quality is poor, permanent birefringence due to the LC nematic orientation was observed as shown in **Figure 1.14.c**. It is shown in this photo the nematic phase aligned toward the capillary flow in the tube providing directional birefringence along the tube. Anyway, boehmite was also abandoned because of the poor dispersion quality, very low observed birefringence from nematic suspension (Δn < 10^{-3} when Φ > 10%) and relatively high scattering aspect.
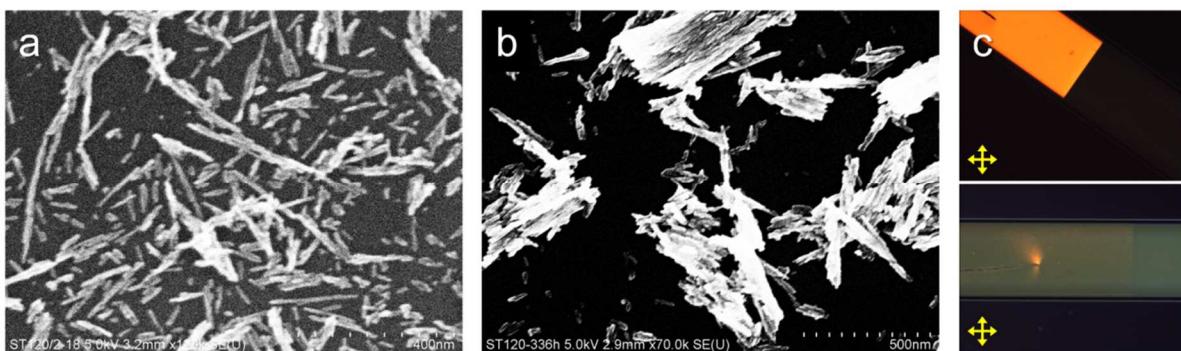
Figure 1.15. SEM images of aggregated rutile nanorods synthesized with the reaction time of 18 hours-(a) and 36 hours-(b). (c) Polarization optical micrographs of the (a) suspension in a glass capillary tube placed parallel and 45° to the polarizers.

As a next candidate material, Rutile appeared advantageous considering its high refractive index ($n_{rutile} \sim 2.70$) that may provide much larger form birefringence compared to Boehmite ($n_{boehmite} \sim 1.65$). Synthesis method using aqueous $TiCl_4$ solution reported by Dessombz et al.[5] was followed to make rutile nanorods. However, the rutile particles synthesized in varied experimental conditions – reaction time and temperature – were all aggregated and polydispersed as shown in **Figure 1.15**. Moreover, even worse than the case of Boehmite, the rutile nanorods aggregated shortly after the synthesis forming powders settling at the bottom of the container. This result led us to try surface functionalization again by phosphonate or dopamine[48] molecules. Unfortunately, in all cases a highly dispersed nanorod suspension satisfying the required optical quality could not be prepared through all these efforts. All the rutile nanorod suspensions prepared were very opaque but not notably birefringent ($\Delta n = 4.5 \cdot 10^{-3}$ when $\Phi > 9\%$). This is estimated to be due to the large scattering of aggregated rods with high refractive index and poor LC orientation owing to colloidal instability.

Mendipite (Pb₃O₂Cl₂)

Out of the MLC systems that have already been demonstrated, any other new anisotropic nanoparticle materials could be a candidate if they show the expected colloidal and optical properties. About the same time of the beginning of this project, Korgel *et al.* had published the solventless thermolysis synthesis of mendipite nanobelts that show an exceptionally high birefringence that exceeds 1 ($\Delta n = 1.1$) measured on a single nanowire in the air.[49] Thus it was considered promising to obtain outstanding collective optical effect if LC properties could be incorporated into the colloidal suspension of mendipite nanoparticles. **Figure 1.16** shows the SEM and TEM images of mendipite nanobelts and the observed large optical retardation from isolated single nanobelts.
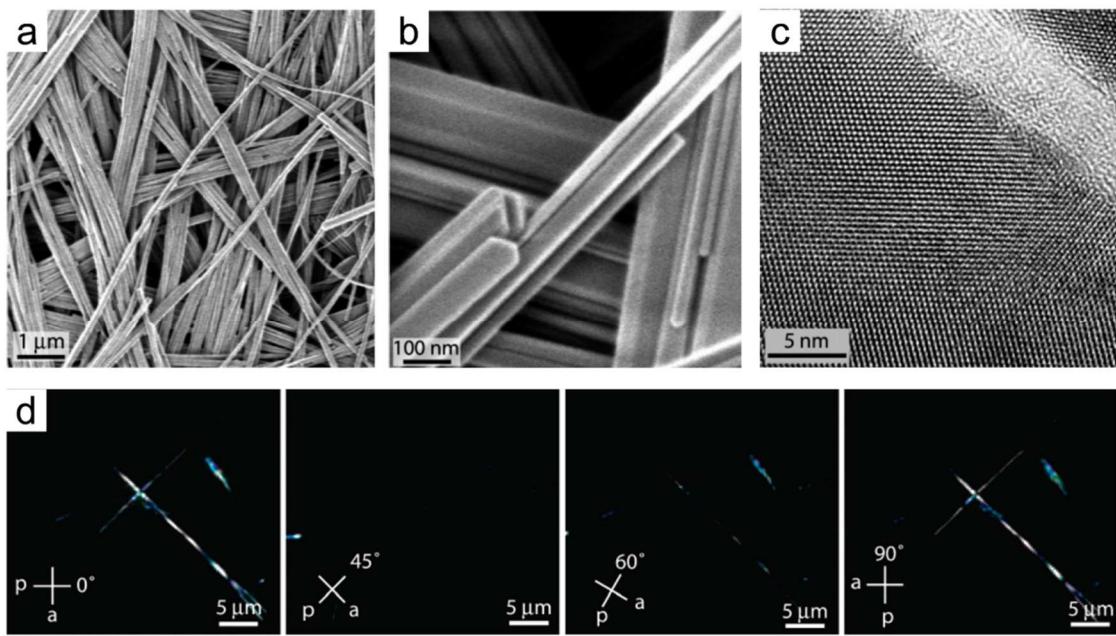
Figure 1.16. SEM-(a,b) and TEM-(c) images of crystalline mendipite ($Pb_3O_2Cl_2$) nanobelts synthesized by solventless thermolysis technique. (d) Polarization optical micrographs of single nanobelts in different polarizer and analyzer angle. *Figure taken from the reference paper* [49]

According to the original paper[49], highly crystalline mendipite nanobelts are synthesized by two steps: preparation of lead base precursor solution and its calcination. However, it was not easily reproduced the same quality as the XRD patterns on our powder products had often shown ambiguously elongated peaks though they are situated on the same position with the peaks in the reference patterns. Despite the repeated experiments to find the optimal condition by modifying the main parameters such as the duration and the temperature of thermal treatment and the precursor stoichiometry, the obtained mendipite powders had no good quality and the results were not reproducible.

Lanthanide phosphate (LnPO₄): Choice of LaPO₄

The finally considered nanoparticle materials are lanthanide phosphate ($LnPO_4$) series with diverse lanthanide elements on the Ln position. There had been already many reports on the synthesis of anisotropic nanoparticles of $LnPO_4$, but no MLC systems had been made yet according to the literature. Gadolinium phosphate and lanthanum phosphate were chosen as they had often been synthesized in form of long rod-like particles appropriate to exhibit LC organization and also as their interesting magnetic and luminescent properties.
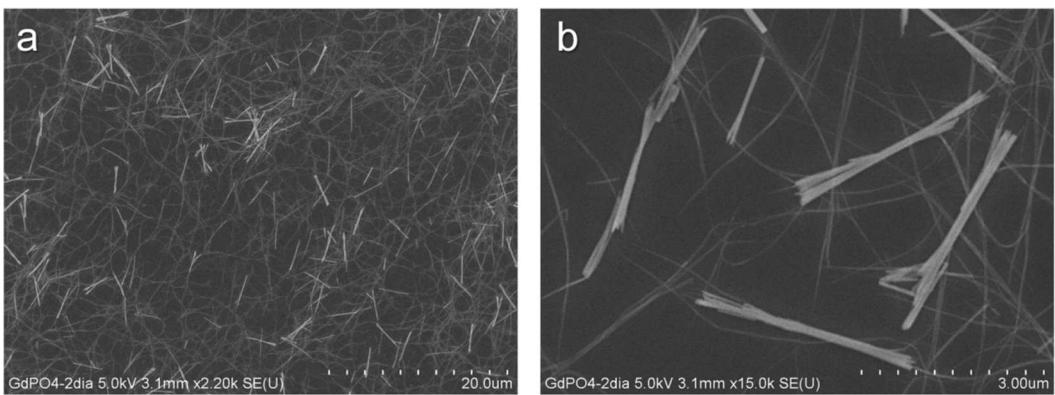
Figure 1.17. SEM images of hydrothermally synthesized GdPO$_4$ nanoparticle aggregates.

GdPO$_4$ nanorods were synthesized in the same way noted in the next chapter for LaPO$_4$. As shown in **Figure 1.17**, the mainly obtained GdPO$_4$ particles by our experimental procedure were bunches of several tens of single nanoparticles together and these aggregates had an average length of ~3.5μm and the width of ~150nm. The smaller particles did not seem to stay individually dispersed but rather to form nanowires by end-to-end attachment. Because of such a strong aggregating tendency of the nanorods, their colloidal suspensions were much more viscous and usually formed gels that disabled liquid crystalline ordering by density control or by applying electric field. Thus a relevant birefringence analysis could not be conducted with our GdPO$_4$ samples.

Even though it cannot be generalized, in our specific experimental procedure, LaPO$_4$ nanorods could be synthesized with relatively much higher ratio of individually dispersed particles than GdPO$_4$. Compared to all other compositions we tested, the particle dispersion quality of LaPO$_4$ was markedly high and it could be further improved by optimizing the synthesis process. Moreover, LaPO$_4$ nanorods had a very long rod-like geometry with the average aspect ratio higher than 20 that would be favorable to exhibit liquid crystalline arrangement. The optical property was also promising. The synthesized suspension was colorless, relatively transparent, and displayed flow birefrignence when observed between crossed polarizers as a good sign for a possible LC behavior. All these observations from LaPO$_4$ best-satisfied the above-discussed characteristics required for an applicable MLC material. Therefore, LaPO$_4$ was finally chosen for the base material of this project. The details of the advantageous colloidal and optical properties are demonstrated in the next chapter.

1.3. Conclusion

Mineral liquid crystals (MLC) are materials in which mineral's intrinsic properties are combined with the self-organization behavior of colloids. Onsager's entropic model provided early the theoretical basis on understanding MLCs. And there exist some synthetic and natural colloidal systems such as Goethite, Boehmite, and Rutile nanorods or Gibbsite clay platelet suspensions, all of which are in a good accordance with the theoretical

prediction. However, the use of such systems for a practical application has hardly been demonstrated due to the fundamental drawbacks of colloidal systems such as limited colloidal dispersion stability. With a clear objective of our project oriented towards applications to optical devices, a best candidate material was carefully searched focussing on obtaining high dispersion stability and appropriate optical properties. After the examination of many reported MLC materials and possible synthetic processes for anisotropic nanoparticles, $LaPO_4$ nanorods were finally chosen for our base material considering their non-aggregating aspect during the synthesis and the transparent birefringent optical properties of their colloidal suspensions. It was here the starting point of this thesis study. The detailed study on the synthesis and LC properties of $LaPO_4$ system is discussed from the next chapter. Working more on the synthesis of other mineral colloidal systems would also be interesting and it remains as our future work.

Chapter 2

Synthesis of Liquid Crystalline LaPO$_4$ Nanorod Suspensions

The basic theory of lyotropic liquid crystals (LC) and some representative examples of mineral colloidal LC systems were addressed in Chapter 1. It was also discussed why lanthanum phosphate (LaPO$_4$) was chosen as the base material of this thesis study among the other mineral compounds investigated in the earlier period of this project. In this chapter, it is concretely demonstrated how the LC suspension of LaPO$_4$ nanorods are prepared, from the synthesis to the observation of LC mesophases. As it was anticipated, a key issue for the successful synthesis of a fine mineral liquid crystal (MLC) system with colloidal LaPO$_4$ nanorods was to maintain the excellent dispersion stability in the highly concentrated regime up to the LC phase transition density. It is shown here the strategies to acquire permanently dispersed nanorods suspension totally free from aggregation, and then the as-obtained outstanding LC properties are investigated.

2.1. Hydrothermal synthesis of LaPO$_4$ nanorods

Wet-chemical routes to synthesize micro- or nano-crystals of LaPO$_4$ have been developed since a half century ago.[50] The interest of the early study was to develop a mild and economic way of manufacturing crystalline LaPO$_4$ which is an efficient host matrix of lanthanide phosphor elements (Eu, Ce, Tb…). During decades, LaPO$_4$ has been widely used for applications in luminescent lamps, displays, sensors and etc.[51-52] A typical wet-synthesis method for LaPO$_4$ is hydrothermal crystal growth that is achieved basically in two steps: (1) precipitation of primary particles by mixing aqueous La^{3+} and PO$_4^{3-}$ precursor solutions, (2)

hydrothermal growth of these particles at 150~200°C.[51, 53-55] Two essential advantages of this process are its surfactant-free regime and the rapid simple batch style that should be easily scaled up for industrial use.

2.1.1. Bibliography – anisotropic growth & aggregation

Recent studies focussed on controlling the morphology of $LaPO_4$ nanocrystals by controlling the crystallographic growth rate depending on the acidity of the medium during the synthesis in the aqueous conditions.[51, 53] **Figure 2.1** shows the dramatic morphology change of $LaPO_4$ nanocrystals by a simple adjustment of pH of the La^{3+} and PO_4^{3-} precursor solutions.
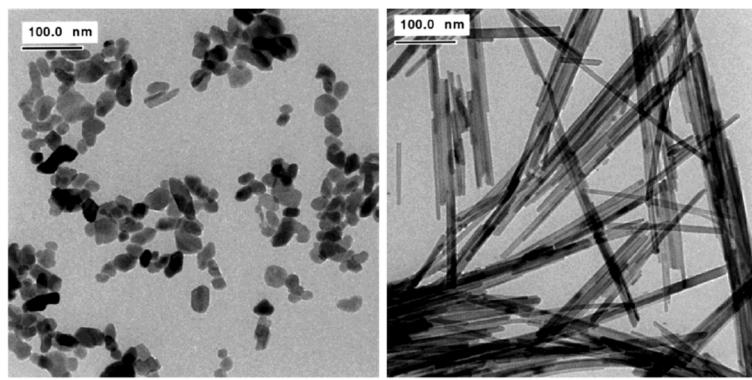
Figure 2.1. TEM images of $LaPO_4$ nanocrystals prepared at pH = 12.5 (left) and pH = 1.7 (right). *Figure taken from reference* [51]

Here, the very long and straight rod-like morphology of the particles shown in the right image originates from the crystallographic growth rate along the [001] direction much faster than the other directions in the low pH medium.[51, 53-55] The anisotropic growth nature is interpreted generally by the surface free energy for specific lattice planes and the surrounding medium. The XRD study on $LaPO_4$ nanorods had revealed their hexagonal structure (**Figure 2.2**) similar to ZnO or $Ln(OH)_3$ that are widely known for anisotropic growth.[53] In this structure, the anions and cations are alternately placed along the [001] direction giving rise to the largest net charges and strongest polarity to the (001) and (00$\underline{1}$) facets.[56] According to the spherical diffusion model proposed by Peng et al[57] and supported by Yu et al[58] for strongly anisotropic crystalline nanorod synthesis, it is estimated that small primary particles are generated at the beginning by the supersaturated precursor mixture, and then the facet-selective 1-dimensional growth is promoted during the Ostwald ripening process under control of the range of [La^{3+}] and [PO_4^{3-}] toward the growth stage as schematically illustrated in **Figure 2.3**. Here, the acidic condition results in the high concentration ratio of cations and anions, [La^{3+}]/[PO_4^{3-}]. The excess of La^{3+} ions would greatly increase the surface charge density enhancing the fast growth rate on the (001) and (00$\underline{1}$) facets.
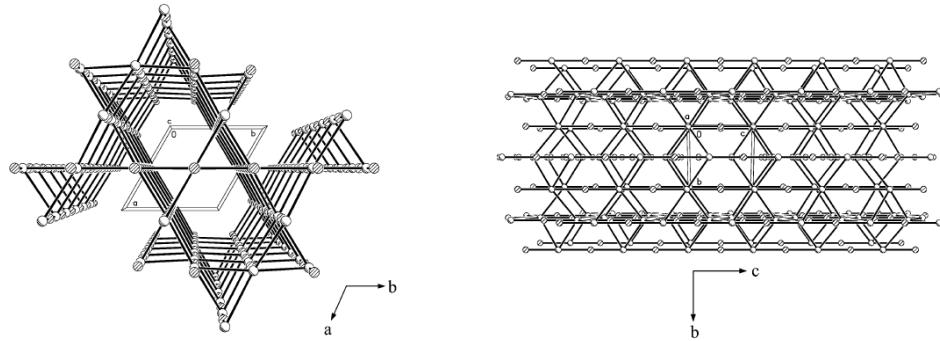
Figure 2.2. Packing view of hexagonal rhabdophane structure along the *c* axis (left) and *a* axis (right). *Figures taken from reference* [53]

Spherical diffusion model   Highly anisotropic growth
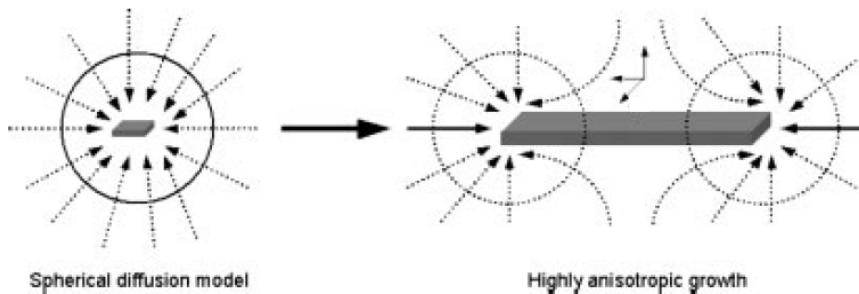
Figure 2.3. Illustration of spherical diffusion model for primary particles (left) and 1-dimensional growth under condition of high reaction activity at the ends during the Ostwald ripening process (right). *Figures taken from reference* [58]
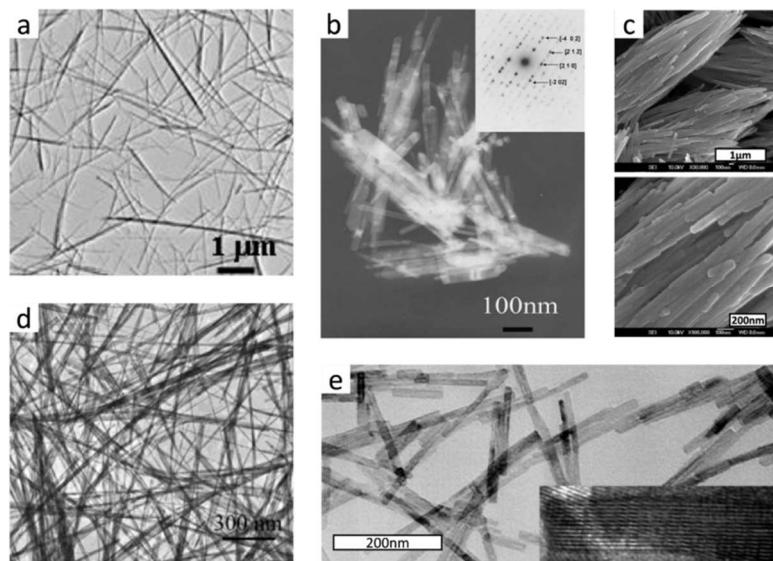
Figure 2.4. TEM and SEM images of hydrothermally synthesized $LaPO_4$ or $LnPO_4$ nanorods showing their strong aggregating nature. *Figures taken from reference papers* (a)-[59], (b)-[60], (c)-[55], (d)-[53], and (e)-[56].

Despite such a highly anisotropic morphology of the LaPO$_4$ nanorods, there has been so far no report on the LC behavior of their colloidal suspensions. This is presumably because of the aggregation that has usually occurred during or after the hydrothermal synthesis. Large rod aggregates are not appropriate for lyotropic LC behavior unless they are re-dispersed by any chance. Rod aggregates larger than a couple of micrometers in length are often unstable in colloidal suspensions settling at the bottom resulting in turbid milky aspect due to the large scattering of light. Indeed, no example of highly stabilized LaPO$_4$ nanorods without aggregation could be found from any published report. All the electronic microscopy images taken from the reference papers in **Figure 2.1** and **Figure 2.4** show the LaPO$_4$ (or LnPO$_4$) nanorods' strong tendency to aggregate.

2.1.2. Optimizing the synthesis process

In this study, aiming to make a LC system with LaPO$_4$ nanorods, the reaction process was revisited and a simple method was developed to produce individually dispersed nanorod suspension avoiding aggregation during the synthesis. And a method to maintain, and even enhance, the dispersion stability for long time after the synthesis at high particle concentration was discovered.

Effect of reaction temperature and concentration

As a starting point, we found out following the early developed methods[51, 53] that, when the precursor solutions were mixed, instantly generated primary particles rapidly aggregated through some kind of oriented attachment mechanism leading to uncontrolled bundles and aggregates (**Figure 2.5.a-inset**), and the following hydrothermal treatment thus leads to large rod aggregates (**Figure 2.5.a**).
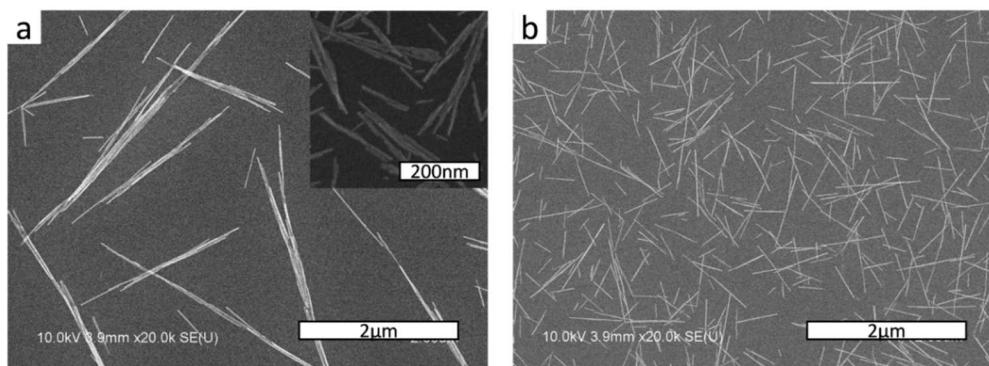
Figure 2.5. (a) Aggregated LaPO$_4$ nanorods and their aggregated primary particles before hydrothermal growth (inset) obtained by following the reported method. (b) Non-aggregated nanorods obtained with the revisited process.

Considering the fundamental concept of aggregation kinetics of charged colloids that high particle concentration and high temperature accelerates aggregation by increasing the probability of thermal activation[23], a key improvement could be obtained by minimizing the concentration (down to 0.05 M) and the temperature (down to 0°C) of the precursor solutions for the first step. Importantly, the second step of hydrothermal treatment should be performed swiftly in order to promote the particle growth through the ripening process instead of aggregation without recrystallization. Following such a procedure, the dispersion quality was greatly improved as **Figure 2.5.b** shows the as-prepared nanorods that are individually dispersed.

Effect of pH

The anisotropic growth mechanism described in the literature is also supported by our own experimental observation. **Figure 2.6.a-b** shows the SEM images of the primary particles-(a) and their grown nanorods-(b) from the mixture pH = 1.2 (both images are in the same magnification scale). The primary particles have a highly polydisperse morphology. But the particles grown at the low pH have straight and very long rod-like morphology. The average length (L) and diameter (D) for **Figure 2.6.b** are 252nm and 11nm respectively with the aspect ratio (L/D) of 23. This result could be explained by the reaction mechanism introduced in the section 2.1.1 as the high pH would apparently involve a high $[La^{3+}]/[PO_4^{3-}]$ ratio generating high surface charge density on the particle surface. The fact that the synthesized nanorods globally have much higher polydispersity in length than in diameter (See the rod size distribution data shown in **Figure 2.9** and **Table 2.1**) also indicates that the growth on the facets other than [001] was much slower during the Ostwalt ripening process. On the other hand, the size and the length to diameter aspect ratio (L/D) of particles grown at higher pH of 4.6 are both much smaller after the same hydrothermal treatment (**Figure 2.6.c**). In this case, a significant decrease of $[La^{3+}]/[PO_4^{3-}]$ ratio would have involved a decrease of the surface charge density, which was also noticed by the loss of colloidal dispersion stability.
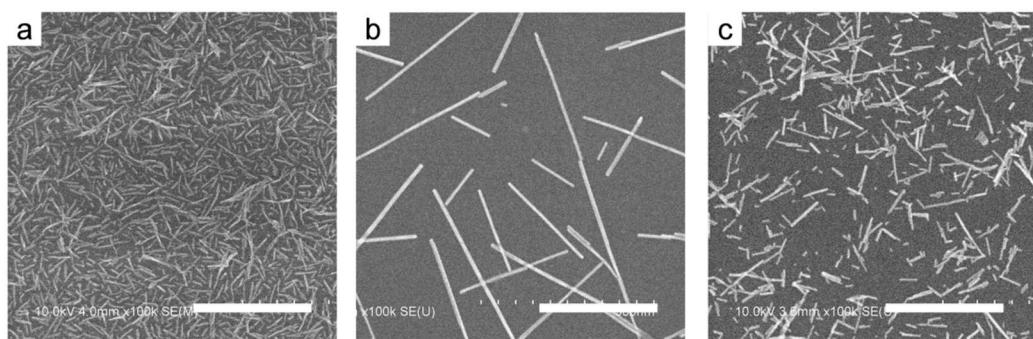
Figure 2.6. SEM images – all in the same magnification scale – of primary LaPO$_4$ particles-(a) and hydrothermally grown nanorods obtained in [La^{3+}] rich condition (equimolar mixture at pH = 1.2) (b) and in [PO$_4^{3-}$] rich condition (1 : 2 mixture of La^{3+} and PO$_4^{3-}$ precursors at pH = 4.6) (c). The white scale bars indicate 300nm.

Mono-crystalline aspect
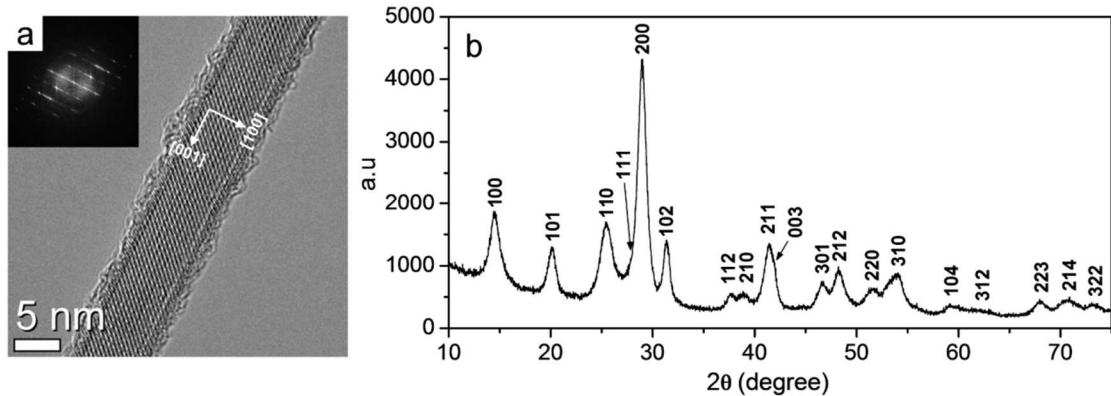
Figure 2.7. (a) HR-TEM image of a synthesized single LaPO$_4$ nanorod. The white arrows indicate the crystallographic axis. Inset is the corresponding Fast Fourier Transformation (FFT). Note that the irregular surface is due to the fusion of the crystal by the high voltage electron beam for high resolution. (b) XRD pattern of the standard rods and corresponding indexation from the rhabdophane reference -JCPDS 46-1439.

Our optimized synthesis process also provides a good mono-crystalline structure of each individually dispersed nanorods. It could be anticipated from the straight form with a constant diameter in the SEM image (**Figure 2.6.b**), and is confirmed by high-resolution transmission electron microscopy (TEM) image in **Figure 2.7.a**. This figure clearly shows a periodic fringe pattern of lattice planes. The rod shape corresponding to the preferential growth along the *c* axis of the hexagonal 'rhabdophane' phase was evidenced by powder X-ray diffraction (XRD) shown in **Figure 2.7.b**.[53]

2.1.3. Controlling the rod size by ultra-sonication & low temperature synthesis

Rod size is an important parameter for the LC behavior as the Onsager's model predicts the direct dependence of phase transition density on the rod aspect ratio (See Chapter 1). It would therefore be a meaningful experimental study to make LC suspensions of LaPO$_4$ nanorods with different average rod size. It was described above that the rod morphology of LaPO$_4$ nanorods could be controlled by playing on the acidity of the medium during the synthesis. Nevertheless, for the purpose of making LC suspension, this parameter could not be modified. It is because the high colloidal stability essential for LC behavior is guaranteed only in a narrow pH range around 2 where the nanorod surface is strongly charged while the ionic strength is not too much elevated to screen this charged surface.

In this regard, some other strategies were considered and it was found possible to cut the nanorods by using ultra-sonication after finishing the growth reaction. By simply applying an ultra-sonic wave in the synthesized aqueous colloidal LaPO$_4$ nanorod suspension for several hours, samples with the same diameter (*D* = 11nm) but shorter average length (*L* = 200nm) corresponding to an aspect ratio of *L/D* = 18 could be obtained. The original

nanorods without any treatment will further be referred to as standard-rods, and the shortened nanorods obtained after ultra-sonication as lar-rods considering their lower aspect ratio as compared to the standard rods. Another route to obtain nanorods with smaller average size was to let the primary particle suspension grow at ambient temperature instead of performing the hydrothermal treatment. In this case, we observed that recrystallization and growth of the primary particles does occur but slowly in several days allowing to obtain smaller particles. The overall dispersion quality of these samples is not as good as the one obtained after rapid hydrothermal treatment due to the aggregation of primary particles as mentioned previously. However this was the only way to obtain particles with a significantly differentiated overall size maintaining the same aspect ratio of the standard-rods. The average length and diameter of these nanorods were about three times lower (L = 80nm, D = 3.7nm, L/D = 22), and so they will further be referred to as s-rods, considering their Smaller overall size compared to the standard-rods.
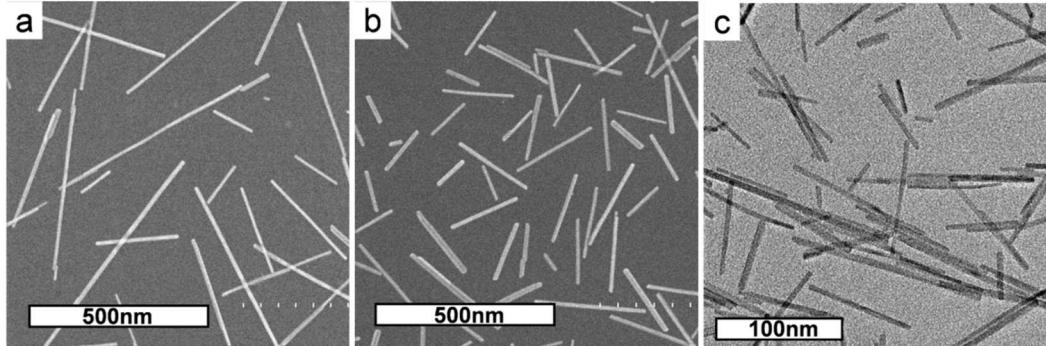
Figure 2.8. (a) SEM image of standard-rods. (b) SEM image of lar-rods. (c) TEM image of s-rods.

SEM and TEM images of these nanorods in different size are shown in **Figure 2.8**. And the histogram of the distribution of L and D of each sample are shown in **Figure 2.9**. In this figure, the red lines are lognormal fittings providing the standard deviation (σ) values quantifying the polydispersity. This size information is listed in **Table 2.1**. Here it can be identified that the σ values are all ~0.6 for the average length, and ~0.2 for the average diameter which supported the 1-D growth mechanism by Ostwald ripening process suggested in the literature (See the section 2.1.1 and 2.1.2).
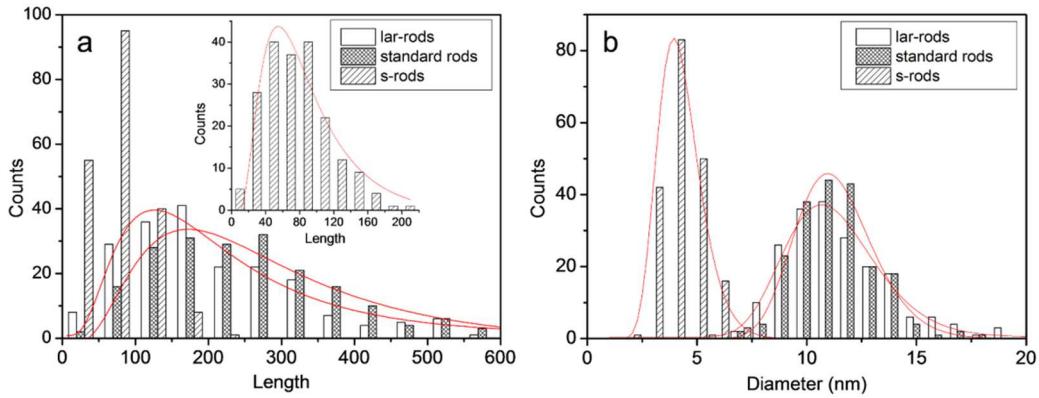
Figure 2.9. Length-(a) and diameter-(b) distribution histograms for size-differentiated LaPO₄ nanorod samples. The red lines are Lognormal fittings. The inset in (a) is for s-rods with smaller bin size.

	L (nm) / σ	D (nm) / σ	L/D
standard-rods	252 / 0.63	11 / 0.19	23
lar-rods	200 / 0.64	11 / 0.23	18
s-rods	80 / 0.58	3.7 / 0.16	22

Table 2.1. Length (*L*), diameter (*D*), aspect ratio (*L/D*), and their standard deviation (*σ*) of the size-differentiated LaPO₄ nanorod samples.

2.1.4. Colloidal dispersion stability

In the aqueous colloidal suspension, the dispersion stability of the synthesized LaPO₄ nanorods could be maintained roughly at 1 < pH < 3 when the particle concentration in volume fraction (Φ) were less than 1%. Flow-birefringence was observed in this range indicating the stabilized nanorods' capability to spontaneously organize toward a LC phase. However, the dispersion equilibrium was easily broken out of this limited range of pH and Φ, and the typical instable kinetics such as flocculation or gelation took place as observed generally on various anisotropic inorganic colloidal systems.[24-25, 27, 47, 61] Such a dispersion instability owing to the particle aggregation disabled the system to exhibit spontaneous Iso-Nem phase transition that might have occurred at a higher Φ. Moreover, aging of the aqueous system was indispensable even at the pH and Φ range optimized for the initial colloidal stability: passing through a couple of months, aggregates were slowly generated making the suspension becomes turbid.
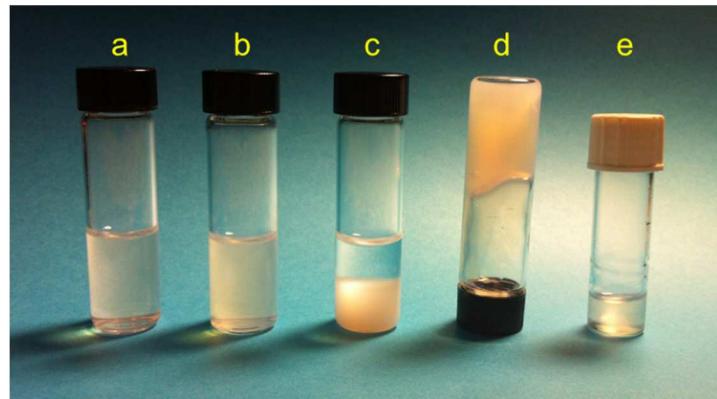
Figure 2.10. Aqueous colloidal suspensions of well-dispersed rods-(a), after aging one month-(b), aggregated rods-(c), gelated rods-(d), and well-dispersed rods concentrated in EG-(e). Rod volume fraction (Φ) is 0.5% for (a-c), 1% for (d), and 6.2% for (e).

Figure 2.10 shows bulk aqueous colloidal suspensions in such different cases. The well-dispersed rod sample (**Figure 2.10.a**) corresponds to **Figure 2.5.b** and shows a very limpid aspect. When the same sample was aged for one month, it becomes less limpid because of aggregation slowly occurring in the suspension (**Figure 2.10.b**). Sample in **Figure 2.10.c** corresponds to **Figure 2.5.a**, where the aggregated rods generated during synthesis are not stable and settle at the bottom of the vial showing a turbid milky aspect due to the large scattering of light related to the large size of aggregates. **Figure 2.10.d** is a sample at $\Phi = 1\%$ with the pH adjusted to 3.5 by dialysis. This sample was as stable as the well-dispersed sample before dialysis, but it turned into a turbid gel state due to the aggregation at such a higher pH. To avoid such an aggregation easily occurred in the aqueous medium that is unfavorable for the LC organization, mineral liquid crystals (MLC) have sometimes been prepared by grafting polymeric molecules at the surface of rod-like particles to apply steric hindrance at the attraction domain.[7-8, 62] But it is true that this way requires complex chemical routes and may change the original property of the colloidal system due to the large amount of organic molecules added into the system. Compatibility of the molecules with both the particle surface and the solvent should also be considered deliberately.

2.1.5. Concentration and transfer into ethylene glycol

In a much more simple way, it was possible to perfectly exclude aggregation and disclose pure LC properties of LaPO$_4$ nanorods by exchanging the solvent from water to ethylene glycol (EG). EG is polar protic solvent leading to the electrostatic stabilization of charged particles as in water. This is shown experimentally as the stability of the LaPO$_4$ particles is largely increased when EG is acidified to ensure the optimal surface charge, while the increase of the ionic strength by addition of salts decreases the dispersion stability. Furthermore, it was observed that the stability in EG is significantly improved as compared to water, suggesting an additional effect of EG for the stabilization of the particles. The explanation has to be found in a specific interaction between glycol groups and the surface of

the particles resulting in solvation and/or chelation of surface ions.[63] The presence of a capping shell of structured EG molecules may limit the minimal distance between particles providing the additional stabilization through steric hindrance. **Figure 2.11** schematically shows the EG molecules surrounding the LaPO$_4$ nanorod surface. The strong affinity of glycol groups with the charged rod surface and also the exceptional hydrogen bondings among EG molecules seem to play a key role for the observed outstanding colloidal stability. This appears similar to the common cases where polyethyleneglycol (PEG) is used to stabilize particles in water or biological media.[64]
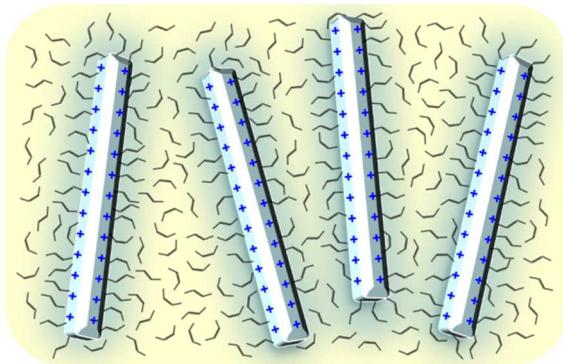
Figure 2.11. Schematic snapshot of the LaPO$_4$ nanorods of which the surface is functionalized by ethylene glycol molecules.

It should also be noted that the transfer is very easy, since EG is just added in the initial suspension and water is then removed by distillation. This method also enabled to modify the rod concentration (Φ) at the same time. The final value of Φ could be determined simply by the ratio between the volume the original aqueous suspension and the volume of EG added. For example, when 5mL of EG was added to a 50mL aqueous suspension with Φ = 0.5%, the final Φ of EG suspension after distillation becomes 5%. Therefore, by a single distillation process that takes a short time (less than 1 hour), well-dispersed nanorods could be transferred from a diluted aqueous suspension into EG obtaining finally a high concentration. This is a novel way to induce nanorods to organize LC structure by satisfying the two essential conditions for it: (1) high volume fraction of rods (Φ), and (2) high colloidal stability free from aggregating kinetics.

Actually, a permanent colloidal stability was achieved in EG over a large ionic concentration range at the elevated Φ where gelation dominated in the aqueous medium. As an evidence, a standard-rod suspension sample transferred in EG and concentrated up to Φ = 6.2% (20.4wt%) is shown in **Figure 2.10.e**. This sample is displaying a constant large transparency without any sign for aggregation during more than two years since it was prepared. Such a transparency is both due from the stability of the individually dispersed rods and also the high refractive index of EG (n_{EG} = 1.43) closer to that of crystalline LaPO$_4$ (n_{LaPO4} ~ 1.7) as compared to water (n_{water} = 1.33) in which the light scattering decreases.

In summary, the general hydrothermal process for LaPO$_4$ nanorods had to be modified because it did not guarantee the particle dispersion after the synthesis. A significant improvement was made by mixing diluted equimolar (0.05M) La^{3+} and PO$_4^{3-}$ precursor solutions at low temperature (0°C) and heating it up rapidly. This was efficient to minimize the rod aggregation until finishing the rod growth reaction. The as-synthesized nanorods were then concentrated and transferred into ethylene glycol (EG) medium by a simple distillation step. While aqueous medium is limited to preserve nanorod dispersion in long timescale, EG allows permanent colloidal dispersion stability even for higher rod volume fraction ($\Phi > 6\%$) which is promising for displaying LC behavior.

2.2. Liquid crystalline behavior

As demonstrated in the previous section, the first period of this study was dedicated to optimize the hydrothermal synthesis process to produce crystalline LaPO$_4$ nanorods avoiding their aggregation, and then to make a highly concentrated and permanently stabilized suspension in the ethylene glycol medium (EG). The purpose of such an effort was to make this suspension to exhibit liquid crystalline (LC) property. In this section, as a result of the successful optimization of the synthesis and transfer, the outstanding LC properties of LaPO$_4$ nanorods in EG are demonstrated.

2.2.1. Bulk suspension

Macroscopic phase separation

Thanks to the outstanding colloidal stability, two distinct liquid crystalline organizations at equilibrium have been observed from the concentrated nanorod suspension in EG. **Figure 2.12.a-b** shows a macroscopically phase separated LC suspension of lar-rods concentrated in EG (Φ=3.4%, before phase separation). The picture of the sample between crossed polarizer (**Figure 2.12.b**) clearly shows the isotropic (Iso) upper phase and the nematic (Nem) bottom phase where some birefringence due to the randomly distributed nematic domains can be seen. This Iso-Nem macroscopic phase separation occurred only in one night after preparing the sample. This is exceptionally fast compared to many other MLC systems reported to take weeks or months for separation. Such a fast phase separation indicates that the LC behavior is not perturbed by other kinetic effects like gelation. Thus it is again evidences that the system is very well stabilized. Moreover, this sample at the elevated Φ is transparent not only in the isotropic phase but also in the nematic phase so that the figure behind the 2mm-think cell is clearly seen indicating that aggregation was efficiently eliminated.
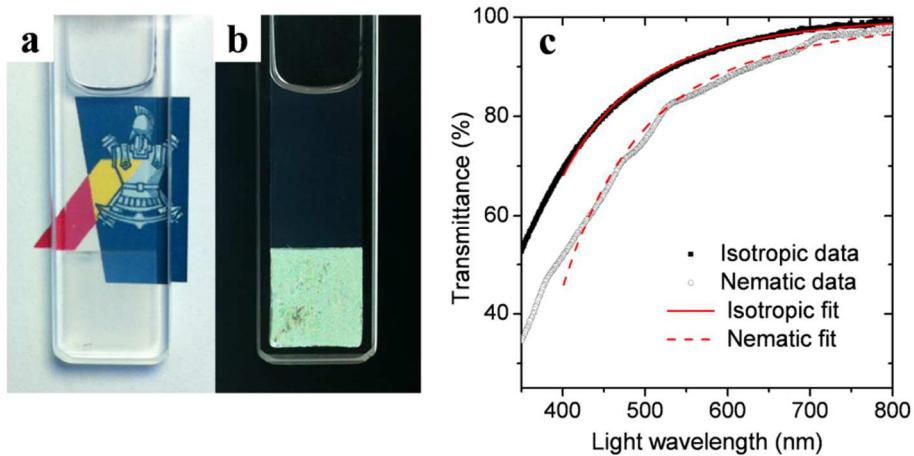
Figure 2.12. (a) Macroscopic isotropic liquid – nematic (Iso-Nem) phase separation of LaPO$_4$ nanorod colloidal suspension in ethylene glycol. The cell thickness is 2mm. (b) The same sample observed between crossed polarizers. (c) Transmittance spectra as a function of the light wavelength (λ) of both phases from the same sample shown in (a) and (b). The red lines are fitted results according to the equation T = 1 – (λ_0/λ^4), characteristic of Rayleigh scattering.

Figure 2.12.c is the percent transmittance spectra of both phases which were taken directly from the same cell as in **Figure 2.12.a-b**. Here, the transmittances at 550nm were 91% and 84% respectively for isotropic and nematic phases. This indicates that, if it is used in the typical electro-optical devices with the thickness of several tens of micrometers, the light loss would be less than 1%. The transmission of the sample can be reasonably fitted with a $1/\lambda^4$ dependence with λ being the wavelength of the light. Such a behavior is typical of Rayleigh scattering. Note that some additional scattering exists in the nematic phase, probably due to the finite size of nematic domains.

Rod size fractionation

Size fractionation is a spontaneous phenomenon that occurs during the Iso-Nem phase separation of polydispersed systems. This is a tendency that relatively long rods are forming nematic phase that settles down, and the rest – relatively shorter rods – stay in the isotropic phase. This effect has been theoretically predicted[2, 65] and experimentally observed[12, 36, 66] in many mineral liquid crystals, and was observed also in the phase separated LaPO$_4$ nanorod LC suspension.
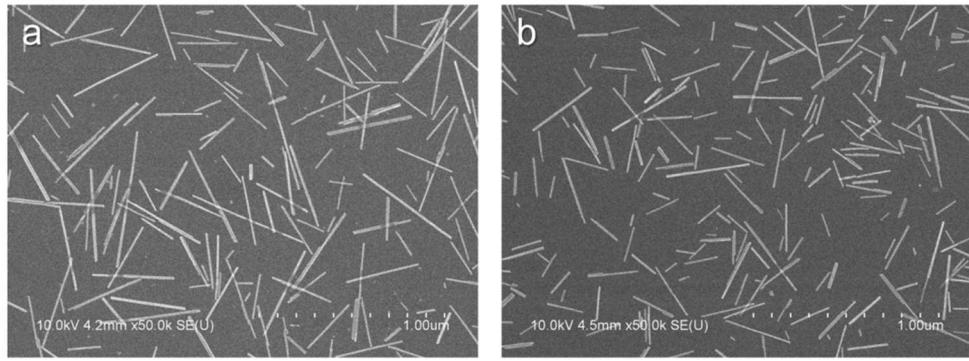
Figure 2.13. SEM images of LaPO$_4$ nanorods taken after macroscopic phase separation, (a) from the nematic phase and (b) from the isotropic phase.
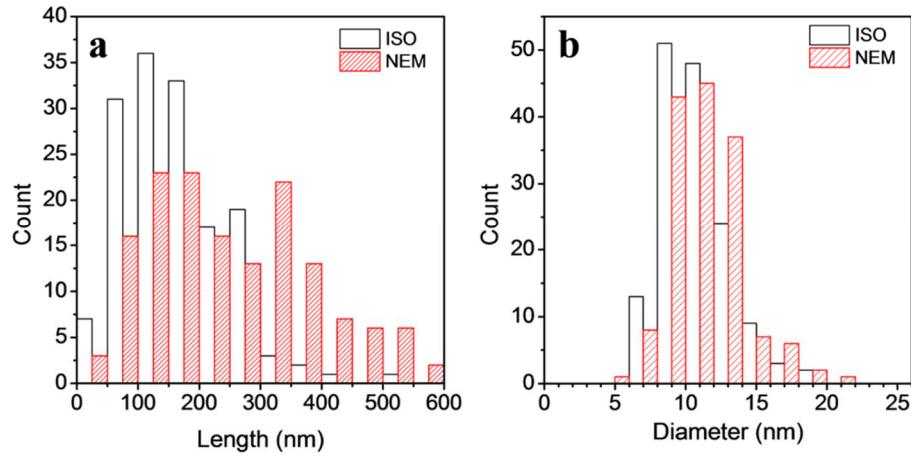
Figure 2.14. Histograms of nanorod length-(a) and diameter-(b) distributions measured in the isotropic and nematic phases respectively after macroscopic phase separation.

From the SEM images of nanorods from nematic and isotropic samples in **Figure 2.13**, it can be said that a visible difference of rod size exists between two phases, though each sample is still polydispersed. The size distribution histograms in **Figure 2.14** show more clearly this difference that the isotropic phase contains relatively short rods and the nematic phase contains more number of long rods. The average length and the aspect ratio for each sample was $L = 256$nm, $L/D = 22$ for nematic phase, and $L = 163$nm, $L/D = 16$ for isotropic phase. The histogram in **Figure 2.14.a** shows that fractionation phenomenon is quite effective to remove long rods ($L > 300$nm) from the isotropic phase. And it is more efficient to obtain a suspension of rods with low average aspect ratio than the ultra-sonication method used in the previous section. However, it is also shown that fractionation is not effective to remove relatively short rods from the nematic suspension, as a still large number of short rods ($L < 200$nm) stay in the nematic sample. For the future study, it would be a good strategy to utilize fractionation for size separation when a high Φ isotropic sample is necessary.

2.2.2. Microscopic phase behavior

For a detailed study on the LC phase behavior of LaPO$_4$ nanorod suspensions, polarization microscopy allowed to directly observe and identify most of the different LC mesophases that display distinct birefringence textures. Observing microscopic structure without waiting for the macroscopic phase separation is convenient because microscopic phase separation takes very short time, generally several minutes for the LaPO$_4$ samples.

Isotropic ↔ Nematic ↔ Columnar phase transitions

Experiment was conducted by diluting concentrated samples in pure LC phases prepared after the step for nanorod transfer from water to EG. The samples were observed at each dilution at a specific Φ calculated. Highly birefringent texture of columnar mesophase, the Schilieren texture of the nematic phase, tactoids at the biphasic Iso-Nem range, and the dark isotropic liquid phase without birefringence are observed along the dilution and shown in **Figure 2.15**. Here, typical Schilieren texture and tactoids confirm again that these samples correspond to dispersion equilibrium states.
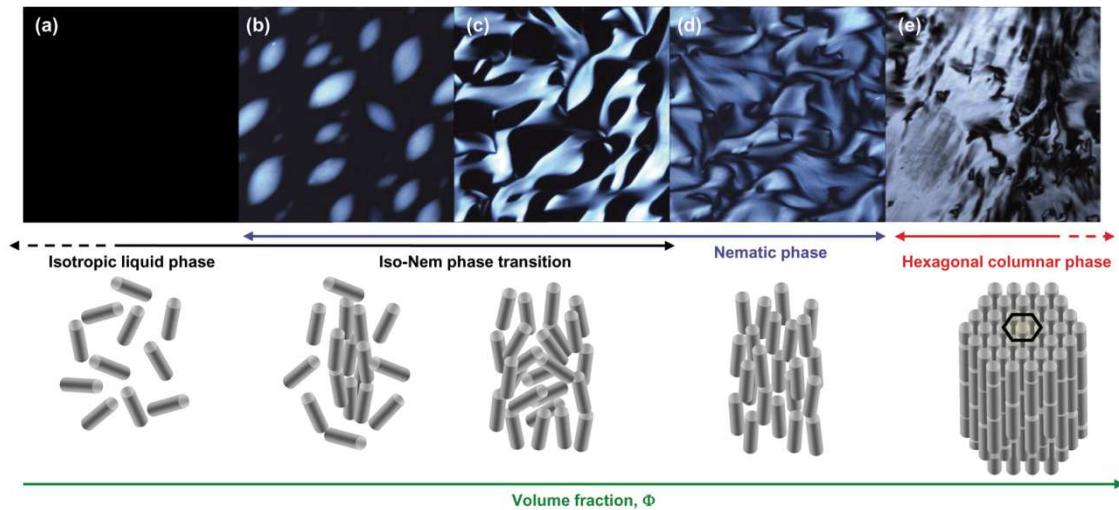
Figure 2.15. Optical textures observed by polarization microscopy and schematic representation of the different liquid crystalline phases of LaPO$_4$ suspensions when increasing the nanorod volume fraction. (a) Dark isotropic phase at Φ = 0.43%. (b) Tactoids in a biphasic phase at Φ = 0.92% (image size: 220μm). (c) Biphasic phase showing anti-tactoids at Φ = 1.1% (image size: 440μm). (d) Typical Schlieren texture of a purely nematic phase at Φ = 1.5% (image size: 440μm). (e) Highly birefringent texture of a hexagonal columnar phase at Φ = 4.34% (image size: 1760μm). Sample thickness is several micrometers for all microscopy images.

The dark image without any birefringent domain in **Figure 2.15.a**, obtained at Φ = 0.43%, indicates this sample is in isotropic phase where nanorods are all randomly oriented without any ordering property due to the low volume fraction. In **Figure 2.15.b**, nanorods start to form small birefringent nematic domains floating in the dark isotropic phase at higher volume fraction (Φ = 0.92%). These droplets having a shape of broad tree leaves are called tactoids as firstly named by Zocher.[1] And this phase in presence of both the isotropic liquid phase and the birefringent nematic droplets are called biphasic. Another biphasic phase at a little higher Φ being 1.1% is shown in **Figure 2.15.c**. In this phase, the birefringent texture is turned over due to the higher portion of nematic phase compared to the reduced volume of isotropic phase now floating in the birefringent nematic phase. These dark isotropic droplets are called anti-tactoids. At Φ = 1.5% the suspension is totally nematic without a presence of dark isotropic region. In this state, all nanorods are aligned together but the orientation of the mesoscopic domain is fluctuating resulting in such a particular texture that is often called as Schlieren texture. When the sample is much more concentrated than here (Φ = 4.34%) nanorods can also have positional order making transition into hexagonal columnar phase (**Figure 2.15.e**). As both nematic and columnar phases are totally birefringent, they could hardly be distinguished by polarization optical microscopy. Instead, the identification of columnar phase was done by small angle X-ray scattering (SAXS) experiment as discussed in the section 2.2.3.

Interestingly, these liquid crystalline textures could be observed also by TEM, which permitted to visualize the nematic alignment of individual nanorods captured on a TEM grill (**Figure 2.16**). For this, a TEM grill coated with negatively charged polystyrene sulfonate layer was soaked in the nanorod suspension and then rinsed before drying it. Even though this figure does not display directly the spatial spacing between particles in the liquid phase, it is revealed in **Figure 2.16.a** that non-aggregated individual nanorods are aligning with a very high order of orientation without touching each other. Moreover, in **Figure 2.16.b-d**, it is clearly shown how nanorods are aligned to form the typical LC textures such as anti-tactoid and lamellar fluctuation.

Phase diagram

As discussed in Chapter 1, in real systems of charged colloids, the LC behavior is not only determined by the variation of Φ but also by the ionic strength of the medium. In our $LaPO_4$ nanorod suspension, nitric acid concentration (C_{HNO3}) is the only substance changing the ionic strength. Thus C_{HNO3} can be noted as ionic concentration of the system. To change C_{HNO3} of the suspension, purification method by dialysis was again used as for the purification in aqueous medium just after the nanorod synthesis. In EG medium, which is highly viscous, dialysis should have been conducted several times in series to remove ions and adjust C_{HNO3} values.
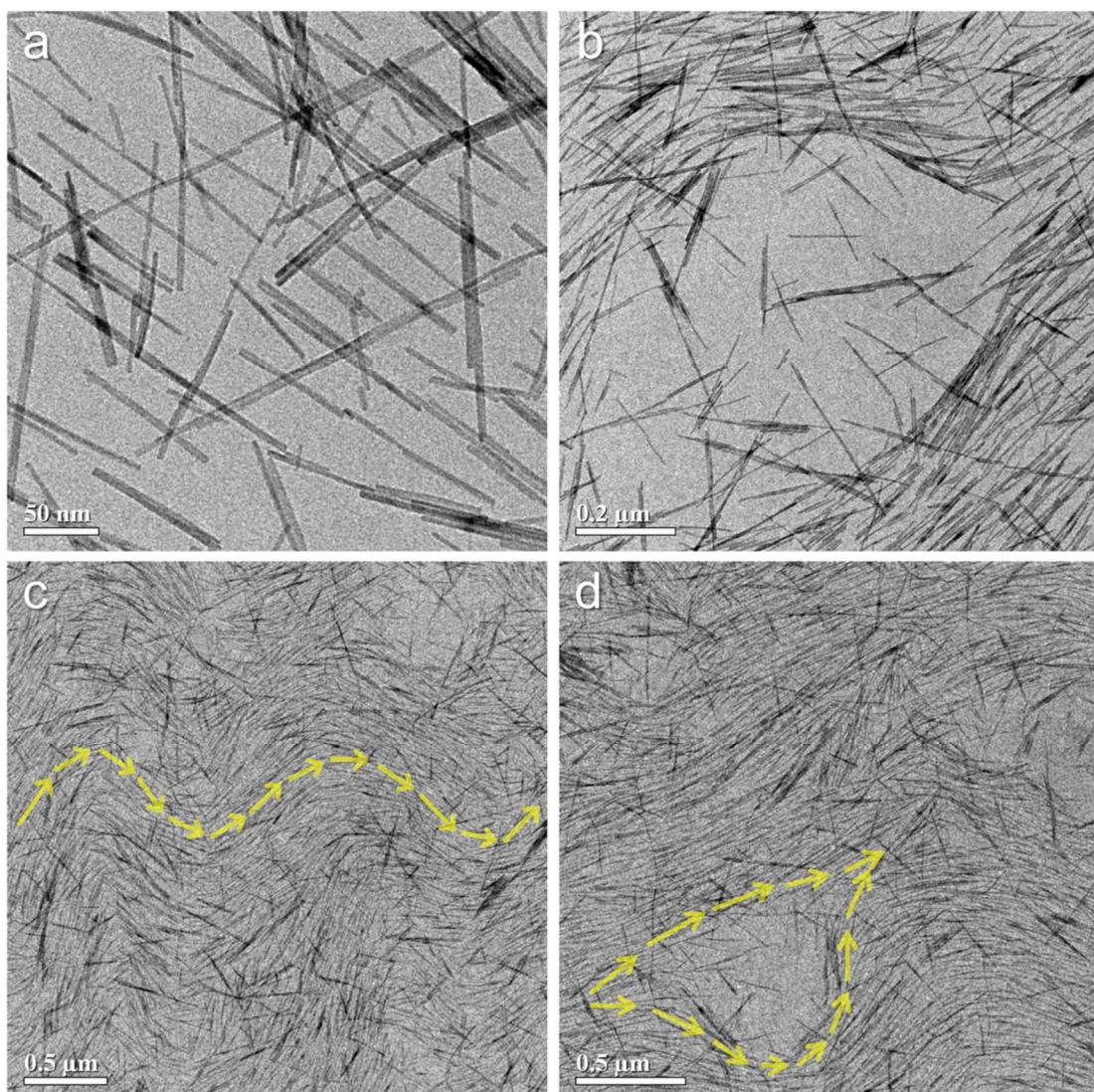
Figure 2.16. TEM images showing the liquid crystalline alignment of LaPO$_4$ nanorods. (a) Nematic orientation of individually dispersed nanorods. (b) Micro-phase separation inducing anti-tactoid structure. (c) Lamellar structure. (d) Anti-tactoid structure.

Repeating the observation of phase behaviors on the diluted samples starting from the highly concentrated and dialyzed LaPO$_4$ nanorod suspension, a phase diagram of the standard-sized nanorod samples as a function of the ionic strength and Φ could be established (**Figure 2.17**). The initial value of C$_{HNO3}$ of the samples in EG with large Φ (up to 9%) was ~0.1M. At such a high C$_{HNO3}$, the samples were generally in a turbid gel state due to the strong ionic strength that counterbalances the repulsive surface charge resulting in particle aggregation (Yellow region in **Figure 2.17**). Purification by dialysis effectively removed the nitric acid from those samples in the gel state. C$_{HNO3}$ of once dialyzed samples decreased to ~0.02M and the suspensions turned into a limpid LC mesophase sols. After a full purification, 99% of the nitric acid could be eliminated (C$_{HNO3}$ ~ 0.001M). The non-diluted samples escaped from the gel state were purely nematic or even columnar as shown

by X-ray scattering (See section 2.2.3). And their successive dilutions showing various textures of LC mesophases (**Figure 2.15**) allowed us to find out the concentrations where the phase transition occurs.
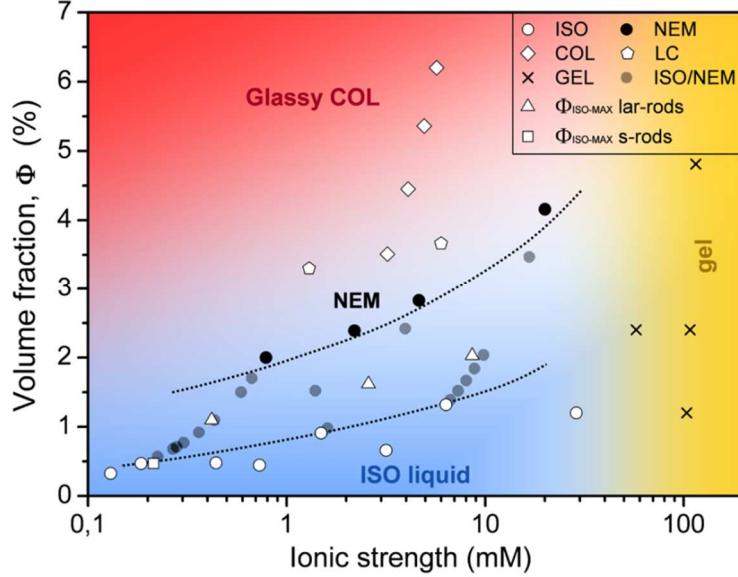
Figure 2.17. Phase diagram of LaPO$_4$ nanorod colloidal suspension in ethylene glycol. Open circles, black circles, and grey circles indicate isotropic, nematic, and isotropic/nematic biphasic domains of standard rods (L/D = 23) respectively. Open diamonds indicate columnar phase which were verified by SAXS, and open pentagons indicate purely liquid crystalline (nematic or columnar) domain of standard rods. Triangles indicate maximum volume fractions for purely isotropic phase ($\Phi_{iso-max}$) of lar-rods (L/D = 18) that are placed higher than those of standard rods. Open square is $\Phi_{iso-max}$ of s-rods (L/D = 22). Crosses indicate the high ionic strength domain where the suspension is in a gel state.

According to the phase diagram in **Figure 2.17**, volume fractions for the Iso-Nem phase transition are much lower on the whole studied ionic strength range than the theoretical value ($\Phi_{iso-nem}$ ~ 17%) calculated by substituting the average rod aspect ratio (L/D=23) into Onsager's theory of hard rods. Here, electrostatic interactions have to be considered, by defining an effective rod diameter (D_{eff}) which is larger than the bare one and which depends on both the ionic strength of the medium and the particle surface charge density. As discussed above, LaPO$_4$ nanorods are strongly positively charged in the acidic condition due to the surface protonation, which is in fact the driving force for the colloidal stability of the suspensions. Increasing ionic strength screens the repulsive electrostatic interactions, therefore revealing the bare particle dimensions by decreasing D_{eff}. Scaling Φ_{eff} also with the inverse of D_{eff}, it is expected a shift to higher volume fractions of the Iso-Nem phase transition, as it is observed experimentally in the phase diagram (dashed lines in **Figure 2.17**). Moreover, the highest volume fraction for purely isotropic liquid $\Phi_{iso-max}$ of lar-rods (open triangles) with the low aspect ratio (L/D = 18) are placed higher than those of standard rods.

These last two results show a qualitative agreement with Onsager's theory. The quantitative discrepancy with theory also observed in other MLCs[28] can be explained considering that the validity of Onsager's theory is for the needle-like limit, i.e. for very high aspectratio (*L/D* >> 1).[2] This is not the case of our LaPO$_4$ nanorods, especially when electrostatic interactions are taken into account by D_{eff}. Furthermore, rod polydispersity as well as attractive interactions can shift the volume fractions by broadening the biphasic domain at the Iso-Nem phase transition.[65] Such attractive interactions could originate from Van der Waals interactions, which become effective at high ionic strength when electrostatic repulsions are screened. They can induce a transition from a sol to a gel state, as indicated in yellow region in **Figure 2.17**.

2.2.3. Small Angle X-ray Scattering (SAXS)

This work was conducted by Dr. Eric Grelet at Centre de Recherche Paul Pascal in Bordeaux (CRPP) using the SWING Beam line of synchrotron SOLEIL.

An interesting feature of the concentrated suspensions is that their viscosity increased a lot during the purification process going toward the low ionic strength. They finally turned into a glassy-like state (Red region in **Figure 2.17**) which corresponds to a hexagonal columnar mesophase as demonstrated by small angle X-ray scattering (SAXS) in **Figure 2.18**. In this highly ordered phase, the nanorods self-organize into liquid-like columns which in turn form a bi-dimensional hexagonal crystalline array (**Figure 2.15.e**). In this phase at low ionic strength, repulsive interactions dominate, therefore avoiding particle aggregation and maintaining a large transparency of the suspension. For this reason, the pure LC phases of the LaPO$_4$ system can be manipulated in the concentrated regime. It is sometimes difficult to distinguish unambiguously by polarization microscopy the nematic phase from the columnar phase because both mesophases are birefringent. Several points above the Iso-Nem biphasic range on the phase diagram (**Figure 2.17**) are thus still unclear whether they are in nematic or in columnar phase. Instead, SAXS experiments have been performed for different dilutions of one purified sample (**Figure 2.18.d**), indicating a swelling law behavior of bi-dimensional order with $q_{100} = \alpha \cdot \Phi^{1/2}$ (**Figure 2.18.e**). The prefactor α can be easily calculated for a hexagonal lattice with $\alpha^2 = 32\pi/(\sqrt{3} \cdot D^2)$. From the numerical fit of the data, the rod diameter can be estimated as approximately 8nm, which is roughly consistent with the value of 11 nm measured by SEM (**Table 2.1**). Note that some broadening of the Bragg reflections can be seen in the columnar range by increasing the rod volume fraction as shown in **Figure 2.18.d**. This is related to finite size effects originating from the concentration step of the particles, in which the LC domain size in the sample decreases by removing the solvent, increasing therefore the width of the Bragg peaks.[67]
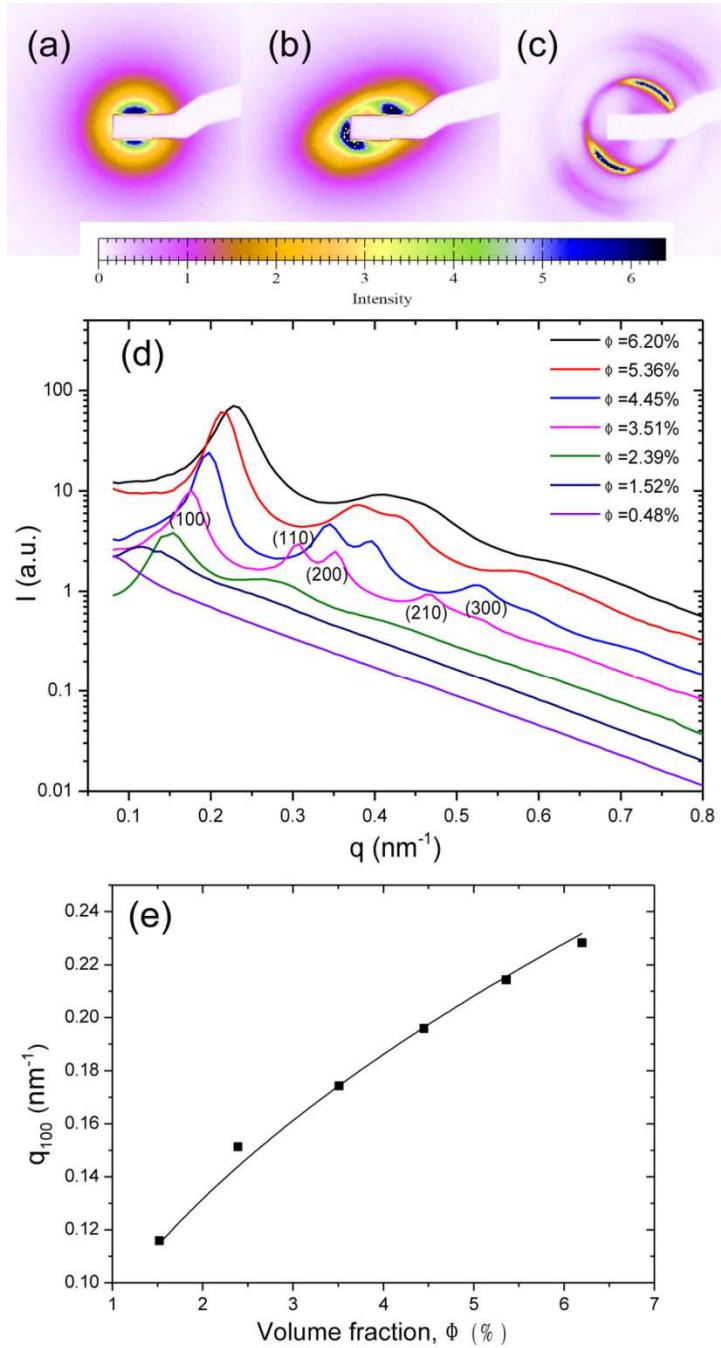
Figure 2.18. Typical diffraction patterns obtained by SAXS in (a) the isotropic liquid phase, (b) the nematic phase, and (c) the columnar phase. (d) Scattered intensity I as a function of the wave vector q for different volume fractions Φ of $LaPO_4$ suspensions. The Miller indices only shown for clarity at $\Phi=3.51\%$ indicate a hexagonal structure of the columnar mesophase. (e) Evolution of the position of the main Bragg reflection (100) with the nanorod volume fraction (Φ). The dark line is a data fit $q_{100}=\alpha \cdot \Phi^{1/2}$ characterizing a swelling law of a two-dimensional order.

In summary, a prominent liquid crystalline (LC) behavior of the LaPO$_4$ nanorods could be exhibited thanks to their outstanding colloidal dispersion stability achieved by optimizing the synthesis process and transferring into ethylene glycol (EG). Clear isotropic ↔ nematic ↔ columnar phase transition and separation mainly dependent upon the rod density (Φ) were observed by bulk sample measurement, polarization optical microscopy, TEM, and also SAXS. A full phase diagram was established based on the observation of many samples in different Φ, rod size, and ionic concentration. As predicted by Onsager's theory, rods with higher aspect ratio form nematic phase at lower Φ. Moreover, high ionic strength visibly increases the phase transition density by screening the surface charge associated with the effective rod diameter. SAXS results evidenced the existence of columnar phase that can hardly be distinguished with the nematic phase by polarization microscopy.

2.3. Conclusion

Optimization of the synthesis process by controlling the basic parameters such as precursor concentration and reaction temperature significantly improved the rod dispersion quality of the final product. It should also be emphasized that using a non-aqueous ethylene glycol medium dramatically eliminated the slow thermal aggregation kinetics that was inevitable in aqueous medium. As-achieved permanent colloidal stability became an initiative for the LaPO$_4$ nanorods to exhibit an outstanding liquid crystalline (LC) behavior. The fast isotropic ↔ nematic phase separation, clear tactoïds and Schlieren textures, and the large birefringence evidence that it is one of the best-performing mineral LC systems ever synthesized so far. It is now necessary to take note of its colorless transparent aspect and its capability as an efficient host of luminescent rare-earth phosphors. These intrinsic properties of our selected material, LaPO$_4$, are promising for real applications in optical devices beyond the confirmation of the good LC properties. The next chapters are dedicated to utilize such properties for light-modulating devices (Chapter 3) and also for developing a novel analytic method of diverse orienting objects (Chapter 4).

※ Experimental details ※

Synthesis of standard-rods

Equimolar (0.05M) aqueous (Milli Q) solutions of La(NO$_3$)$_3$ and (NH$_4$)$_2$HPO$_4$ were cooled down to 0°C in an ice bucket. Same volume of these precursor solutions are mixed and vigorously stirred for minutes in a flask. The stirred mixture had milky aspect due to the instant precipitation reaction generating LaPO$_4$ seed rods. The mixture was transfer into a reactor vessel. Lab-made cylindrical (diameter ~5cm / thickness > 2.5mm) glass tube with a volume ~200mL or a typical stainless-Teflon autoclave with a volume ~100mL were used as

a reactor vessel. ~20% of the volume was left unfilled considering the volume expansion during heating. The glass tube was sealed, or the autoclave was closed perfectly to avoid leak under high pressure, and then entered in the oven preheated to 170°C. After 3 hours, the vessel was cooled down to the ambient temperature. All the above steps from mixing to entering in the oven should have been swiftly conducted in less than 10 minutes to avoid aggregation and obtain the best colloidal dispersion quality.

Preparation of low-aspect-ratio-rods (lar-rods) and small-rods (s-rods)

Lar-rods were prepared by cutting the standard-rods sample under ultra-sonication during 3 hours. S-rods were synthesized without high temperature heat treatment for hydrothermal growth reaction, by leaving the precursor solution mixture under regular stirring during 4 days at the ambient temperature.

Washing and purification

After the synthesis, there exist a lot of residual ions (La^{3+}, NH_4^+, PO_4^{3-}…) that cause aggregation of particles. First step to remove these ions is washing by centrifugation and re-dispersion. The product colloidal suspension of $LaPO_4$ nanorods after synthesis were transferred into centrifuge tubes (30mL/tube) and centrifuged at 11000rpm during 1hour. The nanorods settled at the bottom of the tube showing sticky gel-like aspect, and the supernatant liquid was removed. 10mL of 0.01M aqueous nitric acid solution was poured in each tube and the tubes are vigorously agitated by vortex machine for about 30 minutes to perfectly re-disperse the nanorods. Re-dispersion after centrifugation is possible only once. If the centrifugation is repeated, nanorods were no more be dispersed again by agitation. Further purification was thus conducted by dialysis. 4 liter of 0.01M aqueous nitric acid solution (pH = 2) was prepared. Dialysis membrane (Spectra/Por®, MWCO = 12-14,000) had already been washed with distilled water several times and left in distilled water for more than 2 days to remove impurities. The washed nanorod suspension in the centrifuge tubes were transferred into the dialysis tube, entered in the dialysis tub, and moderately stirred with magnetic bar agitator for 2 days.

Transferring aqueous nanorods into ethylene glycol (EG)

Transfer was conducted by distillation. The volume of EG for the intended final nanorod concentration was calculated and mixed with the purified aqueous suspension in a round bottom flask. Water was selectively evaporated using a rotary evaporator (bath temperature = 50°C, vacuum < 20 mbar, rotation speed = maximum). As water distillation often causes an abrupt overflow, the vacuum pressure should be finely adjusted during the whole time of this step. After removing most of water in the suspension, a more powerful vacuum pump was used to perfectly remove remaining water under stirring. A careful manipulation was required to remove all water but not dry EG which occurs aggregation of nanorods.

Adjusting ionic strength

In many cases in previous works, addition of salts in the low-ionic-strength suspension has been typical method. But for highly concentrated viscous colloidal suspension, this method often causes local aggregation of particles before homogenization of salt concentration. Also, $LaPO_4$ nanorods in aqueous medium had a very narrow ionic strength range for stabilization, so there was no chance to adjust it before transferring into EG. Therefore in this study, dense colloidal suspensions in EG were prepared at ionic force ~0.1M as a result of concentrating ~10 times from aqueous suspension at 0.01M. And then these EG suspensions were dialysed again in pure EG to adjust the ionic force at lower range down to 10^{-3}M. Dialysis procedure is the same with that in water.

Charaterization

Olympus BX51WI optical microscope with modified geometry was used with a DTA1600E CCD camera for polarization optical microscopy. A detailed setup of the microscope is demonstrated in Appendix. High resolution transmission electron microscopy (TEM) and scanning electron microscopy (SEM) were performed respectively on FEI Tecnai F20 and Hitachi S4800 field electron gun scanning electron microscope (FEG-SEM). To identify the extent of aggregates, SEM samples were prepared by attaching nanorods on a negatively charged polystyrene sulphonate layer coated on a silicon wafer substrate. The nanorod size data were obtained by counting the length and diameter of 300 individual particles on different SEM images (for standard rods and lar-rods) and TEM images (for s-rods) from each sample. The estimated precision for the size determination is about 1 nm for standard rods and lar-rods, and about 0.2 nm for s-rods respectively. X-ray diffraction (XRD) pattern was obtained using Philips X'pert diffraction system working at CuKα radiation, and indexed comparing with the rhabdophane reference -JCPDS 46-1439. Small angle X-ray scattering (SAXS) measurements were carried out on the SWING beamline at the synchrotron radiation facility SOLEIL, with a sample to detector distance of 1384mm and with a wavelength of 0.103nm. The polarization optical microscopy to observe the LC texture and to perform the electro-optical measurements was conducted on 15μL of $LaPO_4$ nanorod suspensions deposited between a typical microscope slide and a coverslip. Nitric acid concentration (C_{acid}) was obtained by fitting the measured electric conductivity (σ) to the C_{acid} vs. σ curve of the reference nitric acid solutions. The mass concentration of the colloidal solution was obtained with a dried sample of a given volume, and the volume fraction was calculated dividing it by the density of $LaPO_4$ in rhabdophane phase, 3.94g/cm^3.

Chapter 3

Birefringence: Applications & Modeling

This chapter deals with a collective optical property, birefringence, of the aligned structure of colloidal $LaPO_4$ nanorods prepared in the way demonstrated in chapter 2. Birefringence enabled a facile observation of the liquid crystalline (LC) mesophases using a typical polarization microscopy. And it is a very useful property for devices to modulate polarization and transmission of light such as LC displays (LCD). The first objective of this thesis was to design active LC devices composed of mineral compounds, which has been hardly established.[68] If it were possible to make active mineral LC devices, a variety of novel applications should be possible taking many advantages of inorganic materials such as large transparency range and high thermal stability. In the first section, the electro-optical behavior – controlling birefringence with the external electric field – of the synthesized colloidal $LaPO_4$ nanorod suspensions is investigated, which was compared favorably to the performance of commercial organic LC materials. It is also investigated, in the second section, designing a thin film wave retardation device – often called in the conventional term 'waveplate' – by a directed-assembly of the nanorods. In order to fabricate a perfectly oriented structure of nanorods on the macroscopic scale, the LC property of the rod suspension was excluded but a thixotropic rhological property was exploited. Surprisingly, the values of birefringence (Δn) exhibited both by the electro-optical manipulation in the liquid suspension and from the solidified thin film waveplate are unexpectedly high. Theoretical modeling study on the birefringence of heterogeneous media in the final section provides the explanation for this, which was indeed due to the combination of intrinsic and form birefringence: a novel concept of engineering birefringence that is only possible using mineral materials.

3.1. Electro-optical behavior

The outstanding colloidal stability and the high optical transparency of the colloidal LaPO$_4$ nanorod suspension even for low ionic strength and high volume fraction (Φ) appear very attractive for investigations of its electro-optical properties targeting active light modulating devices. As isotropic, nematic, and columnar phases were observed, birefringence modulation by using both the electro-optical Kerr effect in the isotropic phase and the orientation switching in the aligned nematic or columnar phases could have been tested.

3.1.1. Elecro-optical Kerr effect

Electro-optical Kerr effect, discovered by John Kerr in 1875, is a phenomenon of generating birefringence from a material in response to the application of external electric field across it.[69] Most materials exhibit an electro-optical Kerr effect, which is usually visible with transparent materials, and it is stronger in some polar liquids composed of anisotropic molecules such as nitrobenzene ($C_6H_5NO_2$) or nitrotoluene ($C_7H_7NO_2$) (**Figure 3.1**). Kerr effect should be distinguished with the Pockels effect, a similar phenomenon that is often shown in some crystalline materials with a lack of inversion symmetry. The Pockels effect shows a linear variation of the refractive index according to the changing electric field, however, the Kerr effect displays a proportional relation to the square of the electric field as described with the following equation,

$$\Delta n = \lambda B E^2 \qquad \text{(Equation 3.1)}$$

where Δn is the induced birefringence, λ is the wavelength of light, E is the strength of the applied electric field, and B is the Kerr constant.
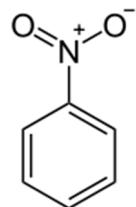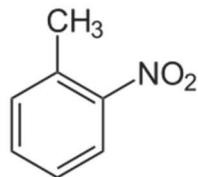
nitrobenzene   nitrotoluene

Figure 3.1. Molecular structures of nitrobenzene and nitrotoluene that perform the most significant electro-optical Kerr effect among conventional polar liquids.

Kerr cells

A Kerr cell is a device to modulate polarization states of light using the electro-optical Kerr effect, which is composed of a glass cell with electrodes filled with nitrobenzene. Some disadvantages of Kerr cells are the toxicity of nitrobenzene and the required voltage to switch birefringence as high as ~30kV, even though nitrobenzene has the highest Kerr constant ($4.1 \cdot 10^{-12}$ m/V^2) among conventional molecular liquids.[70] For this reason, use of a Kerr cells is very limited, and they are less frequently used than the Pockels cells that still require high voltage but composed of solid crystals.

Organic liquid crystal cells

Organic LC materials are abundantly used for electronic display devices of today. A basic principle of liquid crystal display (LCD) is to make each pixel as an electro-optical cell to switch light transmission by controlling the orientation of birefringent nematic phase of thermotropic molecular LC materials between crossed polarizers as shown in **Figure 3.2**.
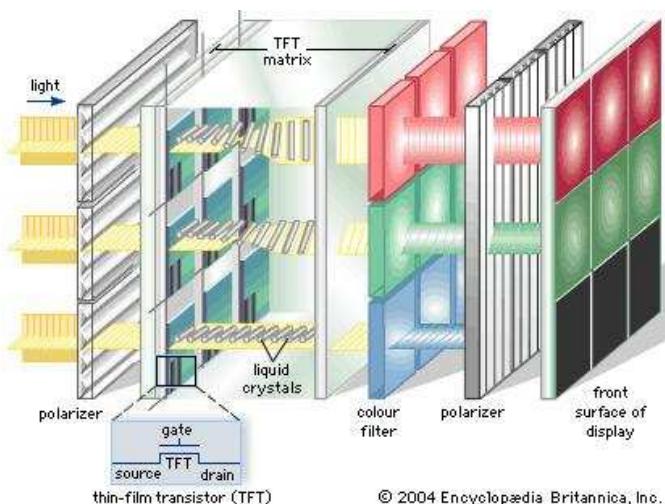
Figure 3.2. Schematic figure of the thin-film transistor liquid crystal display (TFT-LCD). *Figure taken from Encyclopedia Britanica 2004.*

Detailed discussion on the behaviors of organic LCs is out of the scope of this thesis. Yet, it should be noted that the Kerr constant of conventional thermotropic LCs is globally situated around 1-order of magnitude higher than that of nitrobenzene. For example, the Kerr constant of 5CB (4-Cyano-4'-pentylbiphenyl) molecules, a commonly used nematic LC, is $6 \cdot 10^{-11}$ m/V^2 in the isotropic phase at the temperature 1K higher than that for isotropic-nematic phase transition.[71] This value is about 1-order of magnitude higher than that of nitrobenzene, but still very low to be used for light electronic devices. Thus current LCD

technology is oriented to use an initially oriented nematic phase with a low voltage bearing some disadvantages such as high cost, limited viewing angles, and low switching speeds. As there is a need to overcome these problems, recent researches to enhance Kerr constant of organic LCs exploited blue phase LCs composited with polymers that reach 3-order of magnitude higher Kerr constant than nitrobenzene ($B > 10^{-9}$ m/V^2).[70, 72] In the following section, it is shown that this highest Kerr constant obtained with the state-of-the-art engineered organic LCs is conquered with the LaPO$_4$ mineral liquid crystalline suspension by a simple experimental observation of its Kerr effect.

3.1.2. Elecro-optical Kerr effect in isotropic LaPO$_4$ nanorod suspension

In-plane switching (IPS) cell

"In-plane switching" is a technology used for LCD devices, which involves arranging and switching of LC materials injected between two parallel glass substrates in a plane parallel to the substrates. This method was developed to solve the above stated problems of typical LCDs using twisted-nematic phase of thermotropic organic LCs. **Figure 3.3** shows a structure of a commercial IPS cell. There exist two part of transparent indium tin oxide (ITO) electrode coated on the bottom substrate with a comb-like geometry that are placed parallel with a constant gap width between each tooth. When a voltage is applied between the ITO electrodes, electric field is generated between the teeth that have opposite signs of field strength as shown with the red lines in the right figure. LC materials in the space between these electrodes may therefore align along the electric field parallel to the substrates.
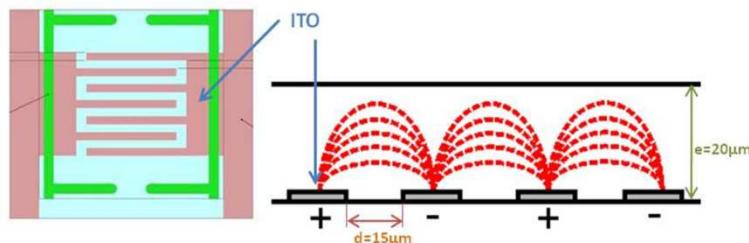
Figure 3.3. Geometry of a commercial in-plane switching cell for testing electro-optical properties of liquid crystals

IPS mode is advantageous for measuring and making a maximum use of the Kerr effect thanks to the in-plane alignment of LC materials. (A maximum retardation can be generated to a light traveling along the orthogonal axis of the substrate plane.) As a first part of the Kerr effect measurement in LaPO$_4$ nanorod suspension, commercial IPS test cells (Instec Inc) were used.

Isotropic LaPO₄ nanorod suspension in commercial IPS cells

To observe Kerr effect in the colloidal LaPO₄ nanorod suspension, an isotropic sample should be taken. And to avoid the short circuit problem under electric field, a well-purified (low ionic strength) sample by a full dialysis (ionic strength < 1mM) was taken. As previously shown with the phase diagram (**Figure 2.17**), the isotropic region of the colloidal LaPO₄ nanorod suspension at such a low ionic strength is placed at the volume fraction (Φ) lower than 1%. **Figure 3.4** shows the birefringence generated from an IPS cell filled with a sample at Φ = 0.66% under alternative sinusoidal electric field applied and gradually increased. Even in such a dilute regime, the commercial IPS cell (typically used to test organic LCs) displays a high light transmission under electric field expecting a large birefringence and a significant Kerr effect.
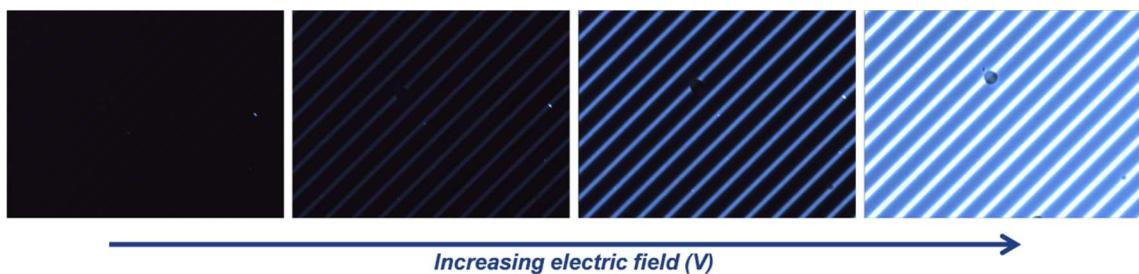
Figure 3.4. Polarization optical micrographs of an IPS cell filled with a LaPO₄ nanorod suspension in the isotropic phase (Φ=0.66%) under the applied AC electric field showing the birefringence change under increasing field strength. The IPS cell is angled 45° to the crossed polarizer.

A quantitative measurement of birefringence (Δn) is possible with a direct measurement of optical retardation ($\delta = \Delta nd$ (nm) / d = thickness of the birefringent medium) by using a Berek compensator (See Appendix) equipped with the polarization microscope. Another way to obtain Δn value is to measure the transmitted light intensity (I) across the IPS cell between crossed polarizer by using a CCD camera. In this case, the calculation of Δn is provided by the equation,

$$I = I_0 \cdot sin^2(2\theta) \cdot sin^2\left(\frac{\pi \cdot d \cdot \Delta n}{\lambda}\right) \qquad \text{(Equation 3.2)}$$

where I_0 is the intensity when the polarizer and analyzer are parallel, θ is the angle between the polarizer and the orientation of nanorods in the cell, that is here 45°.
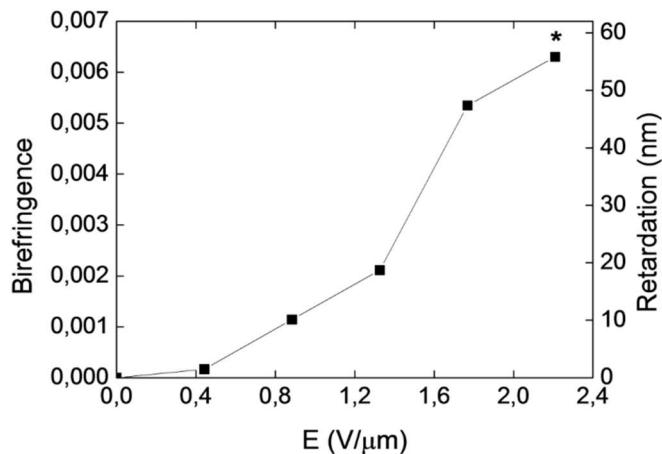
Figure 3.5. Variation of birefringence and optical retardation of an IPS cell (d = 8.8μm) filled with a LaPO$_4$ nanorod suspension sample (#J25 – 4th dialysis – Φ = 0.9%). A sinusoidal alternative electric field wave of 100kHz frequency was used. Short-circuit due to the initiation of electrolysis occurred at E > 2V/μm (starred point). *This data finally came out to be false due to the problem of commercial IPS cells.*

Measured birefringence and optical retardation values according to the applied electric field are shown in the diagram in **Figure 3.5**. Here their variation seems to globally follow the proportionality of Δn to E^2 as noted by **Equation 3.1**, except for the last point (starred) where the increasing tendency is reduced. Indeed, the starred point is at the E value over the short-circuit limit which was ~2V/μm for most of the suspension samples. At such a high voltage, bubbles start to be generated due to the electrolysis reaction consuming the electric current. This means a significant portion of the electric field serves for this electrochemical reaction rather than for the nanorod orientation.

A problem of commercial IPS cells

Analyzing the data obtained using the commercial IPS cells, it was found that the measured Δn values were too much higher than the expected values calculated by the theoretical model (Detailed theoretical analysis on birefringence is noted in the section 3.3). **Figure 3.6.a** is a diagram showing the variation of Δn according to the Wiener's theoretical model assuming a perfect orientation of nanorods and the experimental point corresponding to the starred point in **Figure 3.5**. Considering the alignment of nanorods under electric field at the experimental point is not perfect, there exists about 1-order of magnitude difference between this experimental result and the model calculation. Moreover, repeated measurements on the same sample suspension (Φ = 0.9%) in the same IPS cell show irreproducible and fluctuating Δn values (**Figure 3.6.b**).
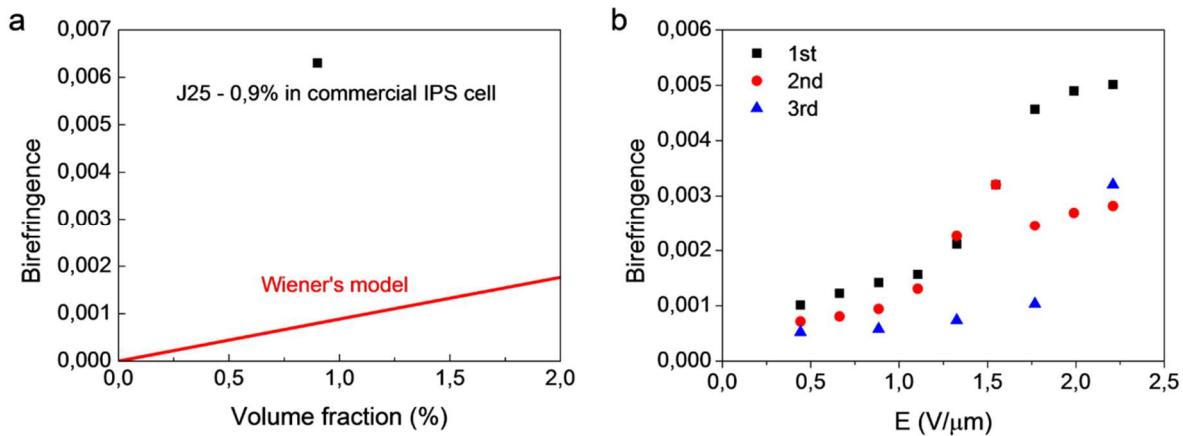
Figure 3.6. (a) A calculated birefringence curve (red line) according to the rod volume fraction by Wiener's model (See the section 3.3), and an experimental point obtained by using a commercial IPS cell (the starred point in **Figure 3.5**). (b) Experimental result of a repeated electro-optical measurement under varied electric field strength (100kHz, sinusoidal) in one commercial IPS cell filled with a sample suspension (#J28 – 2nd dialysis, Φ = 2.3%).

From these data it was suspected that the commercial IPS cell had some unexpected problems. And by testing a cell filled with a pure ethylene glycol, it was found that the commercial cells generate a considerable birefringence without any LC medium inside. This was indeed due to the strain-induced distortion of the glass cover plate of the cell. When a voltage is applied to the IPS electrode, the electric field geometry as shown in **Figure 3.3** induces strong attractive force between the top and bottom substrates on the whole area of the gap arrays. For this reason, a quantitative measurement of birefringence was impossible using the commercial cells. The data in **Figure 3.5** and **Figure 3.6.b** is therefore trustless. And all the reliable measurements were conducted using handmade cells as described below.

Isotropic LaPO$_4$ nanorod suspension in handmade IPS cells

The schematic design of our handmade IPS cell is shown in **Figure 3.7**. It is composed of a bottom substrate, a gold thin film electrode layer with a gap (30 ~ 100μm), spacer films outside of the gap (~60μm), and a coverslip. In this simple geometry with a single gap, there no more exists the problematic attraction between the two substrates generating the false birefringence, because the electric field is generated on a very small area of a single gap and the distance between the spacers is shorter.
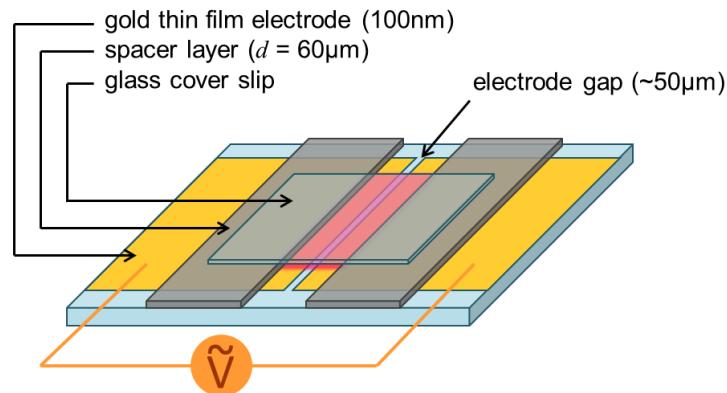
Figure 3.7. Geometry of the handmade IPS cell. Red colored region is where the LaPO$_4$ nanorod suspension is filled.

Figure 3.8 shows the birefringence change on the electrode gap of a handmade IPS cell filled with an isotropic sample (Φ=3.2%) obtained from the upper phase of a macroscopically phase-separated suspension. It gives the same tendency of higher transmission under stronger electric field as shown in **Figure 3.4** for a commercial cell. Here there is only one gap between electrodes, thus only one linear area is brightened when birefringence is generated due to the orientation of rods under electric field.

Figure 3.8. Polarization optical micrographs of a handmade IPS cell under electric field (thickness = 60µm, gap distance = 51µm) filled with an isotropic phase LaPO$_4$ nanorod suspension (Φ=3.2%, obtained from the upper phase of a macroscopically phase-separated suspension). Electric field strength is 0V/µm, 0.693V/µm, and 1.386V/µm respectively for the images from left to right.
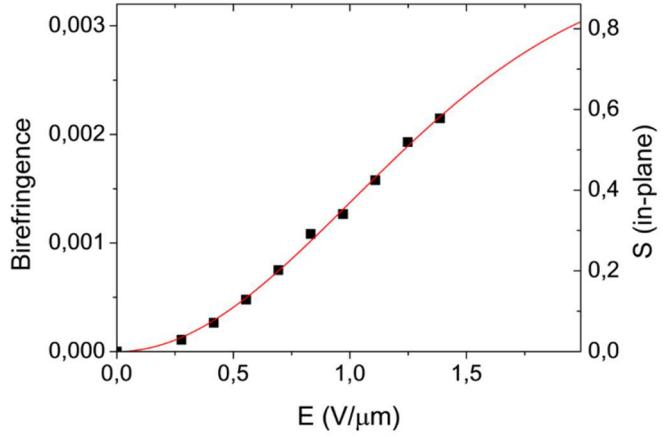
Figure 3.9. Birefringence vs. electric field strength measured on the handmade IPS cell filled with an isotropic sample suspension (Φ=3.2%) corresponding to the images in **Figure 3.8**. Red line is a fitting result with the **Equation 3.3** for Kerr effect being saturated at high E and the right-side axis indicates the in-plane orientational order parameter (S) normalized based on the fitting result.

The measured values of birefringence from this handmade cell according to the electric field strength are shown in **Figure 3.9**. It had been confirmed that repeated measurements provide reproducible data. The maximum *Δn* value obtained near the short-circuit voltage is placed near the calculated value by the theoretical model (See the section 3.3). With such a reliability using the handmade cell, here again, the increasing curvature of *Δn* seems to follow the proportionality of *Δn* to E^2 for the first 5 points as noted by **Equation 3.1**. But for a more accurate analysis, the tendency of saturation of *Δn* at high voltage should also be considered because **Equation 3.1** is only valid at low level of orientation far from saturation. A modified equation for Kerr effect reflecting the saturation at high degree of orientation at high voltage was proposed as[73],

$$\Delta n = \Delta n_{sat} \cdot \left(1 - \exp\left[-\left(\frac{E}{E_s} \right)^2 \right] \right)$$

(Equation 3.3)

where *Δn*$_{sat}$ is the induced birefringence at saturation and E_s is the characteristic electric field strength for saturation. Kerr constant can then be deduced as,

$$B = \frac{\Delta n_{sat}}{\lambda \cdot E_s^{\ 2}}$$

(Equation 3.4)

The red line in **Figure 3.9** is a plot of the fitting curve by **Equation 3.3,** and it gives Δn_{sat} = 0.00355 and E_s = 1.431V/µm. The estimated orientational order parameter (S) is noted with another right-side axis on the same diagram due to its direct proportionality to birefringence (S = $\Delta n / \Delta n_{sat}$) when $\Delta n \ll 1$.[74-75] One can see S increases up to 0.6 at below the threshold voltage triggering the electrolysis reaction (bubble generation). S noted here only implies the in-plane contribution of the rod orientation because birefringence is unchanged by the out-of-plane angular dispersion. The value of Kerr constant is obtained by **Equation 3.4** as B = 2.9 · 10^{-9} m/V^2. It is 3-order of magnitude larger than that of nitrobenzene, 2-order of magnitude larger than that of typical thermotropic organic LCs[71], and comparable with the Kerr constant that could be obtained only with the polymer-composited organic blue phase liquid crystals.[72-73] More discussion on its useful application together with the detailed theoretical analysis is noted in the section 3.3.

3.1.3. Electro-optical measurement in nematic phase LaPO₄ nanorods suspension

This work was conducted together with Dr. Eric Grelet at Centre de Recherche Paul Pascal in Bordeaux (CRPP).

Experiments were achieved both on a nematic phase at Φ = 1.55% and on a columnar phases at Φ = 4.34% respectively, at low ionic strength, in an experimental cell made of an ITO electrode with a gap and a glass coverslip. Typical birefringent texture was observed initially, where the LC domains were randomly oriented at the macroscopic scale (**Figure 3.10.a**). When the electric field was applied, the nanorods on the gap were aligned along the electric field inducing a bright birefringence on this area where the orientational order parameter (S) is close to 1 for E > E_S (**Figure 3.10.b**). When the electric field was turned off, the macroscopic alignment - free of topological defects - is conserved because no elastic force exists to restore the initial random alignment (**Figure 3.10.c**). The value of S by spontaneous orientation without electric field is slightly less than the one driven by electric field, therefore it relaxed back in about 1 hour resulting in a decrease of the birefringence. Quantitative measurements of the orientation and the relaxation of the LC phases by an electric field are shown in (**Figure 3.11**). Interestingly, the critical field required to fully orient both the nematic and the columnar phases is found to be quite low (E_S~0.05V/µm). It must be noted that in these experiments, the initial values of the birefringence (at zero field) depends on the arbitrary orientation of the domain where the measurement is made. The final value of the birefringence (4.4·10^{-3}) must be considered relatively to the volume fraction of nanoparticles (Φ=4.34%) and discussed together with the theoretical model in the section 3.3. The long relaxation time is also peculiar as this enables to maintain the once switched state for a long while after turning the field off.
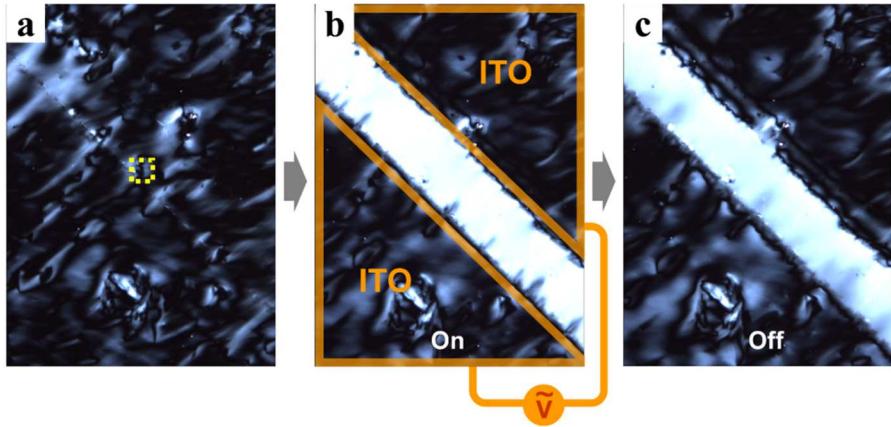
Figure 3.10. Polarization optical micrographs of a nematic suspension (Φ=1.55%) in a LC cell with a thickness about 45µm. This cell is made by a glass coverslip and an ITO electrode with a gap width of 170µm has been performed for applying an alternative in-plane electric field, E. (a) Before applying the electric field, the samples exhibit some birefringent domains. (Dashed yellow box indicates the zone where the birefringence was measured using Berek compensator) (b) During application of a sinusoidal electric field at a frequency of 400kHz inducing the orientation of nematic or mesophase in the gap showing large birefringence. (c) When the electric field is switched off, relaxation of the nanorod alignment is observed with a decrease of the associated birefringence.
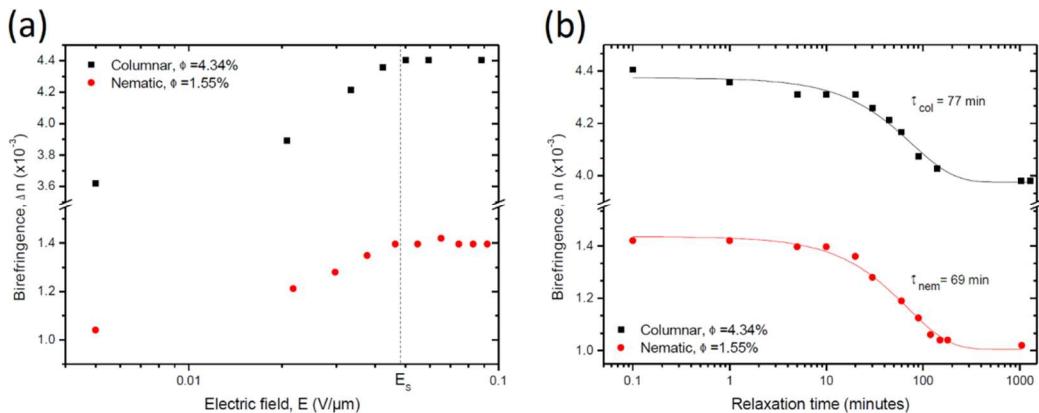
Figure 3.11. (a) Variation of the induced birefringence as a function of the applied electric field in both nematic and columnar phases. (Birefringence was measured on a position corresponding to the dashed box in **Figure 3.10.a**) (b) Relaxation of birefringence according to the time passed after the electric field is switched off, corresponding to an exponential decay with a characteristic time τ of about 1 hour in both phases, as shown by the solid lines in graph (e).

3.1.4. Prospect

There exists only a little number of mineral liquid crystals (MLC) that show a notable electro-optical behavior. And no clear example of a practical application for active devices has been reported up to now. This is presumably due to the optical characteristics of MLCs

independent of the electro-optical performance such as the light absorption and scattering of mineral particles that harm the transparency of the suspension. Otherwise the long-term stability and sedimentation problems discussed at the beginning of this chapter had not satisfied the device application. Elimination of such problems in the $LaPO_4$ nanorod suspension together with its outstanding electro-optical properties shed light on the utilization of MLCs for a practical electro-optical device.

Quantitatively speaking, the optical transmission contrast in the <on/off> phase and <0°/45°> angles repeatedly measured on our IPS Kerr cells were generally higher than 0.99 while the Kerr constant reached $3 \cdot 10^{-9}$ m/V^2. Therefore, a half-wave switching device for visible light with a low rate of light loss (< 5%) can be made using a thin Kerr cell (d < 200µm) that requires a moderate applying voltage. Considering the nematic phase switching, the hour-scale relaxation time, and very low applying voltage (0.05 V/µm) may be advantageous to make novel optical devices such as smart windows or low power portable display devices.

Finally, it should be emphasized that the application of a mineral suspension would also benefit from its low production cost compared to expensive organic LC compounds, and from the stability of the mineral mesogens under UV irradiation or large flux of light. This enlarges the application range including UV light and high power lasers which are always a nuisance for organic materials.

In summary, the $LaPO_4$ nanorods stabilized in EG medium exhibit an efficient electro-optical Kerr effect: orientation under external electric field generating large birefringence. This mineral system shows a very large Kerr constant ($3 \cdot 10^{-9}$ m/V^2) that is 3-order of magnitude higher than nitrobenzene typically used for Kerr cell devices. This value obtained only at Φ = 3.2% challenges the highest Kerr constant ever observed from a particular organic blue phase LC material. Spontaneously oriented nematic samples also show an efficient field-induced re-orientation that is maintained for long time (~1 hour) even after switching off the voltage. Such an excellent electro-optical property together with the high transparency on the entire UV-Vis-IR range is promising for a variety of applications in active light modulating devices.

3.2. Thin film waveplates

LC organization is a smart way to make an oriented structure of anisotropic particles in the liquid phase. If the orientation in the nematic or columnar phases can be maintained after removing solvent, an organized solid structure could also be made. And such structure made in form of thin films would be beneficial for making devices exhibiting a fixed large amount of birefringence. Indeed, rod-oriented solid structure is easily observed by simply drying solvent from a droplet of LC suspension on a substrate. However, the problem comes from

the typical texturing of the LC mesophases. Even though the orientational order (S) is very high in a small nematic domain in the microscopic scale, the director of S is always fluctuating in the mesoscopic scale as it was observed and shown in the previous chapter (See **Figure 2.15**). Dried samples of such LC suspensions also maintain the same texture making it inefficient as for optical devices requiring homogeneous directional birefringence. Therefore, controlling the orientation direction (removing or avoiding texturing) is the key issue when making thin films of oriented nanorods. In this section, it is demonstrated how a typical directed-assembly technique can be applied to fabricate solid thin films composed of homogeneously oriented $LaPO_4$ nanorods. Ironically, stabilized LC suspensions could not be used in this case because of the strong texturing effect was unavoidably. Instead, a breakthrough was made using a 'rod gel' phase suspension that shows a peculiar rheological property called 'thixotropy'.

3.2.1. Shear directed-assembly of nanorods

Anisotropic objects in flowing liquids tend to orient along the direction of shear. This is a ubiquitous effect independent of the scale of the objects such as from floating logs on a river down to molecular liquids. To be exact, the driving force of orientation is the shear force present in flow that pulls an end of the anisotropic object to turn along the flow. For the microscopic objects, this phenomenon has often been observed also with birefringent optical properties of aligned particles such as for observing LCs. The relation between the shear profile and the optical effect in anisotropic liquids had earlier been investigated and noted as 'Maxwell effect'. According to this theory, the applied shear stress and the generated birefringence has a direct proportionality if far from saturation.[76-77] This effect thus has been frequently used to analyze rheological properties of complex liquids (Application of this concept in our system is shown in Chapter 4). Making use of this phenomenon could also be a possible strategy for the assembly of colloidal particles with anisotropic forms into organized solid structures, which is an arising task considered a lot in recent research trends. Indeed, this strategy has often been used to make optically or mechanically anisotropic polymer materials with molecular orientation.[30, 78] It is nevertheless not straightforward for colloidal systems since the orientation occurs only in the presence of shear which is hardly preserved during the solvent evaporation.

Problematic: relaxation & texturing

The difficulty of applying the shear-aligning behaviour for the directed-assembly of rigid particles is that, in general, oriented particles in flowing liquids rapidly relax back into random disorder at rest. This relaxation time in the isotropic phase is typically in millisecond scale which is much faster than the timescale for the drying process through evaporation of the solvent. One possible and convenient method to maintain shear force during evaporating the solvent is spin-coating involving strong centrifugal forces by rotating the substrate. Some reports have shown the orientation of rod-like colloidal particles in this way (**Figure 3.12**).[5-6,

[79] But there has been an obvious limit in controlling the orientation and thickness as the shear force is applied radially and changes continuously during the solvent evaporation.[79]
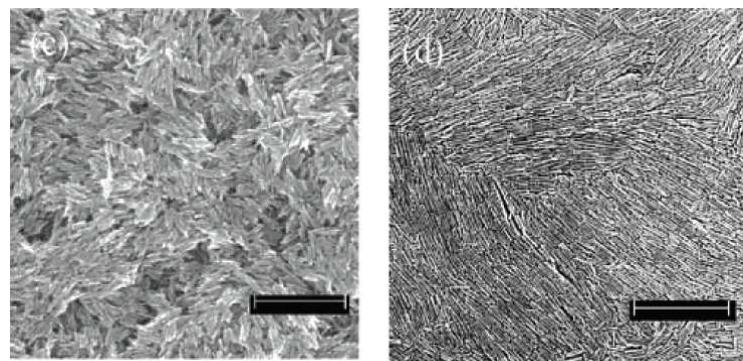
Figure 3.12. (a) SEM images of spin-coated films of ZnO nanorod caped with different ligands (left – butylamine / right – octylamine). *Figures taken from reference* [79]

For this reason, there have been some efforts to use liquid crystalline (LC) colloidal suspensions.[80-81] Nematic LC domains would be re-oriented towards the direction of an applied shear flow and the relaxation of individual particles may not necessarily occur even when the flow stops.[82-84]   However, as explained by Leslie-Ericksen theory[85-86], sheared nematic mesophase shows complex rheological properties that induce irregular flow motions like tumbling of the directors of the nematic domains. Flowing nematic suspensions thus render typical polydomain textures on the mesoscopic scale (1~100µm) where the directors of the domains are angled with each other.[87-89] In order to obtain a homogeneous orientation up to macroscopic scale without such textures, according to the scaling law, an extremely high shear rate ($\dot{\gamma}$) should be applied to refine the characteristic domain size as small as the size of individual particles.[87, 90] Experimental results on different types of LC samples show that shear rates at least $\dot{\gamma} > 100s^{-1}$ are required for non-textured state[91] as shown in **Figure 3.13** for the case of nematic *fd* virus suspension and organic LC polymers. And even if a nematic sample fully aligns at such a high $\dot{\gamma}$, we observed the texture reappeared when $\dot{\gamma}$ was decreased to evaporate the solvent. When spin-coating was used for a colloidal nematic suspension, the orientation was quite successful compared to the cases when isotropic suspension was used (**Figure 3.14**).[6] But there always exist the limited orientation confined in radial direction and the difficulty of controlling thickness that makes it unpractical for device applications. Therefore, it can be concluded that using pure LC suspensions is hardly compatible with the typical methods for colloidal self- or directed-assembly that requires a quiescent removal of the solvent.
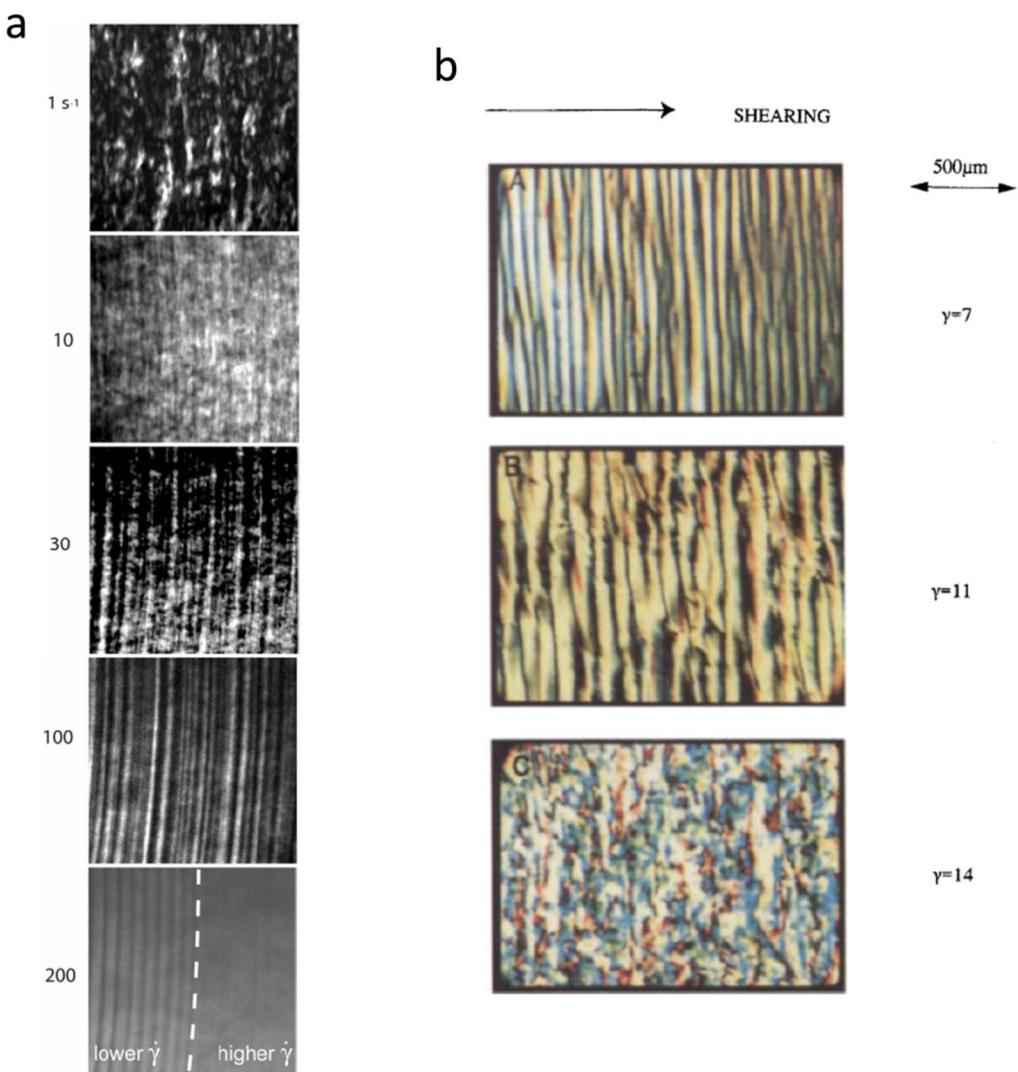
Figure 3.13. Polarization optical micrographs under shear with different steady state shear rates of nematic *fd* virus suspension-(a) and organic LC, poly-benzylglutamate-(b). *Figures taken from reference* [89-90]
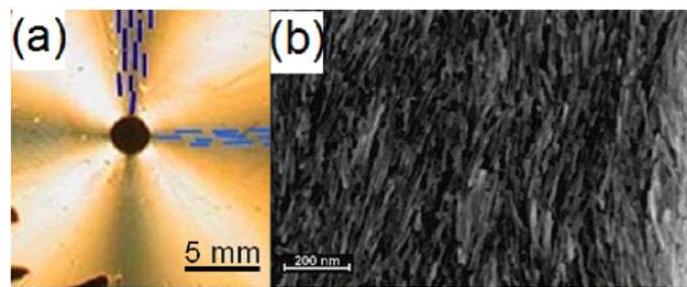
Figure 3.14. (a) Photograph of a rutile nanorod film obtained by spin-coating of a nematic suspension, observed between crossed polarizers. (b) SEM image of the surface of the same film. *Figures taken from reference* [6]

63

Solution: Thixotropic gels

Our approach is to avoid texturing not using the stabilized LC phase but using a rod gel phase at the high ionic concentration taking benefit of its thixotropic property. Thixotropy is a property that some visco-elastic gels (or fluids) lose its visco-elasticity under shear and recover it a while after removing the shear. Gelation of a colloidal suspension generally occurs when the electric double layer is screened by the increase of ionic concentration, so that the particles become attractive and aggregate with each other possibly making percolating networks.[22] In case of anisotropic particles like nanorods, the percolation threshold density (i.e. gelation density) appears to be much lower compared to isotropic particles due to its inverse proportionality with the rod aspect ratio ($\Phi_{gel} = 0.7 \cdot D/L$).[25, 27] And such rod gels with relatively low Φ (**Figure 3.15.a**) often show dramatic thixotropy so that the percolating network breaks down under the application of shear stress and the suspension turns into a flowing sol state.[92-93] Also, these rod gels do not display the typical LC textures though they are somewhat birefringent because the suspension is not stabilized for the particles being free to move.
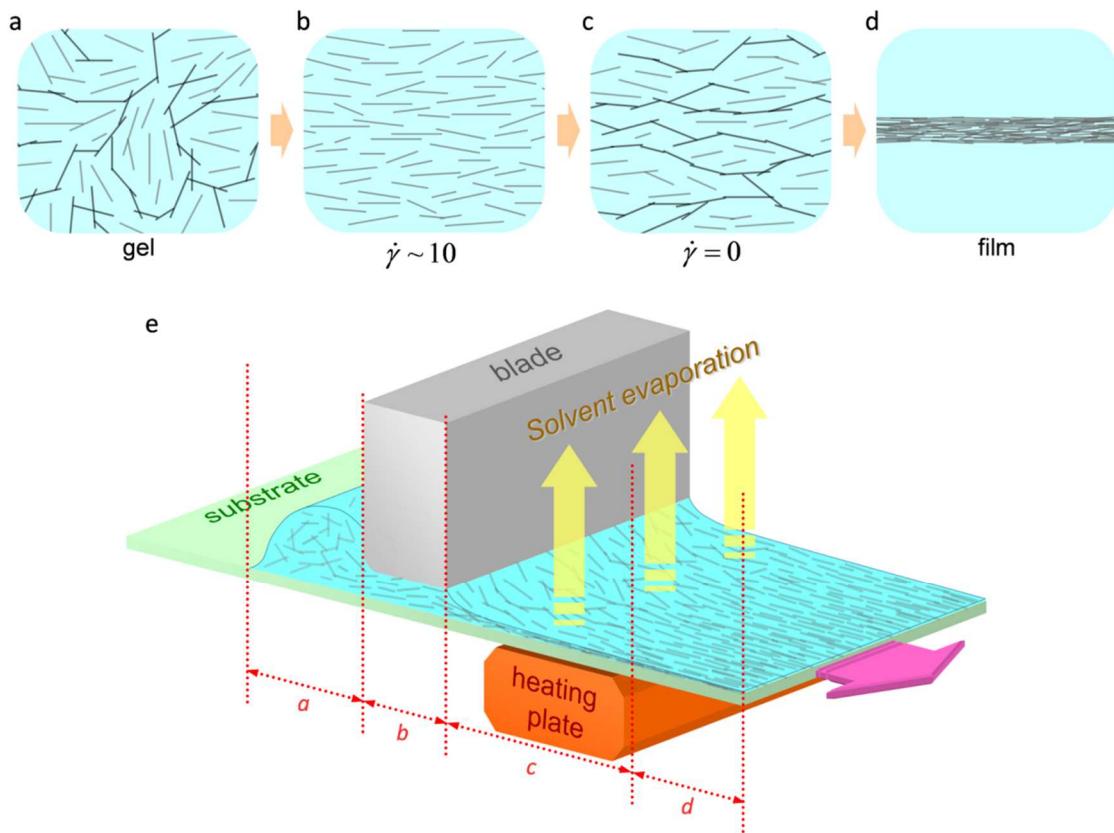
Figure 3.15. Schematic snapshots of nanorods in the thixotropic suspension at each step of the coating process: (a) gel with random networks, (b) sheared sol where the networks breakdown, (c) gel with aligned networks after shear, and (d) cross section of the aligned film after drying solvent. (e) Schematic illustration of the blade coating process to fabricate aligned nanorod thin films. The rod suspension state at each section, *a–d*, corresponds to the above snapshots (a)-(d).

From here, it can be expected that shearing a thixotropic rod gel with a moderate $\dot{\gamma}$ may efficiently induce such a gel-to-sol transition and simultaneously the orientation of rods as they recover the individual mobility (**Figure 3.15.b**). And when the flow stops, the attractive interparticle forces in the absence of shear stress would lead the sol to turn back to a gel state, thus freezing the rod orientation only disturbed within the short range that is to say without texturing (**Figure 3.15.c**). At this state, the solvent could be quiescently removed by evaporation at rest – without shear flow – preserving the frozen structure of rod orientation. Even though the orientational order parameter, ($S = <3cos^2\theta – 1>/2$)[88], achieved at this state with a moderate $\dot{\gamma}$ (to maintain the homogeneous orientation and the continuous evaporation of solvent) and altered by gelation, may not be very close to unity, it may be further improved during the drying step by the confinement within the film and the geometrical aspects of hard rod packing, leading finally to a very high degree of ordering ($S \approx 1$) (**Figure 3.15.d**). **Figure 3.15.e** schematically shows the simple blade coating process designed to fabricate thin films of aligned nanorods in this way. A phase-tuned nanorod suspension is deposited on a substrate moving at a constant speed (500µm/s) under the coating blade with a controlled gap width (~50µm). The blade was designed to have a large drag area parallel to the substrate. During the drag of the suspension by the blade, a constant shear rate ($\dot{\gamma} \sim 10s^{-1}$) is applied generating a Couette flow in the gap thus uniformly shearing the suspension. After passing through the blade, the substrate is heated to evaporate solvent and solidify the film. If a thixotropic rod gel is used, the organization state of the rods in each section (*a* to *d*) of the coating steps in **Figure 3.15.e** may correspond to the schematic snapshots in **Figure 3.15.a-d**.

Figure 3.16. Photographs of a phase tuned LaPO$_4$ nanorod suspension in ethylene glycol showing a dramatic thixotropic behavior, left – original gel state, middle – sol state after stirring, right – returned gel state after setting the sol inclined.

The gelation density mentioned above ($\Phi_{gel} = 0.7 \cdot D/L$) is lower than the Iso-Nem transition density ($\Phi_{Iso-Nem} \sim 4 \cdot D/L$) as described by the Onsager's model.[2] Thus colloidal gels composed of a percolating nanorod network can easily be prepared by adjusting the ionic concentration of the typical LaPO$_4$ nanorod suspension in EG. **Figure 3.16** shows the dramatic thixotropy observed from a phase tuned LaPO$_4$ nanorod gel suspension. Though

this is a qualitative observation without specific rheological measurements (the few amounts – typically a couple of milliliters – of our synthesized products were not enough for the measurement using conventional rheometers), the strong thixotropic property of the rod suspension is clearly proved with this figure. It was also confirmed experimentally that the amount of $\dot{\gamma}$ required for such rod orientation in the rod gel was only ~10s^{-1} as anticipated, which was suited for the typical blade coating techniques applicable and easily scalable to the roll-to-roll process.

Figure 3.17.a is a phase diagram (the same type with **Figure 2.17**) reconstructed with the experimental points of rod suspensions tested for the directed-assembly by the blade coating method with the above stated strategy. It can be checked again here that sol-gel transition of the LaPO$_4$ nanorod suspension occurs at the ionic concentration (C$_{ion}$) near 40mM. The spontaneous LC phase transitions (isotropic ↔ nematic ↔ columnar) were observed only in the sol state (C$_{ion}$ < 40mM) according to the rod volume fraction (Φ) where the individual nanorods obtain the mobility. To tune the suspension as a prominently thixotropic rod gel phase as in **Figure 3.16** for a successful directed-assembly, the ionic concentration was adjusted at 40mM < C$_{ion}$ < 100mM and the volume fraction at Φ > 3% (black circles in the phase diagram). When C$_{ion}$ > 100mM, even though they are globally in gel phase, the suspensions became too much thick which are irreversible to return to sol phase under shear. And when Φ < 3%, the gel re-formation was too slow. The polarization optical micrographs of each different phase in liquid state (A-gel, B-nematic, C-columnar, D-biphasic and E-isotropic) are shown in **Figure 3.17.b**. The rod-gel phase-(A) shows some kind of perturbed birefringent texture that doesn't have domains with a visible size due to the microscopic structure schematized in **Figure 3.15.a**. Besides, the other LC sol phases-(B, C, and D) display clean textures with the characteristic domain sizes roughly around 100μm (The size of the image is 340μm × 340μm).

In order to investigate the influence of those different colloidal phases on the film structure, coatings were prepared starting from these samples and their optical anisotropies were also characterized between crossed polarizers (**Figure 3.17.c**). When the isotropic phase-(E) was blade-coated the film shows very low birefringence without specific orientation indicating there is no significant orientation due to the fast rod relaxation out of shear. When the stabilized LC phases-(B-D) were used, their own textures that are elongated due to the shear appeared on the films. It is because the moderate $\dot{\gamma}$ applicable with the given coating method is much less than that to refine these textures as described above. By contrast, a perfectly aligned film could be prepared using the gel phase-(A) as the film made of it shows homogeneous directional birefringence without textures or haze. The optical transmission contrast – described as $(I_{45°} – I_{0°})/(I_{45°} – I_{0°})$ – measured on this film is 0.994 indicating that the film is composed of a highly oriented large single-domain. And such a high orientation could be obtained only in the gel phase showing strong thixotropic behavior (black circles in **Figure 3.17.a**). Therefore it is evidenced that using thixotropic rod gels for the directed assembly by a simple blade coating method can be considered as a prospective strategy.
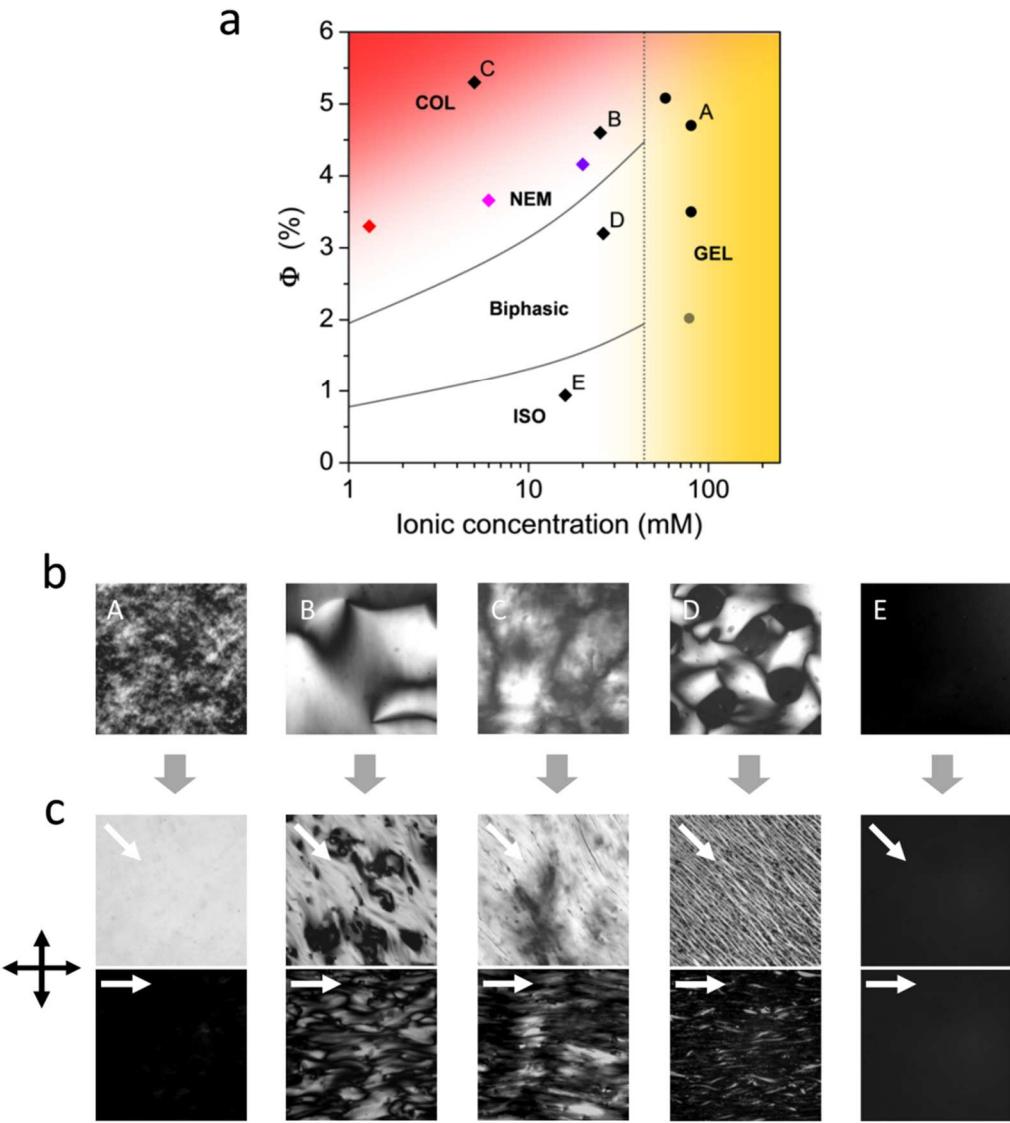
Figure 3.17. (a) Phase diagram of LaPO$_4$ nanorod suspension in ethylene glycol. (b) Polarization optical micrographs of different phases corresponding to the ▲ points (A-E) in the phase diagram. (c) Polarization optical micrographs of the aligned nanorod films prepared from each phase (A-E). The orientation of the crossed polarizers is indicated by the black arrows. On each micrograph, the white arrow indicates the coating direction. Image area is 340μm × 340μm.

In **Figure 3.18.a,** the optical contrast of films made at various $\dot{\gamma}$ using one sample suspension tuned in different sol-gel phases by varying C$_{ion}$ (Φ gradually changes due to the intrusion of solvent during dialysis). When using a thixotropic gel phase (C$_{ion}$ = 60mM), a high contrast values close to 1 were obtained in a $\dot{\gamma}$ range of 6~70s^{-1}. However, the highest contrast obtained using nematic sols at different C$_{ion}$ was less than 0.8, which is due to the mesoscopic textures as shown in **Figure 3.17.c**. In case where $\dot{\gamma}$ > 100s^{-1}, even though the instant orientation during shear could be better, the optical quality of all films drops regardless of the phase states because the solvent evaporation cannot be kept homogeneous. In this regard,

maintaining high heating temperature is also important to steadily and rapidly evaporate the solvent. To confirm the advantageous thixotropic property, the relaxation of the optical contrast on sheared gel and nematic sol were observed over time in liquid state without drying (**Figure 3.18.b**). A sheared thixotropic gel maintained its very high contrast for over a hundred minutes. While a nematic sample quickly lost the initial value of 0.84 due to the free relaxation of the elongated textures (not relaxation of individual nanorods), even though the most viscous nematic sample at the lowest C_{ion} was chosen. This texture relaxation behavior is also visualized in **Figure 3.19** as polarization micrographs taken at each time of the measurements corresponding to **Figure 3.18.b**. In case of stabilized nematic LaPO₄ nanorod suspension (**Figure 3.19.b**), one can see the typical texture of sheared nematic phase similar to that observed in the other LC materials (**Figure 3.13**). But in case of using thixotropic gel suspension (**Figure 3.19.a**), though tiny textures are slowly generated decreasing a little the value of optical contrast – presumably due to the micro-phase separation effect – it is very slow and seems quite effectively being frozen by gelation. Taking into account of all these results, our strategy and interpretation of using thixotropic rod gel suspension for the shear-directed assembly of LaPO₄ nanorods into a large homogeneous thin film could be said correct and prospective.
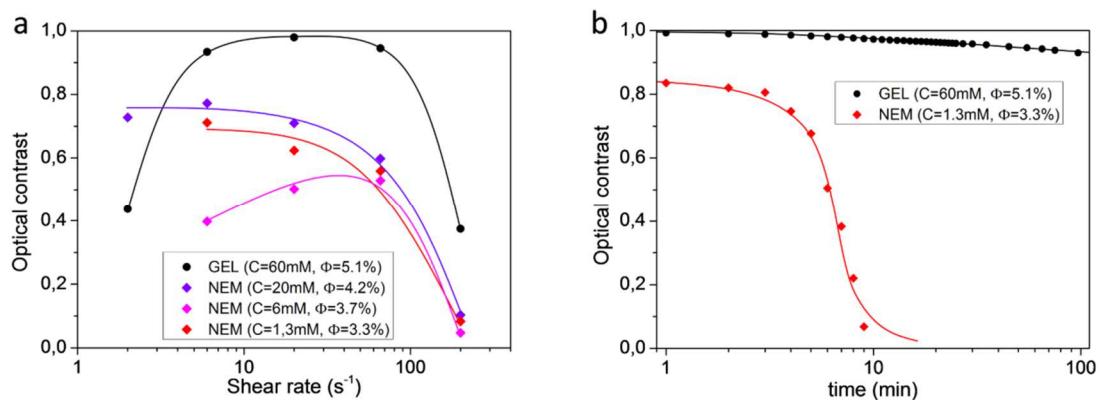
Figure 3.18. (a) Optical constrast, $(I_{45°} – I_{0°})/(I_{45°} – I_{0°})$, as a function of coating shear rate of films made of rod suspensions with tuned phase corresponding to the experimental points in **Figure 3.17.a** (b) Relaxation of optical contrast of liquid films after shearing thixotropic gel and nematic sol suspensions (without drying solvent).
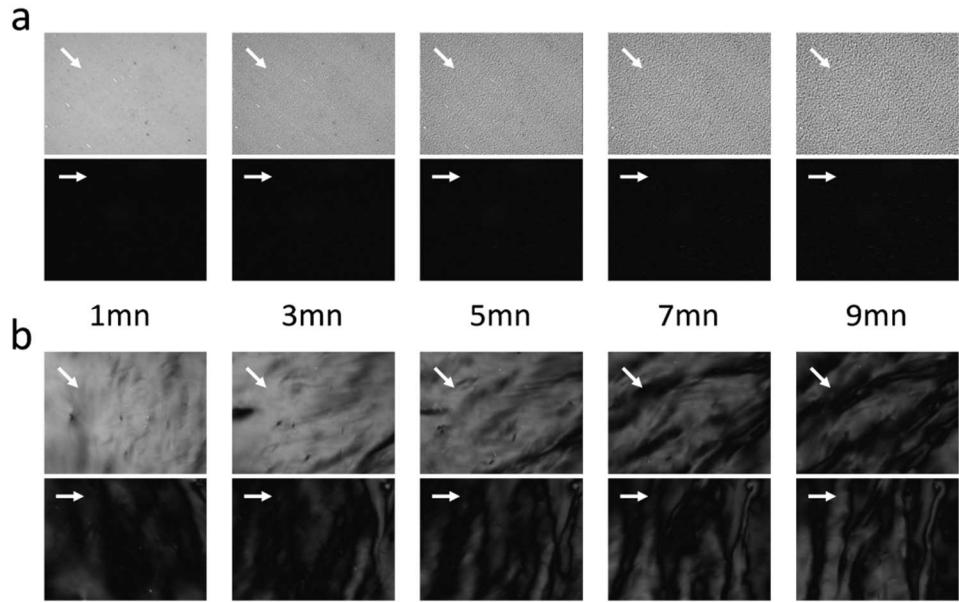
Figure 3.19. Polarization optical micrographs of the blade-coated LaPO$_4$ nanorods suspensions taken at each time after coating without drying solvent: (a) thixotropic rod gel (C$_{ion}$ = 60mM, Φ = 5.1%), (b) nematic sol (C$_{ion}$ = 1.3mM, Φ = 3.3%). Data corresponding to **Figure 3.18.b**.

3.2.3. Aligned LaPO$_4$ nanorods thin film waveplate

Rod oriented structure

SEM images of a film showing high optical contrast due to the homogeneous unidirectional birefringence made in the way described above are shown in **Figure 3.20**. In this film, all the nanorods are aligned parallel among each other and in-plane parallel to the substrate. It is also verified with the cross section image that such alignment is the same throughout the whole thickness of the film. Such an alignment quality was observed on the whole macroscopic area of the film in the centimeter scale made of the thixotropic rod gel suspension. This is a clear evideince for the excellent alignement of the nanorods only by the proposed method. There exist very small number of rebellious particles out of orientation, but they don't seem to have a significant optical effect considering their proportion. Besides, the regularly existing cracks should be responsible for the film's scattering property as their size is comparable with the wavelength of light (UV-Vis). This will be discussed in the next section for the optical properties of the film.
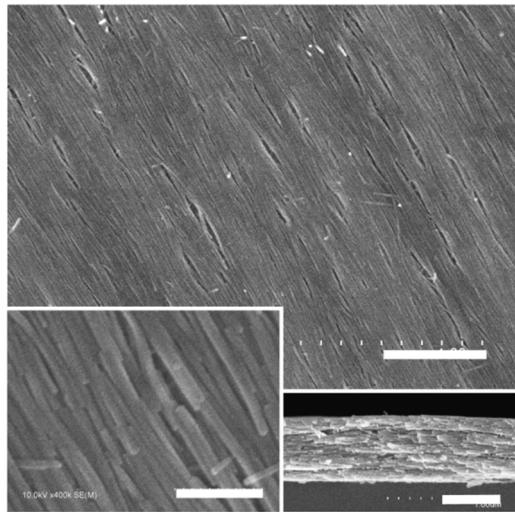
Figure 3.20. SEM images of the surface and cross section of an aligned LaPO₄ nanorod film fabricated by shear-directed assembly using a thixotropic rod gel suspension. (scale bars indicate 500nm–*top and right*, and 100nm–*left*).
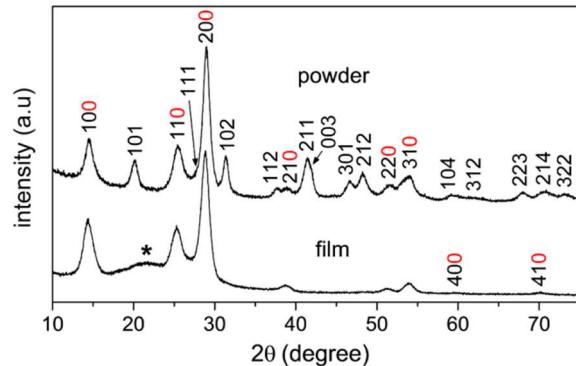
Figure 3.21. XRD patterns of LaPO₄ nanorods powder and the aligned thin film with the corresponding indexation (taken from JCPDS 46-1439). The powder pattern is identical to **Figure 2.7.b**.

Interestingly, the XRD pattern of the same film (**Figure 3.21**) is totally different from that is taken from a powder sample of the same nanorods. On this pattern, there exist only the *hkl* peaks with *l* = 0 (the starred broad peak is due to the glass substrate). Indeed, the absence of the peaks for *l*=1,2,3... that are seen on the powder XRD patterns evidences again the alignment of all nanorods parallel to the substrate, The hexagonal c-axis along the long rod axis is always parallel to the substrate thus making those peaks invisible.

Optical properties

Thanks to such an excellent orientation and packing of the LaPO$_4$ nanorods, the light scattering aspect of the film is minimized so that a large size film sample deposited on a glass slide (7.5cm × 2.5cm) exhibits high transparency (**Figure 3.22.a**). The light transmittance spectra in Figure 3.2.10.a shows that a high transparency spans over the entire UV-Vis-IR range. The stiff decrease at λ lower than 400nm (UV) is owing to the scattering property of the particles that has the average length (L) of ~250nm and also to the surface cracks observed in **Figure 3.20** of which the size is in the similar length scale but somewhat larger width scale. Observing many films with different alignment quality, it has been verified that the scattering aspect of the film depends mainly on the size and the amount of these cracks. Therefore an essential condition to improve the optical quality of the film is to minimize these cracks in terms of their number and size. It was shown in the microscopic scale, the same film exhibits large uniform birefringence resulting in the high optical contrast between crossed polarizers (**Figure 3.17.c.A**). A macroscopic view of the whole area of the same film is shown in **Figure 3.22.b**. It is verified from these photographs that the optical quality linked to the degree of the rod alignment is satisfactorily good and uniform on the macroscopic scale for using as a waveplate device even larger than the typical calcite or quartz waveplates made of polished single-crystals.
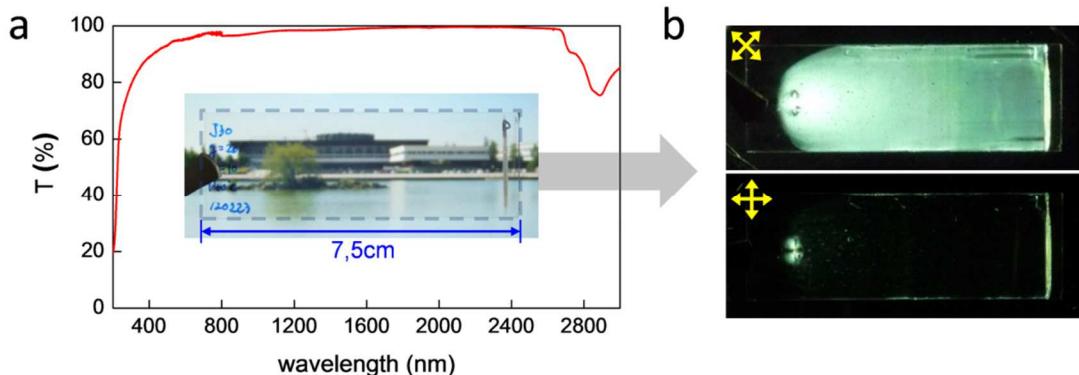
Figure 3.22. (a) Light transmittance spectra of an aligned LaPO$_4$ nanorod film with a thickness of 500nm on the point of measurement. The inset is a photograph taken through a film sample deposited on a glass slide of size 7.5cm × 2.5cm (dashed contour). (b) Photographs of the same sample placed between crossed polarizers with a back light illumination. Rods orientation is horizontal and crossed-polarizer orientation is indicated by the yellow arrows.

Figure 3.23.a shows the intensity ratio (I / I_0) of light transmission measured at different angle between the polarizer and the rod orientation director of the film (θ). The birefringence of the film (Δn) was measured in the same way for the electro-optical measurements noted in the previous section with **Equation 3.2**. Here, the variation of I / I_0 at a fixed wavelength (λ=633nm) as a function of θ fits very well the $\sin^2(2\theta)$ curve of the equation (red line). The

light extinction ratio of I / I_0 was 0.004 at $\theta = 0°$, which confirms the almost perfect orientation of the rods and the superior performance of the film as a waveplate without significant haze. A simple calculation of $\varDelta n$ at $\theta = 45°$ determines a remarkable value of 0.13. It is also verified in Fig.4b that such a large Δn is independent of the different film thickness as, in **Figure 3.23.b**, the retardation (δ) increases linearly with the thickness. Accordingly, any amount of retardation can easily be achieved simply by controlling the film thickness.
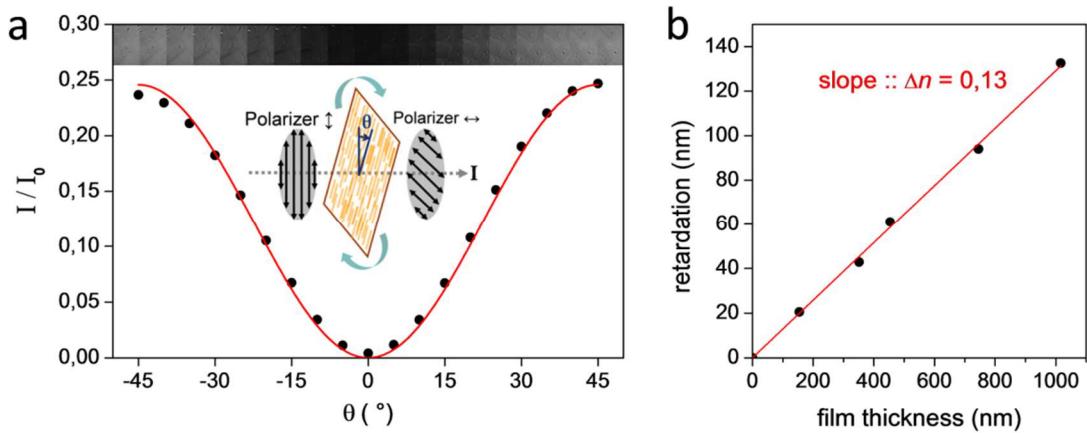
Figure 3.23. (a) Normalized light intensity (λ = 633nm) transmitted through a 750nm-thick film placed between crossed polarizers as a function of the sample azimuth angle θ. The top insets are micrographs taken at each θ. The inset in the middle is a schematic of the measurement configuration. (b) Optical retardation (δ) as a function of the film thickness providing an almost constant value of $\varDelta n$ being 0.13 as the slope of the fitted red line.

Given the high transmittance of the film on a large UV-Vis-IR range (**Figure 3.22.a**), it would be interesting to use this film on the whole range for different applications, which has been impossible with the other thin film waveplates composed of organic polymers. **Figure 3.24** is a spectral data of normalized light transmission intensity (I / I_0)-(top) and the calculated $\varDelta n$-(bottom) plotted on the same axis of wavelength spanning 250 ~ 2000nm obtained on a 400nm-thick film prepared on a quartz substrate. The $\varDelta n$ curves for typical calcite and quartz single crystals are plotted together for a comparison.[94] According to this data, it can be said that a birefringence almost as large as that of calcite (Δn ~ 0.17) with a constancy on the λ range as large as that of quartz (Δn ~ 0.01) can be achieved by the oriented LaPO$_4$ nanorod film. Up to now, one should have carefully chosen among different birefringent materials for waveplates for different uses considering wavelength range, Δn value, surface area, price, etc. Our oriented LaPO$_4$ nanorod films provide a solution to replace those diverse waveplates by only one material, only considering its thickness to obtain the intended retardation. For example, a film sample with a thickness of 800nm (a thickness experimentally achieved as shown in **Figure 3.23.b**) performs as a quarter-wave plate at λ = 520nm (green light) and as a half-wave plate at λ = 280nm (UV).
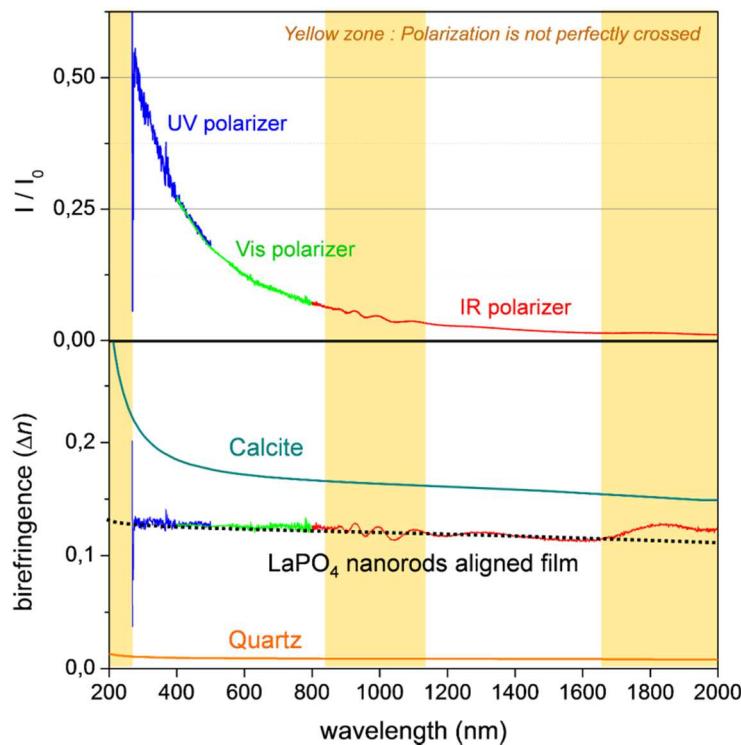
Figure 3.24. Normalized light transmission intensity-(top) and the calculated birefringence-(bottom) according to the wavelength of a 400nm-thick film deposited on a quartz substrate placed between crossed polarizers. For 3 different range of wavelength, UV, Vis, IR, proper polarizers were used. Birefringence data of typical calcite and quartz crystals were added *from the reference paper* [94]. Yellow colored regions where the UV data are not given and the IR data are fluctuating are where polarizers are not working perfectly.

3.2.3. Prospect

A couple of intrinsically birefringent mineral crystals such as calcite and quartz have been the only materials allowing for the control of light polarization for wide spectral range and high power light source. However, the difficulty in processing large single crystals with controlled thickness to obtain a uniform retardation have lead high production costs and size limitations. Stretched organic polymer films based on the photoelastic effect are often substitutes for mineral crystals to make cheap, large area retardation plates. However, their lower optical quality, narrow transmission spectral range, and low thermal stability that are inevitable with organic materials have limited their application only to visible or near-IR range and to low power density.

For this reason, there have been researches since decades to find alternative waveplate materials by using the optical anisotropy of nanostructured materials. Periodic gratings fabricated by lithography techniques[95-97] and epitaxially grown metal oxide nanorods[98-101] have been studied as candidates. However, these materials seem to be still far from the real

application considering their drawbacks, at least one among the limited birefringence, low transparency, limited thickness and surface area, and high cost. More recently, mesoporous silica[102] or silica-titania composite films[103] have been reported providing Δn up to 0.06 associated with high transparency and low cost of sol-gel fabrication. Nevertheless, the issue still remains to obtain a homogeneous alignment of pores on a macroscopic area with a film thickness sufficient to reach a useful amount of optical retardation.

The aligned $LaPO_4$ nanorods thin film fabricated by a simple coating process should be a fascinating alternative overcoming all these limitations to make a thin film waveplate. The remarkable birefringence (Δn = 0.13) associated with the high transparency on the entire UV-Vis-IR range and the high thermal and mechanical stability lead by the use of mineral crystals expands its versatile use in UV optics, high flux display devices (e.g. video projectors) and laser optics as well as in telecommunications using IR bands. Compared to the fabrication process of the other existing technologies, it also has the advantage of the scalable and cost effective processability applicable to large area role-to-role process. Above all these things, the novel concept of self-assembling anisotropic building blocks using thixotropic rod gels would be useful in making organized structures of any other type of nanoparticles with interesting anisotropic shapes and physical properties.

In summary, a simple directed-assembly method to fabricate thin films of oriented nanorods was developed. It is based on the shear-induced orientation of anisotropic objects in liquids which is a ubiquitous natural phenomenon. There have been some typical problems making use of this effect for the assembly of rigid particles such as the orientation relaxation and texturing during and after applying the shear. These problems could be eliminated by the strong thixotropic property of the tuned rod gel phase of the $LaPO_4$ nanorods suspension allowing us to make large homogeneous films incorporating a perfectly oriented (in-plane) rods structure. As-prepared films perform remarkably high birefringence (Δn = 0.13) that is almost constant with the film thickness and with the wavelength of light over the 250 ~ 2000nm range. Such large birefringence associated with the high transparency on the whole UV-Vis-IR range is promising for making cheap inorganic waveplates for a variety of applications.

3.3 Birefringence modeling

In the previous sections (3.1 & 3.2), it has been shown experimentally that oriented $LaPO_4$ nanorods in form of liquid crystalline colloidal suspensions or thin films perform significant optical birefringence. Practical applications in diverse optical devices were envisaged as a large retardation could be obtained maintaining high transparency. Especially, Δn = 0.13 obtained from the rod-aligned film structure is unexpectedly high. Now there arise questions how this system exhibits such a large birefringence, and how to control it so as to design materials for proper applications. Finding apposite answers to these questions would be

fruitful for engineering active Kerr effect devices or thin film waveplates considering the required specific characteristics: the amount of retardation, wavelength, transparency, dimension of the device, etc. Wiener's model[104-105], the dielectric tensor components of a heterogeneous medium containing anisotropic inclusions, provides a simple and robust theoretical description of form birefringence. This model has often been used to analyze birefringence of anisotropic media composed of macromolecules including biological objects such as proteins or DNAs.[105-107] When studying such organic compounds, the intrinsic part of birefringence could have been neglected as its contribution to the total birefringence is relatively lower than the form birefringence part. However, the model is also generalizable to anticipate the total contribution of both the form and intrinsic birefringence parts when the medium contains intrinsically anisotropic inclusions as in case of mineral systems.[18, 108] In this section, the experimental results obtained from $LaPO_4$ nanorods suspensions and films are revisited by introducing Wiener's model, which reveals an optimal combination of form and intrinsic birefringence together in this mineral system. Basing upon the good matching of experimental observations with the theoretical analysis, strategies to design and engineer a new class of inorganic birefringent materials are suggested.

3.3.1. Wiener's model

The model considers the mean dielectric constant, ε, of a heterogeneous material composed of a host medium incorporating sub-wavelength size inclusions with the volume fraction, f (noted as the same with Φ),

$$\varepsilon = \varepsilon_1 + \frac{f(\varepsilon_2 - \varepsilon_1)}{1 + (1-f) \cdot \left\{ (\varepsilon_2 - \varepsilon_1) / \varepsilon_1 \right\} \cdot L}$$

(Equation 3.5)

where ε_2 is the dielectric constant of the inclusion material and L is the depolarizing coefficient determined by the geometry of the inclusion. Birefringent heterogeneous material can be obtained with inclusions exhibiting an anisotropy axis, providing that the particle anisotropy axes are aligned. In this case, the value of the birefringence $\Delta n = n_{//} - n_{\perp} = \sqrt{\varepsilon_{//}} - \sqrt{\varepsilon_{\perp}}$ is obtained from $\varepsilon_{//}$ and $\varepsilon_{\perp}$, the values of the mean dielectric constant in the directions respectively parallel and perpendicular to the inclusion anisotropy axis. For partially oriented particles, averaging over the particle orientation distribution reduces the birefringence. For inclusions exhibiting anisotropic shapes, a form birefringence arises from the anisotropy of the depolarizing coefficient L. Several types of anisotropic inclusion geometry have been shown to produce efficient form birefringence.[108] In this study we consider the usual case of revolution ellipsoids which provides a convenient general description of anisotropic nanoparticles (including rodlike or platelike nanoparticles in the limit of large anisotropies). The values of $L_{//}$ and $L_{\perp}$ can be calculated as a function of

the ellipsoid aspect ratio a/b with a being the particle size along the revolution axis and b the diameter of the particle in the equatorial plane[109-110],

$$L_{//} = \frac{ab^2}{2} \int_0^\infty \frac{ds}{\left(s+a^2\right)^{3/2}\left(s+b^2\right)} \qquad \text{(Equation 3.6a)}$$

$$L_\perp = \frac{ab^2}{2} \int_0^\infty \frac{ds}{\left(s+a^2\right)^{1/2}\left(s+b^2\right)^2} \qquad \text{(Equation 3.6b)}$$

$L_{//}$ and $L_\perp$ verifies the relation $L_{//} + 2L_\perp = 1$. The birefringence, Δn, of the heterogeneous medium is thus determined by the dielectric constant of the host medium, ε_1, and of the inclusion ε_2, by the nanoparticle aspect ratio a/b, and by the volume fraction in nanoparticles f. Note that **Equation 3.5** is known to be a good approximation even for dense assembling of particles, that is over the entire range of volume fraction between 0 and 1.[105]

Form birefringence

In **Figure 3.25.a**, the variation of Δn is plotted as a function of f, for different values of the aspect ratio a/b. It is here assumed, first, that the inclusions are homogeneously dispersed and perfectly oriented and, second, that **Equation 3.5** is valid even in the case of dense particle assemblies.[105, 109] Obviously, for $f = 0$ and $f = 1$, which correspond to the cases of homogeneous media of isotropic dielectric constant ε_1 and ε_2 respectively, the form birefringence vanishes. Between these two limit cases, Δn reaches a maximum absolute value for f slightly larger than 0.5. When the particle aspect ratio moves away from unity, the form birefringence Δn changes and rapidly tends to the birefringence value that would provide particles of infinite aspect ratio so that sufficiently anisotropic nanoparticles are well described by ellipsoid of infinite or zero aspect ratio. In case the particles become prolate ellipsoids, $a/b > 1$, the form birefringence generated should be positive as plotted as black lines. And when the particles become oblate, $a/b < 1$, they show negative form birefringence as grey lines. The infinite case of prolate ellipsoid ($a/b \to \infty$) can be considered as long cylindrical particles and the infinite case of oblate ellipsoid ($a/b \to 0$) can be considered as a stack of thin large plates.

Intrinsic birefringence

Apart from the form birefringence, nanoparticles made out of a material which exhibits, in the bulk state, an optical anisotropy axis provide intrinsic birefringence. Considering a heterogeneous material containing such spherical nanoparticles and assuming perfect alignment of the nanoparticle anisotropy axis, the material birefringence can be obtained from **Equation 3.5** as a function of the volume fraction in nanoparticles. In **Figure 3.25.b**, the variation of Δn versus f are plotted for different values of the intrinsic nanoparticle material birefringence of, $\Delta n_2 = n_{2a} - n_{2b}$, where n_{2a} and n_{2b} are the refractive indices of the nanoparticle material in the directions respectively parallel and perpendicular to the anisotropy axis. The heterogeneous medium birefringence Δn increases monotonously with f and reaches the maximum possible value of Δn_2 for $f = 1$. The nonlinear variation of Δn with f is reinforced by the difference between the refractive index of the particles and the host medium. In the present calculation we have taken $\Delta n_{2b} = 1.654$ and $\Delta n_1 = 1$. For $n_1 \approx n_{2b}$, we would have $\Delta n \approx f \cdot \Delta n_2$.
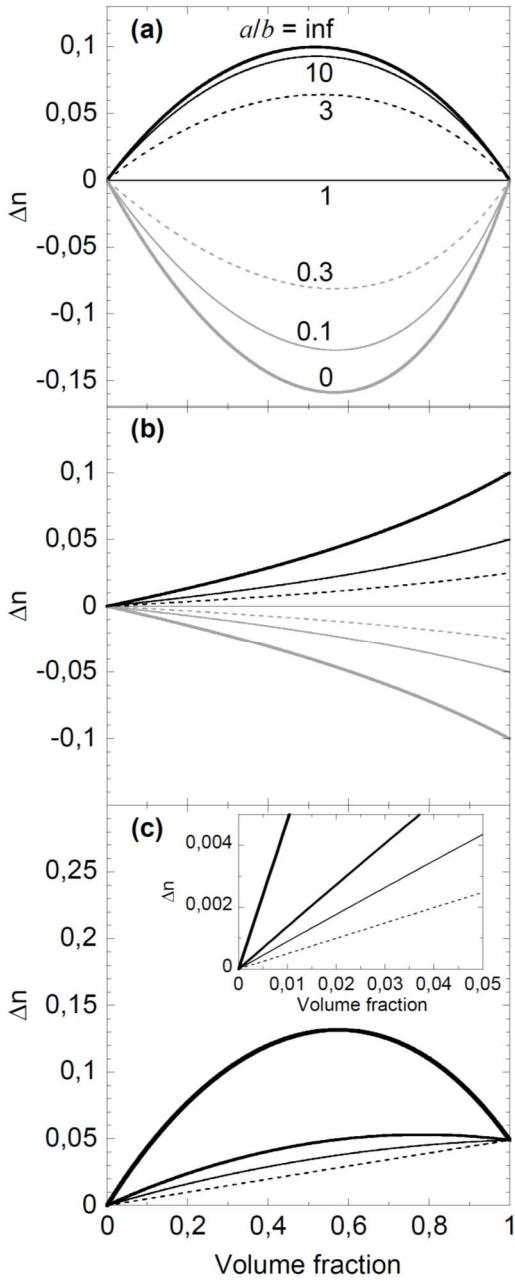
Figure 3.25. Calculated birefringence of the heterogeneous material as a function of the volume fraction of nanoparticle inclusions (**Equation 3.5**). (a) Nanoparticles of refractive index $n_2 = 1.7$ are dispersed in a host medium of refractive index $n_1 = 1$. Form birefringence is calculated for different values of the nanoparticle aspect ratio a/b corresponding to oblate spheroids [grey lines: 0 (bold), 0.1 (full), 0.3 (dashed)] and prolate spheroids [dark lines: 3 (dashed), 10 (full) infinite (bold)]. (b) Intrinsic birefringence is calculated for spheroid nanoparticles exhibiting an intrinsic birefringence $\Delta n_2 = -0.1$, -0.05, -0.025, 0, 0.025, 0.05, 0.1. The average nanoparticle refractive index is $n_2 = 1.68$ and the host medium refractive index is $n_1 = 1$. (c) Prolate nanoparticles of infinite aspect ratio and of refractive index $n_{2a} = 1.703$ and $n_{2b} = 1.654$ are dispersed in a host medium of refractive index $n_1 = 1$ (bold), 1.33 (full), 1.44 (thin), 1.654 (dashed).

Combination of intrinsic and form birefringence

Then, when using nanoparticles made of an intrinsically birefringent material and also exhibiting an anisotropic shape, the intrinsic and form birefringence combine and one could expect to be able to elaborate highly birefringent heterogeneous material. In **Figure 3.25.c**, the birefringence of a heterogeneous material containing nanoparticles of infinite aspect ratio, made of an intrinsically birefringent material, is plotted as a function of the nanoparticle volume fraction. We have chosen the case of a nanoparticle material which is a uniaxial positive birefringent compound with its optical anisotropy axis parallel to the long axis of the nanoparticle, so that form and intrinsic birefringence have the same sign and sum up. In this calculation we have taken $n_{2a} = 1.703$ and $n_{2b} = 1.654$ thus $\Delta n_2 = 0.049$. Different values of the host medium refractive index n_1 have been used: 1 for air, 1.33 for water, and 1.44 for ethylene glycol (EG).

This simple modeling result implies that designing heterogeneous materials carefully considering the refractive indices of the host medium and (optically and geometrically) anisotropic inclusions enables an advantageous combination of both intrinsic and form birefringence. For large refractive index contrast between nanoparticles and host medium, the form birefringence dominates and the overall birefringence takes a maximum value for a volume fraction slightly larger than 0.5. The maximum value of Δn obtained in air medium is 0.132 and it is much higher than the maximum values reached by only form birefringence when $a/b \to \infty$ ($\Delta n_{max} \approx 0.1$, **Figure 3.25.a**) or by only the intrinsic birefringence of the same material ($\Delta n_2 = 0.049$). For small refractive index contrast with the host medium, the optimum birefringence shifts toward higher volume fraction (far from 0.5) because of a weaker contribution of the form birefringence. However, the contribution of the form birefringence remains significant, in particular at low volume fraction. As will be discussed below, each condition has interesting consequence for the case of thin films, nematic colloidal suspensions, and electro-optical applications.

3.3.2. Birefringence of LaPO₄ systems

Indeed, the values of n_{2a} and Δn_2 that have been used for the above calculation of the combination of form and intrinsic birefringence correspond to the refractive indices and the intrinsic birefringence of LaPO₄ crystals in the hexagonal rhabdophane phase. Thus the above calculations can directly be considered as the modeling of the experimental systems such as LaPO₄ rod aligned films, colloidal LC suspensions, and the aligned rods in the electro-optical cells. **Figure 3.26** schematically shows the heterogeneous structure of the LaPO₄ systems where intrinsically birefringent nanorods are dispersed in an isotropic host medium. It has been shown in Chapter 2, the synthesized LaPO₄ nanorods have a long rod-like morphology with an average aspect ratio of $a/b \approx 20$. As **Figure 3.25.a** shows a rapid convergence of the form birefringence when $a/b > 10$, our experimental systems could be

approximated to be the same with a theoretical system containing long cylindrical inclusions $(a/b \rightarrow \infty)$.
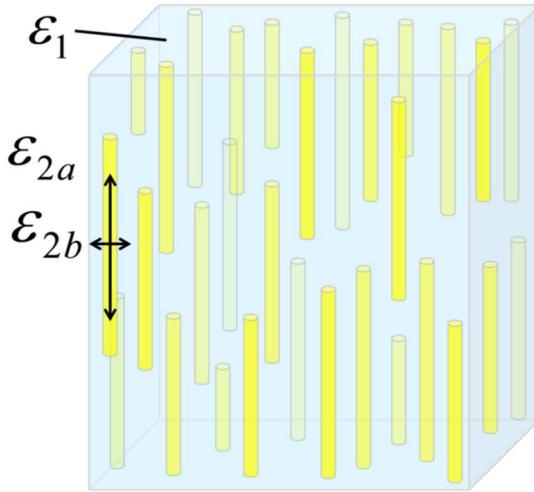
Figure 3.26. Schematic snapshot of the heterogeneous structure composed of a host medium with the dielectric constant, ε_1, and intrinsically birefringent LaPO$_4$ nanorods with non-identical ε_{2a} and ε_{2b}.

Rod aligned films

It has been shown in the previous section that the LaPO$_4$ nanorod aligned film exhibits homogeneous and constant large birefringence. In this film, the rod orientation is almost perfect $(S \approx 1)$ and they are densely packed with a random positional order, of which the packing density (rod volume fraction, Φ) is estimated roughly to comprise between 0.5 ~ 0.7. The remarkable value of the measured birefringence from this film, $\Delta n = 0.13$, is equal to the maximum possible value calculated after **Equation 3.5**. Such a good match indicates that Φ of the film corresponds to that precisely optimizes the optical anisotropy of the heterogeneous material. Taking into account the uncertainty of 0.01 on the measurement of Δn, the volume fraction can be estimated to comprise between 0.5 ~ 0.7 from the diagram in **Figure 3.27** that is redrawn after **Equation 3.5** for the case of LaPO$_4$-air mixture. And it gives the same range of the estimation upon the packing nature of rods. The fact that the measured Δn reaches the calculated theoretical limit also evidences again the particles' perfect alignment in the film. Note that the maximum possible volume fraction for a compact hexagonal assembling of all identical cylindrical rods is ~0.9. For such a highly ordered and compact assembling, Δn drops to a value almost twice smaller than the actual value obtained from randomly packed film. Therefore, it is demonstrated that the heterogeneous structure of LaPO$_4$ nanorod thin films with a perfect orientational order but without a positional order is beneficial to exhibit birefringence corresponding to the optimal combination of intrinsic and form birefringence. The obtained Δn value is about three times larger than the bulk LaPO$_4$ intrinsic

birefringence and about 30% larger than the theoretical limit of form birefringence in the absence of intrinsic birefringence.
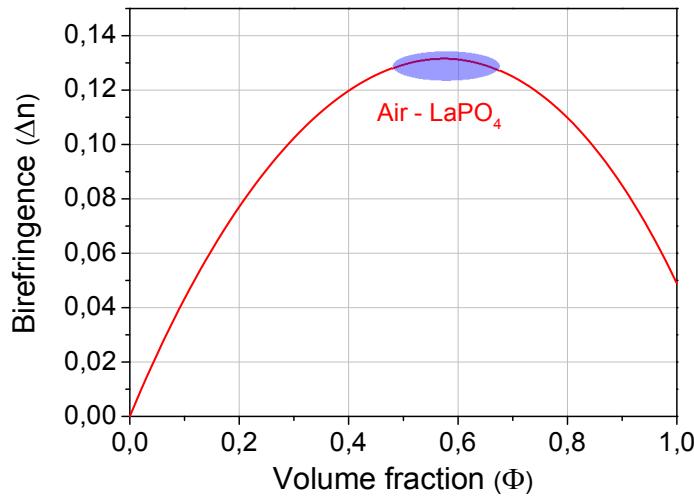
Figure 3.27. Calculated birefringence of the air-LaPO$_4$ nanorods mixture according to the volume fraction (Φ) assuming a perfect orientation and a random distribution of nanorods. The blue region is where the experimentally obtained value of Δn and the expected Φ matches with the calculated result.

Device application of this compact rod aligned film structure for waveplates requires a control of the actual retardation. This can be achieved by controlling either the film thickness or the refractive index contrast between the nanoparticle material and the host medium. The variation of the retardation measured on LaPO$_4$ nanorod films of different thicknesses was plotted in **Figure 3.23.b**. The expected linear variation was observed here. Controlling the material thickness is thus the most straightforward method. But sometimes it might be a difficult task, especially with high values of Δn, if nanometric precision on retardation is required. High reproducibility in the colloidal rod gel synthesis and in the film deposition process is then mandatory. Controlling the value of Δn can be an alternative or even a complementary method which can even be advantageously applied *a posteriori*. Indeed, Δn can be adjusted once the film being deposited by subsequent impregnation to fill up the $(1-f)$ volume fraction of the film porosity with a material of controlled refractive index. As a quick demonstration, a LaPO$_4$ nanorod film was dip-impregnated with ethanol (EtOH) and ethylene glycol (EG). The measured value of $\Delta n = 0.13$ with the pores filled with air (i.e. the host medium is air) dropped down to 0.069 and 0.062 respectively in EtOH and EG. Such an abrupt drop of Δn values indicates that the liquids were absorbed filling the pores (i.e. the host medium was changed by the liquids). These values are slightly higher than the calculated values substituting Δn_a with the refractive index of each medium as alike in **Figure 3.25.c** And it seems to be due to some portion of closed pores that were not filled just by dipping the film in the liquids. Anyway, filling the pores with a medium of a certain

81

refractive index thus allows adjusting the birefringence, and subsequently the retardation through the film. Note that, since Δn is decreased, the film thickness must be increased to obtain a given retardation but the requirements on the film thickness precision is less severe, so that this method may be useful if high precision on the retardation value is necessary. Though here the host medium was exchanged only by absorbing some liquids, it would also be interesting to introduce transparent solid materials such as organic/inorganic polymers since the film deposition process for the fabrication of further engineered optical films. And designing such composite materials will be guided by the above demonstrated Wiener's model by varying the main parameters: refractive indices and volume fractions.

Colloidal suspensions

Provided the possibility of generating significant birefringence by orienting nanorods in the liquid phase utilizing the LC property and the optical Kerr effect (See Chapter 2 and the section 3.1), its theoretical study is also of high interest. Differently to the solid thin films with a high Φ range close to the optimum, liquid suspensions, either isotropic or nematic and columnar sols, can generally be regarded as dilute suspensions of which Φ is less than 10%. Thus in this case it is required to zoom in on this range of the diagram in **Figure 3.25.c**, where Δn would also be relatively low. **Figure 3.28** is thus plotted in a low Φ range (0 ~ 6%) interested for liquid suspensions.
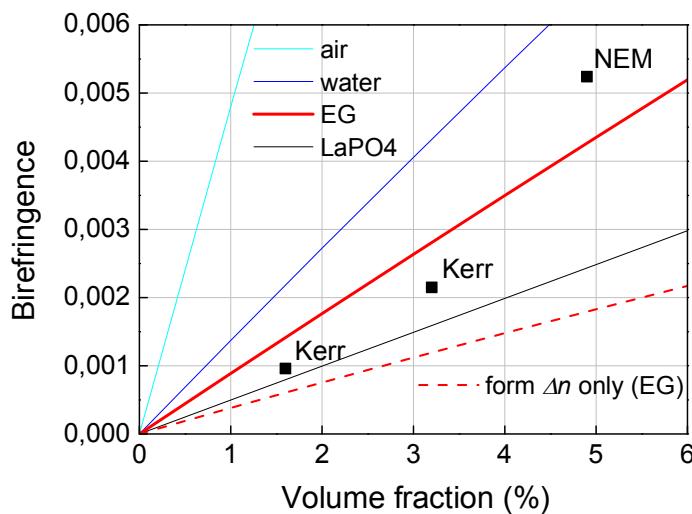
Figure 3.28. Lines are plots of birefringence (Δn) according to the volume fraction (Φ) calculated by Wiener's model for colloidal suspensions of perfectly oriented LaPO$_4$ nanorods in different host media: air, ethylene glycol (EG), water, and a medium with a refractive index the same with LaPO$_4$ crystals. Dotted line is a plot assuming intrinsically non-birefringent inclusions in EG. Black square points are experimentally measured values from a nematic suspension and two isotropic suspensions oriented by electric Kerr effect.

Coming back to the section 3.1.2 (**Figure 3.6.a**), the error from the commercial IPS cell had been recognized by comparing the experimental result with the calculation based on the Wiener's model. Red line in this figure is indeed the same with the red line plot in **Figure 3.28** for EG medium. The experimental value almost 1-order of magnitude higher than the calculation at the same Φ was unacceptable considering the model's reliability in predicting film birefringence. Taking into account that the electrically induced rod orientation is not perfect (S < 1), Δn from the liquid system is expected to be a multiplication of S (order parameter) with the Δn value calculated assuming a perfect rod orientation as they have a direct proportional relation.[74-75] Therefore, the experimental points should normally be placed a little lower than the calculated plot line if the rod orientation by Kerr effect reached close to the saturation.

Considering the correctly measured results using the hand-made IPS cells, the maximum value of Δn plotted in **Figure 3.9** is 0.00215 when Φ = 3.2%. The experimental point is marked again in **Figure 3.28** (in the middle noted as 'Kerr') and it is placed in the theoretically expected region below the red line plotted based on Wiener's model. One more point by Kerr effect experiment at lower Φ is also added in this figure (also noted as 'Kerr') that displays the same tendency.

Another point of measurement with a spontaneously oriented nematic suspension at higher Φ is also added (noted as 'NEM'). Birefringence of this nematic phase was observed on a small single domain region after shear-aligning so that the rod orientational should have been almost perfect (S ≈ 1). The Δn value obtained on this phase is placed about 20% higher than the calculation. This acceptable deviation supposed to be due to some probable reasons such as measurement errors for rod volume fraction, IPS cell thickness, and retardation, and also the possible inaccuracy of Wiener's mode. The question of what would be the main reason is still under debate.

In **Figure 3.28**, the red line is ~75% higher than the black line assuming there is only intrinsic birefringence, and is more than a double than the dashed red line only for form birefrigence. And the three experimental points are placed not far from the red line. This result stands for the fact that combining form and intrinsic birefringence together is even more helpful in this case of dilute colloidal suspensions compared to the case of compact thin films to reach large birefringence over the theoretical limit of using only one part of them. This is interesting as minimizing the thickness of the Kerr cell device is a critical issue. The presence of significant intrinsic birefringence would also enable a zero-scattering device when the refractive indices of the medium and inclusions are matched while form birefringence disappears with the scattering aspect but intrinsic birefringence stays.

In summary, the large birefringence observed from the oriented LaPO$_4$ nanorods both in the liquid suspensions (section 3.1) and the solid thin films (section 3.2) was examined theoretically by using Wiener's model. According to the model calculation, the main parameters determining the birefringence of an anisotropic heterogeneous material are the particle aspect ratio, volume fraction, refractive index contrast between the particles and the host medium, and the intrinsic birefringence of particles. It was found that the optimal combination of the form birefringence – involved with the rod orientation – and the intrinsic birefringence of LaPO$_4$ particles (Δn_{LaPO_4} = 0.05) offers the remarkable total birefringence observed from the thin films (Δn = 0.13). In case of liquid suspensions, the contribution of the intrinsic part becomes more important as the refractive index contrast drops decreasing the form birefringence part. All the experimental results match well with the model calculations. And the model enables the rational design of new birefringent materials with targeted optical properties.

3.4. Conclusion

Organic liquid crystals are convenient active polarization modulators but only useful with low power light sources in the narrow wavelength range. Single crystalline calcite and quartz are commonly used for waveplates performing ideal birefringence and transparency but very costly to make large. We have shown a new approach to resolve these problems yet taking the advantages of the both materials by using mineral liquid crystals and their directed-assembly. Indeed, there exist a number of mineral crystals exhibiting intrinsic birefringence other than calcite or quartz. As the intrinsic optical anisotropy originates from the crystalline structural anisotropy, highly birefringent crystals also have high chance to be synthesized into anisotropically shaped nanoparticles. An organized structure of such optically and geometrically anisotropic nanoparticles can exhibit large total birefringence originated from both intrinsic and form birefringence. The validity of this approach was confirmed by the theoretical analysis using Wiener's model. Concluding remarks from the theory is that the optical properties of a retardation device can be anticipated and designed as targeted by choosing appropriate materials and controlling the main parameters such as porosity. Our LaPO$_4$ system can be said to be a representative engineered material following this concept. The active electro-optical cells by the soft colloidal nanorod suspension perform outstanding Kerr effect despite the weakened refractive index contrast. The thin film waveplates by the compact nanorod assembly challenge the performance of calcite single crystals with incomparably lower cost and easy fabrication process applicable on the large area. In both cases, the large birefringence benefits the synergetic combination of intrinsic and form birefringence together. Now the above-demonstrated device performances accompanied by the high optical contrast are ready for commercialization.

※ Experimental detail ※

Electro-optical measurement

Commercial IPS cells are from Instec Inc (US). These cells are filled with a sample colloidal suspension by the capillary intrusion (~10µL). Handmade IPS cells are made on a 2.5cm × 2.5cm sized glass substrate (1/3 of a typical glass microscope slide). Substrates are coated with a thin gold layer (~100nm) by plasma sputter-coater (Emitech Inc) then the gap was made by scratching with a cutter. Spacers were simply made of scotch tapes (3M) that have a constant thickness d of 60µm. Depositing a tiny volume (~10µL) of a sample suspension on the gap area and then covering the cell with a glass coverslip with a light pressing is enough to make a complete cell as the capillary force maintains the coverslip well attached on the spacer layer. As both commercial and handmade cells have open holes exposed to outside, evaporation of the suspension solvent (EG) occurs slowly, thus the samples were prepared just before the electro-optical measurement each time. Prepared cells are mounted on a lab-made cell support that has the same size of the microscope glass slides for the easy microscopy manipulation and a stable electric contact of the exposed part of the cell electrodes (ITO/gold). Cells on the support are connected with a voltage amplifier (FLC, dual channel broadband linear amplifier 'A400D') which is connected to a low voltage function generator. To avoid the short-circuit problem due to the electrolysis (easily visible by the triggering of bubbling under high electric field strength), high frequency (1kHz < v < 1000kHz) alternative voltage with zero-offset was used for the Kerr effect measurement. Also, switching on/off the main power of the voltage amplifier generates voltage shock that induces instant current through the cell suspension. This was avoided by cutting the electrode contact before turning on/off the amplifier. The measurement of birefringence under applied electric field was conducted in the same way described in Chapter 2.

Blade coating

The home-made blade coating machine is schematized in **Figure 3.15.e**, and it was optimized for the substrate size of standard typical microscope slides (2.5cm × 7.5cm) for the convenience of using commercial glass or quartz slide as coating substrates. ~20µL of phase-tuned nanorod suspension sample is deposited on a substrate. Then the substrate is dragged under the fixed coating blade by a robot arm with the constant speed (~500µm/s) and the gap thickness from the blade plane (20~100µm – varied to control the film thickness). The substrate coated with the sheared suspension coming out of the blade was heated on the heating plate at 140°C to evaporate ethylene glycol. The substrate now with the solidified film was annealed in a furnace at 500°C for 2 hours. Film thickness was measured by using Dektak 150 surface profiler between two grooves made by a cutter.

Suspension phase tuning

To avoid permanent aggregation of the nanorods during tuning the phase to obtain the intended C_{ion} and Φ values, all the samples are started from a stabilized and dilute aqueous phase ($C_{ion} \sim 0.01M$, $\Phi < 1\%$). Rod gel suspensions are prepared directly by transferring and concentrating those aqueous suspensions into EG by a rotary evaporator (See Chapter 2). The final C_{ion} and Φ values could be adjusted by varying the volume of aqueous suspension and the added EG. LC sol suspensions are prepared by decreasing by C_{ion} dialysis. As shown in the phase diagram, the curvature of the decreasing Φ by the intrusion along the dialysis should be considered. Sol samples with lower Φ are prepared by diluting the high Φ suspension in EG.

Chapter 4

Polarized Photoluminescence

In the previous chapters we have focused on the birefringent property of the crystalline $LaPO_4$ nanorods in form of liquid crystalline suspensions and oriented thin films. Now we consider that inorganic systems can incorporate many other anisotropic physical properties according to the variety of mineral compositions synthesizable in form of anisotropic nanoparticles. In fact, crystalline $LaPO_4$ is a rare earth phosphor host that has been widely used for lighting and display devices. When doped with other lanthanide ions such as europium (Eu^{3+}), cerium (Ce^{3+}), or terbium (Tb^{3+}), or their mixtures, crystalline $LaPO_4$ becomes an efficient phosphor emitting red, green, or blue lights under excitation in UV or some specific wavelengths in the visible range. This was indeed another reason for choosing $LaPO_4$ as the base material of this study. It was a vague idea at the beginning, but some kind of anisotropic photoluminescence (PL) control was expectable supposing the first goal of rod orientation control was achieved. Later on, we really found a peculiar anisotropic PL effect from the oriented structures of Eu doped $LaPO_4$ ($LaPO_4$:Eu) nanorods: Each of the many sharp peaks composing the particular europium emission spectra are differently polarized according to the crystallographic axes of the $LaPO_4$ nanorod. It is discussed in this chapter where this polarization comes from and how it is different from the familiar luminescence polarization effect by the other types of phosphors. The detailed aspect of the polarized PL emission is demonstrated experimentally from different types of oriented $LaPO_4$:Eu nanorod samples such as aligned thin films, nematic liquid crystalline suspensions, electrically aligned isotropic phase, as well as from a single nanorod observed by confocal microscopy. Then it is envisaged how this polarization effect can be utilized as an indicator of the orientation states of many interesting systems. A concrete example of application for microfluidics is also suggested in the final section.

4.1. Photoluminescence of lanthanide-doped LaPO$_4$

The typical photoluminescence (PL) emission spectra of lanthanide-doped nanocrystals consist of many sharp peaks for the different transition levels due to the splitting of the 4f configuration of lanthanide ions.[111] Such a distinct PL aspect compared to the broad single emission peaks of other types of phosphors (e.g. organic dies or semiconductor emitters) offers a great possibility of engineering emission color and intensity by varying the doping ions and the host matrix composition. Among the large number of host materials, LaPO$_4$ has been proven to be a desirable host mineral when doped with Eu, or Ce and Tb considering its high quantum efficiency close to a unity and the high thermochemical stability as well as the easy hydrothermal synthesis methods.[51, 56, 59, 112-117] For this reason, doped LaPO$_4$ crystals have been widely used as a commercial red (Eu-doped) and green (Ce,Tb-doped) emitting phosphors.

Figure 4.1. Photograph of aqueous suspensions of luminescent Ce$_{0.45}$Tb$_{0.15}$La$_{0.4}$PO$_4$ (green emission) and Eu$_{0.05}$La$_{0.95}$PO$_4$ (red emission) nanorods under UV lamp irradiation (λ_{exc} = 260nm).

We have tested doping Eu, Ce, and Tb ions into our LaPO$_4$ nanorods simply by mixing the La^{3+} precursor solutions with the Eu^{3+}, Ce^{3+} and Tb^{3+} precursor solutions prior to the nanorod synthesis by precipitation reaction. Their molar ratios were adjusted to the optimized values to get the highest emission quantum efficiency reported in literature (5% for Eu, 45% and 15% for Ce with Tb respectively).[51] When synthesis was continued in the same way described in chapter 2, colloidal suspensions of LaPO$_4$:Eu and LaPO$_4$:Ce,Tb nanorods could be obtained with the same crystallization and dispersion quality for non-doped LaPO$_4$ nanorods. Figure 4.1 shows the as prepared aqueous suspensions (Φ = 0.5%) of doped LaPO$_4$ nanorods under UV excitation (λ_{exc} = 260nm) displaying a significant PL properties of both compositions.
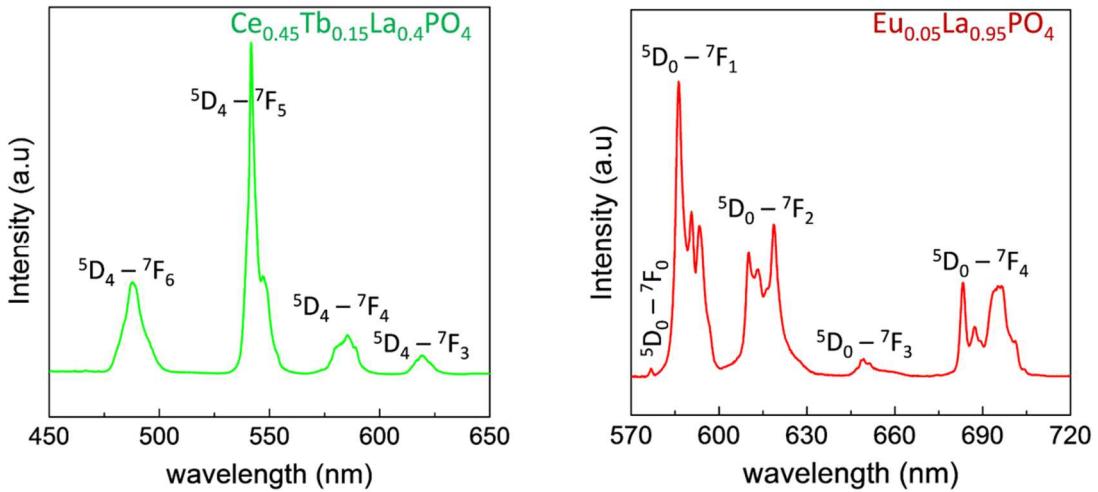
Figure 4.2. Photoluminescence emission spectra from aqueous suspensions of Ce & Tb doped-(left) and Eu doped-(right) LaPO$_4$ nanorods under UV excitation (λ_{exc} = 260nm).
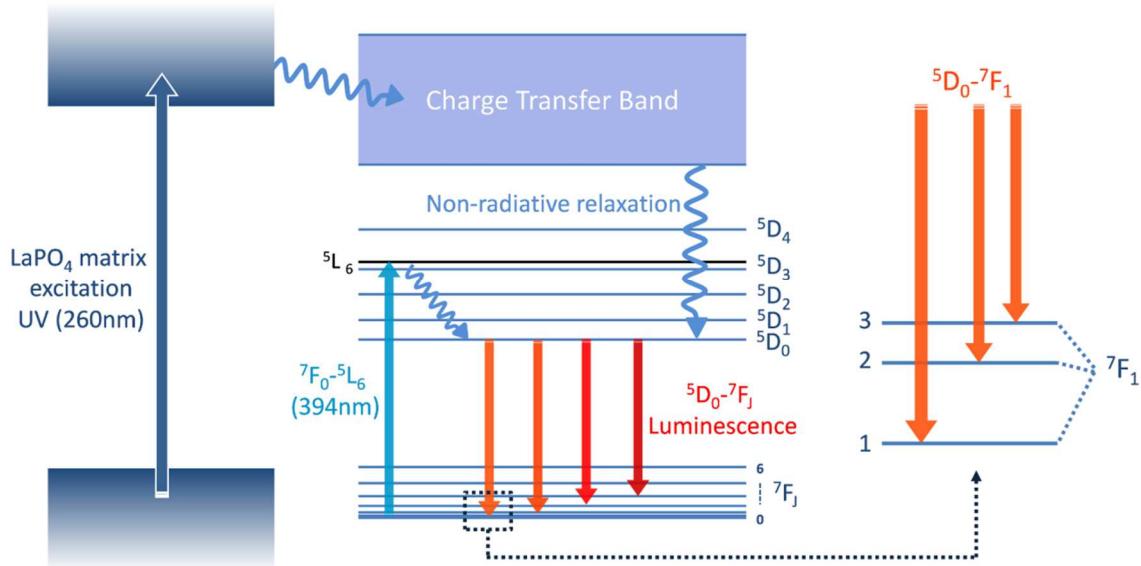
Figure 4.3. Energy level scheme of LaPO$_4$:Eu photoluminescence. The two main excitation pathways through the LaPO$_4$ matrix by UV (260nm) and the direct $^7F_0$-$^5L_6$ excitation by 394nm, and the $^5D_0$-^7F_J emission lines are noted. The right scheme zoomed from the dotted square shows the low symmetry splitting into the three sublevels of $^7F_1$.

The emission spectra of these samples are shown in **Figure 4.2**. As stated above, both the green and the red emission spectra display a series of different transition bands corresponding to the $^5D_4$-^7F_J and $^5D_0$-^7F_J (J = 0,1,2,3,4,5,6) transitions respectively. In case of LaPO$_4$:Ce,Tb, the highest peak ($^5D_4$-$^7F_5$) is placed at λ_{emi} ≈ 540nm leading the green light emission. The emission peaks of LaPO$_4$:Eu are more red-shifted as the first two intense bands

are situated at the orange and red colored light region ($580 < \lambda_{emi} < 630$nm). Figure 4.3 is an energy level scheme of the Eu^{3+} luminescence corresponding to these emission bands. As shown in this figure, UV light excites the $LaPO_4$ matrix ahead and this energy is efficiently transferred toward the charge transfer band (CTB) of the Eu^{3+} ion doped in the matrix. Then the phonon relaxation occurs down to the highly emissive $^5D_0$ level ready to generate luminescence by the radiative $^5D_0$-^7F_J transitions.

What should be noted from the Eu^{3+} emission spectra in **Figure 4.2** is that each transition band shows crystal field splitting into sharp multiple peaks while the Tb^{3+} emission peaks are blunt in the same $LaPO_4$ environment. This can be explained by the non-degeneracy of the $^5D_0$ level of Eu^{3+} ion that involves the simple and easily analyzable stark splitting of each $^5D_0$-^7F_J transitions affected only by the degeneracy of ^7F_J sublevels.[111] The energy scheme at the right side of **Figure 4.3** displays the crystal field splitting of the $^7F_1$ level into three sublevels due to the low site symmetry of the Eu^{3+} ion in the $LaPO_4$ matrix. The synthesized $LaPO_4$ nanorods were found to be in the rhabdophane crystalline phase by XRD in Chapter 2. The doped Eu^{3+} ions belong to the C_2 site symmetry close to the hexagonal symmetry assigned by $P6_222$ space group of the rhabdophane phase.[118-119] According to the selection rules, the low degree of C_2 symmetry accounts for the maximum number ($2J + 1$) of stark splitting thus leading three lines in $^7F_1$ level and five lines in $^7F_2$ level as evidenced by the Eu^{3+} emission spectra in **Figure 4.2**.[120] Focusing on the most clearly visible spectral lines in the $^7F_1$ level, one can see the first degenerate peak is higher than the other two and are not equally spaced. This indicates the Eu^{3+} site is not in a perfectly low symmetry but close to an idealized higher symmetry.[111] Also, there exists at least one small but non-negligible satellite peak next to the third major peak. This supplementary line over the maximum three allowed number of splitting for a unique crystallographic site may belong to the minority site due to the surface effect of nanoparticles.[114, 121-122]

4.2. Polarized photoluminescence of Eu^{3+} doped $LaPO_4$

Uniaxial or lower site symmetry of Eu^{3+} ion gives rise to a unique phenomenon of emission polarization. A transition to an unfolded sublevel is allowed only in a certain direction and forbidden in other directions.[120] Thus each sublevel line has a particular polarization component distinct to the other sublevels' the set of which provides a unique crystallographic fingerprint. Accordingly, the shape of the emission spectra displays a significant change in different polarization axis. This phenomenon should be distinguished from the polarized luminescence of other types of phosphor materials showing an equivalent variation of the whole emission band intensity without change of the spectral form. Observing the peculiar aspect of Eu^{3+} emission polarization together with counting the number of stark splitting for different transition levels has been useful to analyze the symmetry group of various crystalline host matrix (or ligand) materials.[111, 120, 123-124]

In spite of such an interesting polarization effect of rare-earth luminescence, there exist very few reports on its direct observation. This is indeed because of the difficulty to obtain single crystal samples. Rare-earth phosphors are usually synthesized in the bulk form of powders

or colloidal dispersions composed of a lot of nano- or micro-sized monocrystals that are randomly oriented. The observed emissions from these samples are thus isotropic even though each crystalline particle exhibits polarized emission property. A principal way to observe polarized emission is thus to use a single crystal grown up to a macroscopic size large enough to get measureable signals. Brecher *et al.* thoroughly studied in 1960s the polarized Eu^{3+} absorption and emission spectra from a carefully grown yttrium vanadate (YVO_4) single crystal assigning the polarization components of the whole transition sublevels.[123] However, such an arduous work was not continued for many other different host crystals presumably because there was no technical interest if the polarization could not be manifested and controlled in the common random bulk states. Another intelligent way to observe polarized emission would be to make an assembled structure of crystalline particles for their crystallographic axis to be oriented. This approach was attempted decades later by Binnemans *et al.* making Eu^{3+} complex with liquid crystalline mesogenic ligands.[125-127] This novel work revealed the ligand-field split polarized emission spectra from a bulk aligned liquid crystalline phase that is switchable under external electric or magnetic fields.

In our study, we make an assembly of $LaPO_4$:Eu nanorods by using the methods demonstrated in the previous chapters: shear-directed assembly and liquid crystalline (LC) assembly assisted by electric field. Then the polarized emission spectra were observed from these samples where nanorods are oriented parallel.

4.2.1. Polarized emission from rod aligned films (S ≈ 1)

It was demonstrated in chapter 3 that a highly oriented $LaPO_4$ nanorod film could be fabricated by the shear-directed assembly method. The same type of the film was also made with Eu doped $LaPO_4$ nanorods. As the nanorod synthesis and the film fabrication process are identical for undoped nanorods, the film quality and the degree of orientation is the same thus reaching the value of the order parameter close to a unity (S ≈ 1). The crystallographic *c* axes of all the nanorods in this film are thus almost perfectly oriented toward the same direction. Due to the uniaxial rhabdophane phase of $LaPO_4$ nanorods, this film would exhibit a polarized emission property identical to that of a single crystal regardless of the orientation of *a* and *b* axes.

Polarized PL measurement was conducted also using the polarization optical microscope connected with an optical fiber to a liquid nitrogen-cooled spectrometer (SpectraPro-300i, ARC). A simplified scheme is shown in **Figure 4.4.a** and the detailed setup is shown in **Appendix 1**. In standard microscope equipments UV light cannot be used for the excitation of the charge transfer band (CTB) because the optical components such as objective lens are not transparent for UV. Instead, the $^7F_0$-$^5L_6$ transition was targeted as the appropriate excitation band considering its position at the violet edge of the visible wavelength range and its high absorption cross section. The excitation spectra obtained for the highest emission peak at 587nm is shown in **Figure 4.4.b** with a narrow but intense peak at 394nm for $^7F_0$-$^5L_6$ line. The selected excitation light source was an InGaN LED emitting a peak wavelength of 395nm with a narrow half width ($\Delta\lambda$ = 14nm) and an optical output power of 100mW

(SMB1W-395, Roithner Laser Technik) was selected. The light blue-colored region in **Figure 4.4.b** indicates the emission wavelength range of this LED covering well the $^7F_0$-$^5L_6$ line. Such a good match of the $^7F_0$-$^5L_6$ line with the LED light focused on the measurement spot by the microscope objective enabled to acquire an intense emission spectra without using a laser excitation source. The doping ratio of Eu was fixed at 20% ($Eu_{0.2}La_{0.8}PO_4$) for all polarized PL experiments as this ratio was reported to be optimal to get highest emission intensity with 394nm excitation.[128]
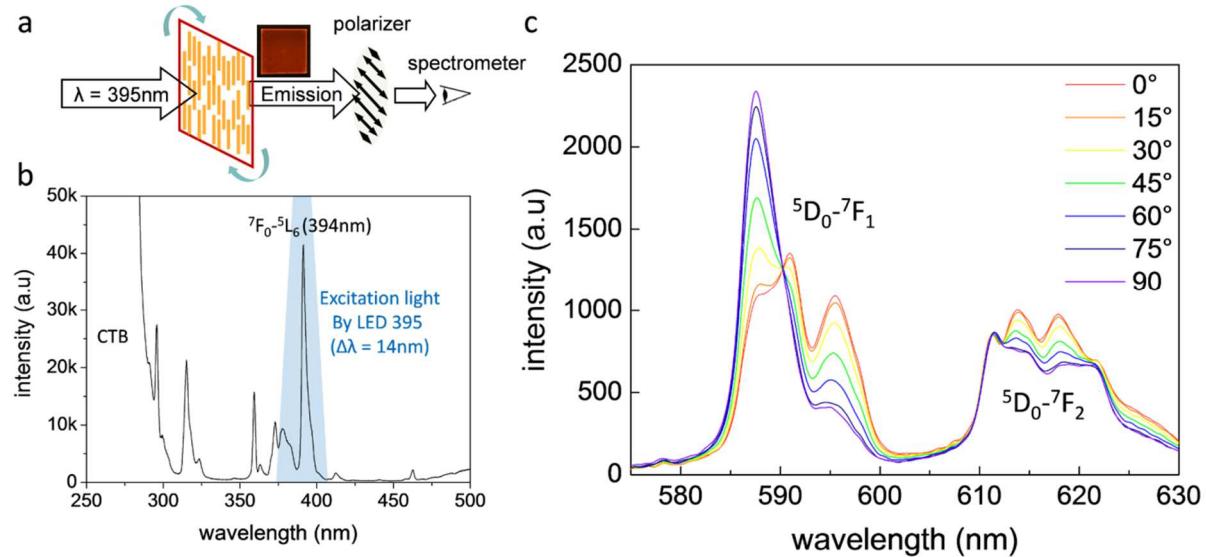
Figure 4.4. (a) Simplified scheme of the measurement of polarized PL emission from a LaPO$_4$:Eu nanorod aligned film. The sample is rotated with a fixed polarizer due to the anisotropy of the spectrometer gratings. (b) The excitation spectra of LaPO$_4$:Eu nanorods obtained on the highest emission peak at 587.5nm. (c) Polarized PL emission spectra (smoothed by FFT filter with 8 points of window) on the two transition levels ($^5D_0$-$^7F_1$ and $^5D_0$-$^7F_2$) obtained at different angle (15° steps) between the rod orientation direction and the polarizer.

The polarized PL emission spectra from the film on the wavelength range corresponding to both $^5D_0$-$^7F_1$ and $^5D_0$-$^7F_2$ levels are shown in **Figure 4.4.c**. The basic spectral form is similar to that shown in **Figure 4.2**, but it changes dramatically according to the angle between the rod orientation direction and the polarizer. The spectra obtained at larger angles ($\theta > 90°$) were symmetric to the observation between 0 ~ 90° supporting the uniaxial crystallinity of the nanorods. As stated above, this spectral change indicates that different sublevel lines have different polarization component, i.e. each degenerate transition dipole has a unique angle to the rod axis (c axis). Considering $S \approx 1$ for the rod orientation, the spectra obtained at 0° and 90° can be regarded to be the π and σ spectra respectively of the Eu^{3+} emission in the rhabdophane LaPO$_4$ host crystal. And the spectra obtained at the intermediate angles between 0° and 90° are the sum of the projections of these π and σ spectra on each angle. It should be noted that these polarized emission spectra were obtained with the isotropic

excitation light. There was no spectral change when the excitation lights with different polarization angles were tested. Therefore, the emission polarization by crystal field splitting is independent of the excitation polarization when the excitation occurs at higher transition level ($^5L_6$) followed by the non-radiative relaxation down to a lower emissive level ($^5D_0$). This becomes an important advantage

Spectral decomposition of sublevels

Focusing on the $^5D_0$-$^7F_1$ transition level, there exist three main peaks at 587.5nm, 590.7nm, and 595.1nm that correspond to the three degenerate sublevels assigned as 1, 2, 3 in the right side energy scheme in **Figure 4.3**. As these peaks are close to each other and superposed, it is required to decompose individual peaks by spectral fitting. OPUS software was used for the fitting and the parameters such as form and width of the peak were found empirically and then kept the same for all peaks. The peak form was not purely Lorentzian but best matched with the 40%-Lorentzian and 60%-Gaussian mixed form. The non-single wavelength LED light (See **Figure 4.4.b**) covering not only the narrow peak of $^7F_0$-$^5L_6$ level seems to be responsible for this Gaussian broadening of the peaks. The observed fact that the peak form becomes almost purely Lorentzian under single wavelength laser excitation at 394nm support this idea. The data fitted in this way for σ and π spectra are shown in **Figure 4.5.a-b**. There are three main peaks and also a satellite peak near the third peak at 597.4nm that was essential for the good fitting result. It is clearly seen here the intensity of these four peaks vary in different way indicating again the low symmetry of the nanorod crystals. **Figure 4.5.c** is a polar diagram of the varied intensity of these peaks fitted on all the spectra taken for each 15° steps shown in **Figure 4.5.c**. These discrete point data are fitted for the orthogonal dipolar components as,

$$I = A \cdot sin^2\theta + B \cdot cos^2\theta \qquad \text{(Equation 4.1)}$$

where I is the measured peak intensity and θ is the angle between the rod orientation and the polarizer. The very good agreement between the fit and experimental data confirms the reliability of the spectral decomposition fitting of the emission spectra. These polar diagrams are redrawn separately for each peak in **Figure 4.6**, together with the orthogonal dipolar components plotted as red lines. This result enables to estimate the angle of each sublevel transition dipole inside the uniaxial crystalline rod. One thing to beware of is that $^5D_0$-$^7F_1$ is a magnetic dipolar transition level where the luminescence emission is polarized orthogonal to the magnetic dipolar axis. The calculated values of A, B and their standard errors, and the angle between the dipole and rod axis (φ) for each peak are noted in **Table 4.1**. The low relative uncertainty on the determination of A and B support the polarized spectra fitting procedure. The angles for each peak gives an idea of dipolar geometry resulted from the crystal field splitting of sublevels. The very similar φ values for the third peak (595.1nm) and

the satellite peak (597.4nm), also visualized in **Figure 4.6.c-d**, indicates that they originate from the same sublevel.
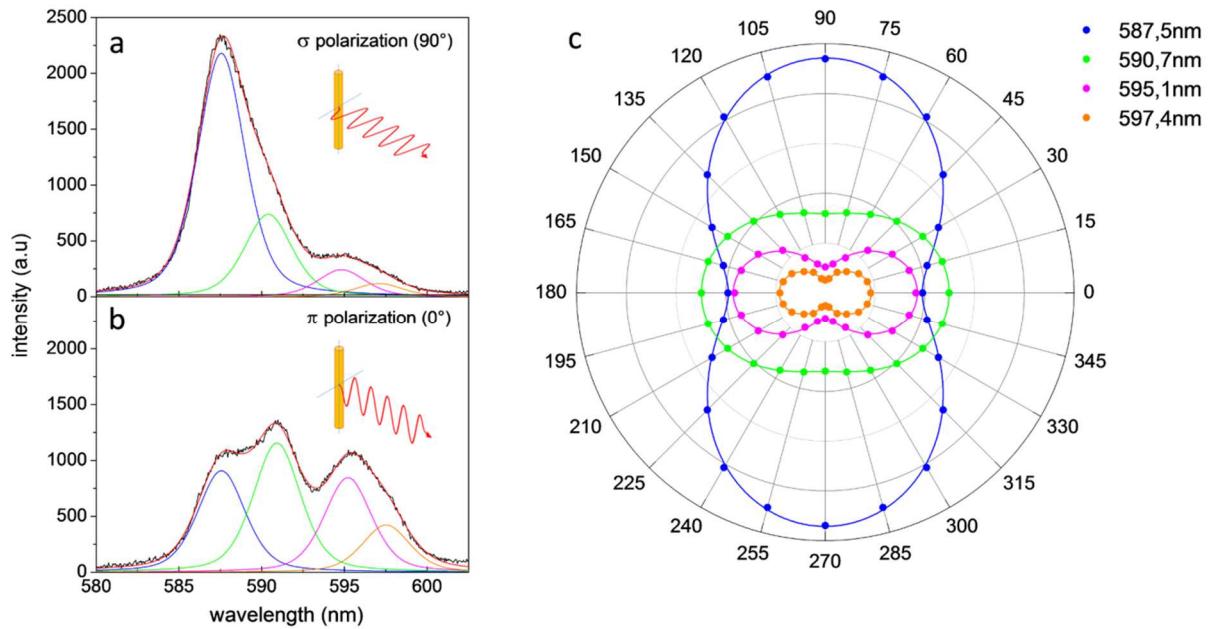
Figure 4.5. σ-(a) and π-(b) polarized spectra on the ${}^5D_0$-${}^7F_1$ level with the fitted spectra (red line) as the sum of four three decomposed peaks for each sublevel transition and one satellite peak. (c) Polar diagram of the intensity of the four peaks fitted on each spectra for different measurement angles (θ) shown in Figure 4.4.c. The continuous line is a dipolar fitting according to **Equation 4.1**.
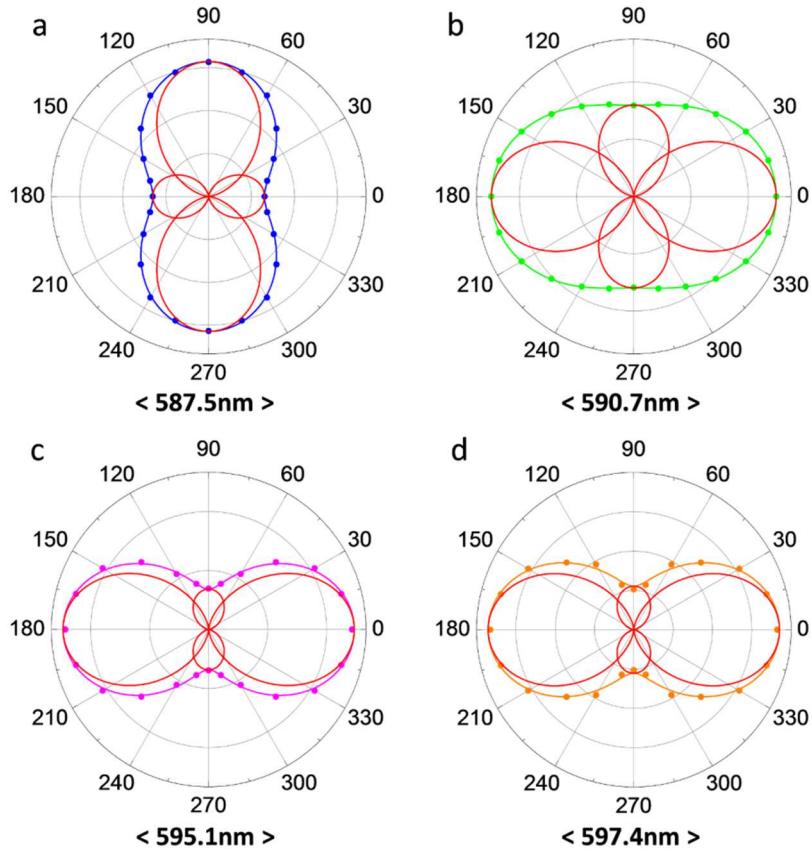
Figure 4.6. Polar diagrams of the peak intensity corresponding to the data shown in **Figure 4.5**.c. Red lines are orthogonal dipolar components decomposed from the fitting line.

peak	587.5nm	590.7nm	595.1nm	597.4nm
A	9422	3191	1025	553
S.E	21.8	4.4	19.3	15.4
B	3899	4979	3700	1852
S.E	20.7	4.2	18.3	14.6
φ	67.5	32.7	15.5	16.6

Table 4.1. Orthogonal dipolar components intensities (*A, B*) calculated by polar fitting and their standard errors (S.E) and the angles (*φ*) between each dipole axis and the rod axis (crystallographic *c* axis).

4.2.2. Polarized emission from nematic suspensions (S ≈ 1)

The σ and π polarized spectra obtained from the rod aligned film are those propagating perpendicular to the rod axis (normal to the plane of rod aligned film). Another essential

polarized emission component missing here is α spectra that propagates along the rod axis, which cannot be measured from the film with the in-plane rod orientation. Nematic liquid crystalline (LC) suspension of the LaPO$_4$:Eu nanorods provides a chance to observe α spectra together with σ and π spectra by controlling their orientation direction under external electric field. The in-plane orientation of nematic phase using IPS (in-plane switching) electrode geometry was described in detail in Chapter 3, from which σ and π spectra can be obtained in the same way from the rod aligned film. Another possible electrical switching mode is homeotropic alignment by using two transparent plane electrodes superposed with a spacer layer. **Figure 4.7.a** shows this geometry of a commercial homeotropic cell (Instec Inc) we used. If an electric field is applied between these two electrods, the nanorods would be oriented normal to the electrode planes.
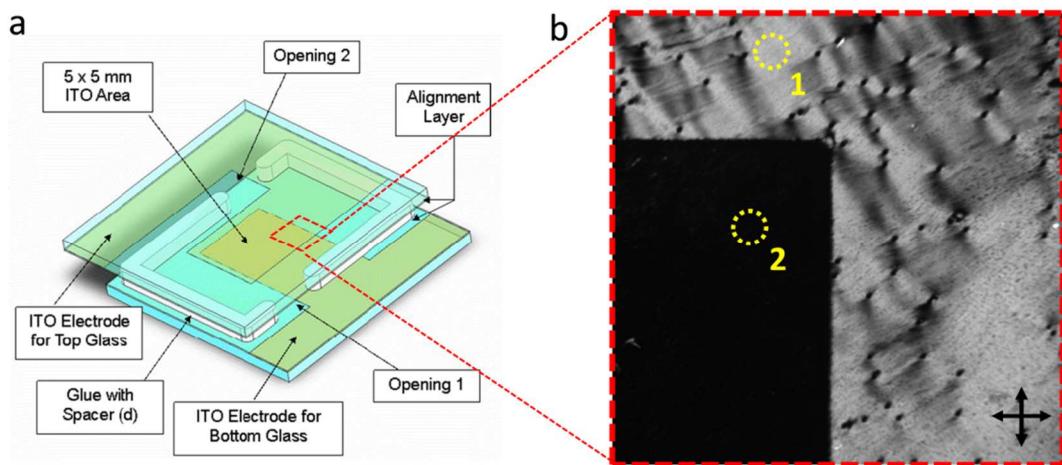
Figure 4.7. (a) Schematic of the commercial homeotropic switching cell (Instec Inc) geometry. *Figure taken from the product brochure* (b) Polarization optical micrograph of a homeotropic cell filled with a dense nematic LaPO$_4$:Eu nanorod suspension with an applied electric field of 1V/µm. The dark region is where nanorods are aligned normal to the two superposed ITO electrodes and the bright region is out of the electrode region where nanorods are aligned in-plane due to the strong shear during filling the cell gap by capillary flow. The σ and π spectra were obtained on the circular region #1 and the α spectra were obtained on the region #2. Size of the picture is 1.8 × 1.8 mm and the black spots dispersed in the bright region are the gap spacer beads.

The birefringent texture of a dense nematic LaPO$_4$:Eu nanorod suspension in this homeotropic cell is shown in **Figure 4.7.b**. The suspension was injected into the cell with a thin gap of 20µm by a spontaneous capillary flow which generates a large shear so that the nematic phase orient towards the flow direction with a very high orientational order close to unity (S ≈ 1) as in the case of the film coating process demonstrated in Chapter 3. Thus an in-plane orientation for measuring σ and π spectra was obtained without an additional effort and was maintained constant long time in a small region of measurement (yellow dotted circle #1) due to the large shear between the tiny gap distance. When the electric field was

applied, the nanorods become re-oriented normal to the two parallel electrode surfaces extinguishing all the in-plane birefringence as the nanorods are uniaxial (dark region). The optical contrast higher than 0.95 between the bright and dark regions indicates the efficient orientation of nanorods into the homeotropic state where the α spectra of the PL emission could be obtained (yellow dotted circle #2).
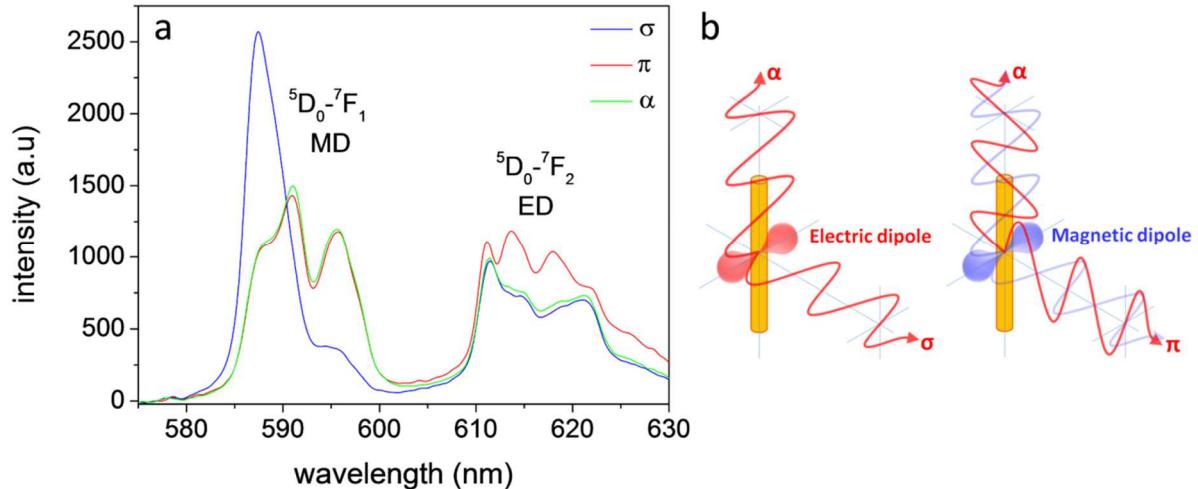
Figure 4.8. (a) σ, π, and α polarized PL emission spectra obtained from a nematic suspension of LaPO$_4$:Eu nanorods in the homeotropic switching cell shown in Figure 4.7. The σ and π spectra were obtained from a shear-aligned (in-plane) nematic phase on the region #1, and the α spectra were obtained from a homeotropic phase under electric field on the region #2. (b) Schematic picture of π and α polarized emission and σ and α polarized emission respectively from magnetic and electric dipoles lying in the plane perpendicular to the rod axis.

Figure 4.8.a shows the three different (σ-blue, π-red, α-green) polarized emission spectra obtained in this way. As expected, the σ and π spectra have the same spectral forms with those obtained from the rod aligned film (**Figure 4.4.c** and **Figure 4.5.a-b**) on both $^5D_0$-$^7F_1$ and $^5D_0$-$^7F_2$ transition bands. Interestingly, the new α spectra displays the same spectral form with the π spectra on the $^5D_0$-$^7F_1$ band and with the σ spectra on the $^5D_0$-$^7F_2$ band respectively. This is indeed because $^5D_0$-$^7F_1$ band corresponds to the magnetic dipolar transition (MD) and $^5D_0$-$^7F_2$ band does to the electric dipolar transition (ED).[111, 120, 123] The α emission is contributed only by the propagation from the dipolar component lying on the plane perpendicular to the rod axis (crystallographic c-axis). As schematized in **Figure 4.8.b**, the α emission of ED is the same as the σ emission in the direction orthogonal to the rod axis, while for the MD it is π-polarized. Note that the observed α emission signal is unpolarized due to the uniaxial crystalline symmetry of the LaPO$_4$ nanorods. Such dramatically different emission spectral forms for each polarization component on the multiple transition bands (ED & MD) contain the information about both the rod orientation direction and the order

parameter in three-dimensional space. The overall theoretical and experimental analysis on it is followed in the next section.

4.3. Orientation measurement by polarized photoluminescence

It was shown in the previous section that $LaPO_4$:Eu nanorods emit polarized photoluminescence (PL) spectra of which shape depends on the direction of observation with respect to the geometrical rod axis (σ, π, and α spectra). This means conversely the polarized emission signals detected from a certain propagation direction contains the information about the relative rod orientation angle. Therefore one can expect that polarized PL analysis of $LaPO_4$:Eu nanorod could be a useful tool for measuring the orientation of the rod itself or of a substance containing it. Indeed, polarization of PL or EL (electroluminescence) is a common effect that is observed from most types of phosphors such as organic dyes[129-133] or semiconductor emitters[35, 134-140], so that this general idea has been exploited since decades especially for studying liquid crystalline (LC) organizations.[130, 141-146] However, there are obvious limits in the traditional method that lag its use for the precise orientation analysis for various anisotropic material systems. These limits come from the intrinsic characteristics of the polarized emission phenomena by those non-rare-earth phosphors. As stated in the previous section, the emission spectra of organic dyes or semiconductors generally have one broad peak of which the total intensity varies according to both the excitation and emission polarization angles.[129-139] The orientation analysis using this polarization nature is basically limited only in 2D space (in-plane orientation) unless a complex optical field geometry or variable incident angle measurement are used.[147] Also, this total intensity can be easily altered by many other experimental parameters such as the emitter density, unstable excitation light, or any reasons that may modify the final signal intensity that are hardly maintained constant during the measurement. Furthermore, manipulating two polarizers for excitation and emission causes many troubles linked to the other optical components of the instrument such as mirrors, filters, and gratings that are polarization selective.

A breakthrough for the first problem (limitation in 2D space) was achieved by utilizing non-linear luminescence effect: second harmonic generation (SHG) and two-photon excited fluorescence (TPEF) together.[147] The complementary polarization responses of SHG and TPEF, that could be recorded simultaneously and separately, enabled the determination of 3D orientation of molecular nanocrystals. And many useful orientation analysis of biological substances – proteins, DNAs, and tissues – were developed based on this method in recent years.[148-150] Whereas SHG and TPF study requires heavy experimental set-up essentially with a high-power laser excitation source and there still remain the other inconvenience stated above.

The crystal-field-split polarized PL emission of Eu^{3+} doped in $LaPO_4$ nanorods demonstrated in the previous section seems to have some crucial advantages to make the orientation measurement more simple and precise. There exist separated ED and MD transition bands, each exhibiting several contributions with specific polarization degree and orientation. These unique features of rare-earth emission allow the 3D orientation analysis simply by

comparing the relative intensity variation of sublevel peaks blowing out the uncertainties when observing the total intensity of the spectra even possible without using a polarizer. The photoluminescence spectrum analysis procedure for the determination of the rod orientation is detailed here below.

4.3.1. Theoretical analysis: "How to determine the orientation"

As demonstrated in the section 4.2.1, each sublevel transition dipole with a particular angle (φ) can be decomposed to two orthogonal components parallel and perpendicular to the rod axis. And due to the uniaxial crystalline symmetry of the rod, the perpendicular component can be considered as a donut-like form or two orthogonal components with the identical intensity for convenience (along the x and y axis on the plane perpendicular to the rod axis). In the case of the electric dipolar transition (ED), the emission intensity by the dipolar component parallel to the rod axis can be noted as $\mathbf{I_\pi}$, and the perpendicular component to be $\mathbf{I_\sigma}$ which is the same with $\mathbf{I_\alpha}$. In case of magnetic dipolar transition (MD), the parallel component provides $\mathbf{I_\sigma}$ and $\mathbf{I_\pi}$ and $\mathbf{I_\alpha}$ are given by the perpendicular component. Therefore the total emission intensity towards three orthogonal directions can be expressed as,

$$\sum I_{ED} = 2I_\pi + 2I_\sigma + 2I_\alpha = 2I_\pi + 4I_\sigma \tag{4.2}$$

$$\sum I_{MD} = 2I_\pi + 2I_\sigma + 2I_\alpha = 4I_\pi + 2I_\sigma \tag{4.3}$$

Single nanorod

Let us consider a single nanorod with a given orientation angles (θ, φ) with respect to the laboratory frame, as schematized in **Figure 4.9**. One can determine the polarized emission intensities propagating along each principal axes x and z ($\mathbf{I_{xy}}$, $\mathbf{I_{xz}}$, $\mathbf{I_{zx}}$, $\mathbf{I_{zy}}$: the first and second indices indicate the propagation direction and the polarization axis respectively) using the nanorod's own polarization components ($\mathbf{I_\pi}$, $\mathbf{I_\sigma}$). These values for ED are,
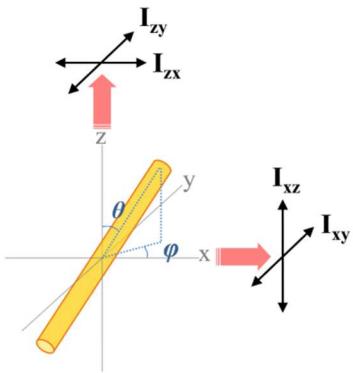
Figure 4.9. Nanorod in 3D space

$$I_{xz} = I_\pi \cos^2 \theta + I_\sigma \sin^2 \theta \tag{4.4}$$

$$I_{xy} = I_\pi \sin^2 \theta \cdot \sin^2 \varphi + I_\sigma (\cos^2 \theta \cdot \sin^2 \varphi + \cos^2 \varphi) \tag{4.5}$$

$$I_{zx} = I_\pi \sin^2 \theta \cdot \cos^2 \varphi + I_\sigma (\cos^2 \theta \cdot \cos^2 \varphi + \sin^2 \varphi) \tag{4.6}$$

$$I_{zy} = I_{xy} \tag{4.7}$$

The I_{xy} and I_{zy} are identical since I_σ and I_a are so for ED. The two components propagating along the y axis (I_{yx}, I_{yz}) can be omitted as they are symmetric with those along the x axis. Considering the measurement in the z-direction of observation, the sum of two polarization components I_{zx} and I_{zy} becomes simply:

$$I_{zx} + I_{zy} = I_z = I_\pi(1 - \cos^2\theta) + I_\sigma(1 + \cos^2\theta) \tag{4.8}$$

As described in the previous sections, Eu³⁺ emission spectra contain multiple peaks that are differently polarized, to all of which the above equations can be applied. Thus if any two distinct peaks or wavelength ranges (indexed with an integer n = 1, 2,…) are chosen in the same transition band, simultaneous equations can be derived with the different intensity values ($I_{n\pi}$, $I_{n\sigma}$) already known from the reference σ and π spectra as,

$$I_{1z} = I_{1\pi}(1 - \cos^2\theta) + I_{1\sigma}(1 + \cos^2\theta) \tag{4.9}$$

$$I_{2z} = I_{2\pi}(1 - \cos^2\theta) + I_{2\sigma}(1 + \cos^2\theta) \tag{4.10}$$

Thus the value of $\cos^2\theta$ can be calculated simply by the ratio $\mathbf{k = I_{1z}/I_{2z}}$ obtained from the measured spectra as,

$$\cos^2\theta = \frac{k(I_{2\pi} + I_{2\sigma}) - (I_{1\pi} + I_{1\sigma})}{k(I_{2\pi} - I_{2\sigma}) - (I_{1\pi} - I_{1\sigma})} \tag{4.11}$$

Once the value of $\cos^2\theta$ is obtained, the $\cos^2\varphi$ value can also be calculated by **Equation 4.5** or **4.6**. It is therefore verified that measuring the emission spectra with two orthogonal analyzing angles in a single measurement plane provides information about the three-dimensional orientation of a nanorod. By the way, from the calculated values of $\cos^2\theta$ and $\cos^2\varphi$, we obtain four symmetric angular positions for each θ and φ. As the nanorod has no sign for front and rear, there exist 4 different combinations of these angles that are mirror images by xy-plane (for θ) and xz-plane (for φ) of one true combination. Measuring one more polarized spectra at an angle between x- and y-axis (45° for example) enables to exclude two mirror images for φ. To distinguish the actual θ from its symmetric position requires one more spectra measurement with a different direction of observation. This is technically possible when using a microscope with a large enough objective aperture. A small aperture positioned at the center of the image plane give the first set of measurements in the direction

normal to the plane of observation. Then, moving the aperture at another position in the image plane enables the measurement of the emission spectra in another direction of observation. In many cases, however, these supplementary measurements would not be necessary because experimental conditions may give enough information to eliminate the mirror images.

For MD, the above equations for ED remain almost the same and just the indices positions are exchanged due to the orthogonal relation between MD and ED. Thus for MD,

$$I_{xy} = I_\sigma \cos^2 \theta + I_\pi \sin^2 \theta \tag{4.12}$$

$$I_{xz} = I_{zx} = I_\sigma \sin^2 \theta \cdot \sin^2 \varphi + I_\pi (\cos^2 \theta \cdot \sin^2 \varphi + \cos^2 \varphi) \tag{4.13}$$

$$I_{zy} = I_\sigma \sin^2 \theta \cdot \cos^2 \varphi + I_\pi (\cos^2 \theta \cdot \cos^2 \varphi + \sin^2 \varphi) \tag{4.14}$$

$$I_{zx} + I_{zy} = I_z = I_\sigma (1 - \cos^2 \theta) + I_\pi (1 + \cos^2 \theta) \tag{4.15}$$

$$\cos^2 \theta = \frac{k(I_{2\sigma} + I_{2\pi}) - (I_{1\sigma} + I_{1\pi})}{k(I_{2\sigma} - I_{2\pi}) - (I_{1\sigma} - I_{1\pi})} \tag{4.16}$$

Therefore, both ED and MD transition level spectra can be used in the same way to detect the orientation of a single nanorod.

Partially oriented rod suspension (0 < S < 1) with a known director ($\vec{n}$)

Considering bulk samples containing many nanorods such as colloidal suspensions, the orientation state consists of two main parameters: orientational order parameter (S) and its director ($\vec{n}$). In this case, the observed emission spectra from the region of measurement at any polarization angle would be an averaged sum of the emission from all the nanorods inside the region that have a certain distribution of θ and φ according to $\vec{n}$. When the nanorods are oriented under external electric or flow fields, or assisted by the spontaneous LC organization, a frequent and interesting question is how to measure S varying with the controlled field strengths. Such as for a single nanorod, polarized emission analysis provides a solution to obtain the value of S that spans from zero to a unity ($0 \leq S \leq 1$). In most cases, the director of orientation $\vec{n}$ is along the external field which is a controlled variable. Thus the polarized PL emission measurement can be conducted in the direction of observation parallel or orthogonal to the director axis, by which the calculation becomes simple.

Figure 4.9 can be again used as schematics for the bulk sample measurement. Assuming that $\vec{n}$ is parallel to the z-axis, each nanorod in the sample has its own orientation expressed by θ and φ. These nanorods influenced by the external field tends to lower θ but has an isotropic axial symmetry in terms of φ in the plane orthogonal to $\vec{n}$. When the PL emission is observed in a direction perpendicular to $\vec{n}$ (for instance the x-direction) – as for the in-plane switching

mode – two polarization components parallel and perpendicular to $\vec{n}$ can be noted as $\mathbf{I}_{//}$ and $\mathbf{I}_\perp$ which correspond to the $\mathbf{I}_{xz}$ and $\mathbf{I}_{xy}$ respectively. Another component propagating along $\vec{n}$ is noted as $\mathbf{I}_h$ (implying the homeotropic mode) that corresponds to $\mathbf{I}_{zx}$ or $\mathbf{I}_{zy}$, which are now equal due to the isotropic symmetry in φ. The expressions for these three polarized emission components are basically the same as those for a single particle. But note that they are averaged sums over many nanorods with various θ values. For convenience these intensities are normalized to those for a single particle. Thus for ED,

$$I_\| = \langle I_\pi \cos^2 \theta + I_\sigma \sin^2 \theta \rangle \tag{4.17}$$

$$I_\perp = \langle I_\pi \sin^2 \theta \cdot \sin^2 \varphi + I_\sigma (\cos^2 \theta \cdot \sin^2 \varphi + \cos^2 \varphi) \rangle \tag{4.18}$$

$$I_h = I_\perp \tag{4.19}$$

Considering that the $\vec{n}$ director is a cylindrical symmetry axis of the problem, leading to $\langle \sin^2 \varphi \rangle = \langle \cos^2 \varphi \rangle = 1/2$ the above equations can be writen,

$$I_\| = I_\pi \langle \cos^2 \theta \rangle + I_\sigma (1 - \langle \cos^2 \theta \rangle) \tag{4.20}$$

$$I_\perp = I_h = \frac{I_\pi}{2} (1 - \langle \cos^2 \theta \rangle) + \frac{I_\sigma}{2} (1 + \langle \cos^2 \theta \rangle) \tag{4.21}$$

And thus,

$$I_\| + I_\perp = \frac{I_\pi}{2} (1 + \langle \cos^2 \theta \rangle) + \frac{I_\sigma}{2} (3 - \langle \cos^2 \theta \rangle) \tag{4.22}$$

In the same way for a single nanorod, a ratio of the intensity of two distinct peaks in one spectra ($\mathbf{k} = \mathbf{I_1}/\mathbf{I_2}$) provides a solution for $\langle \cos^2 \theta \rangle$.

When the emission is measured on the homeotropic plane,

$$\langle \cos^2 \theta \rangle_{homeo} = \frac{k(I_{2\pi} + I_{2\sigma}) - (I_{1\pi} + I_{1\sigma})}{k(I_{2\pi} - I_{2\sigma}) - (I_{1\pi} - I_{1\sigma})} \tag{4.23}$$

When the observation direction is perpendicular to $\vec{n}$,

$$\langle \cos^2 \theta \rangle_{transverse} = \frac{k(I_{2\pi} + 3I_{2\sigma}) - (I_{1\pi} + 3I_{1\sigma})}{(I_{1\pi} - I_{1\sigma}) - k(I_{2\pi} - I_{2\sigma})} \tag{4.24}$$

Equivalent equations for MD are similarly obtained:

$$I_\perp = I_\sigma \langle \cos^2 \theta \rangle + I_\pi (1 - \langle \cos^2 \theta \rangle) \tag{4.25}$$

$$I_\parallel = I_h = \frac{I_\sigma}{2}(1 - \langle \cos^2 \theta \rangle) + \frac{I_\pi}{2}(1 + \langle \cos^2 \theta \rangle) \tag{4.26}$$

$$I_\parallel + I_\perp = \frac{I_\sigma}{2}(1 + \langle \cos^2 \theta \rangle) + \frac{I_\pi}{2}(3 - \langle \cos^2 \theta \rangle) \tag{4.27}$$

$$\langle \cos^2 \theta \rangle_{homeo} = \frac{k(I_{2\sigma} + I_{2\pi}) - (I_{1\sigma} + I_{1\pi})}{k(I_{2\sigma} - I_{2\pi}) - (I_{1\sigma} - I_{1\pi})} \tag{4.28}$$

$$\langle \cos^2 \theta \rangle_{transverse} = \frac{k(I_{2\sigma} + 3I_{2\pi}) - (I_{1\sigma} + 3I_{1\pi})}{(I_{1\sigma} - I_{1\pi}) - k(I_{2\sigma} - I_{2\pi})} \tag{4.29}$$

Therefore the order parameter ($S = (3\langle \cos^2 \theta \rangle - 1)/2$) can be obtained with $\langle \cos^2 \theta \rangle$ that is calculated from the observed emission spectra regardless of the distribution function of θ. $2\mathbf{I_h}$ or $\mathbf{I_{//}} + \mathbf{I_\perp}$ are the sum of the two orthogonal polarization components that is in fact an intensity measurable at only one time without using a polarizer. Once an emission spectra is obtained from a partially oriented sample with a known $\vec{n}$, the value of S can be extracted from its spectral form. This is a novel concept to deal with the polarized signals without using a polarizer. Excluding polarizers from the optical measurement instrument containing number of mirrors, filters, and gratings eliminates all the troublesome problems arising from their polarization selective performances. Moreover, comparing relative intensities of different peaks to measure the orientation is more precise and reliable than the previous way comparing the total intensity change of a broad spectra. It is because the measured total intensity is often altered by the material density, unstable excitation light, defocusing and so on that are hardly maintained constant during the measurement. All these external uncertainties are eliminated when using the method presented here as the spectral form displays purely the information only about the orientation state. Experimental application of this new concept will be demonstrated in the next section.

General solution for unknown order parameter (S) and director ($\vec{n}$)

The above calculation on the bulk sample was in the simplified case where $\vec{n}$ was fixed as the polarization measurement axis. To get a generalized solution where both S and $\vec{n}$ are unknown is also interesting and is the ultimate goal of this study, because it enables the orientation analysis of bulk samples having complex geometries (e.g. textured LC suspensions, isotropic suspensions under complex flow). Looking at **Figure 4.9** again, imagine the director $\vec{n}$ of a partially oriented bulk sample ($0 \leq S \leq 1$) is angled with θ' and φ' according to the *xy*-plane of measurement normal to the *z*-axis. Now there exist two coordinates: the inner coordinate for the rod orientation (θ, φ) according to $\vec{n}$, and the outer

one of the measurement space for the orientation (θ', φ') of $\vec{n}$. Thanks to the trigonometric relation of the dipolar emission components, the two polarized emission intensities measured on the *xy*-plane (noted as $\mathbf{I_x}$, $\mathbf{I_y}$) can be expressed with $\mathbf{I_{//}}$ and $\mathbf{I_\perp}$ obtained above. And there is again the same parallelism between $(\mathbf{I_x}, \mathbf{I_y})$ and $(\mathbf{I_{zx}}, \mathbf{I_{zy}})$ for a single nanorod as between $\mathbf{I_h}$ and $(\mathbf{I_{zx}}, \mathbf{I_{zy}})$. Thus for ED and MD,

$$I_x = I_\parallel \sin^2 \theta' \cdot \cos^2 \varphi' + I_\perp (\cos^2 \theta' \cdot \cos^2 \varphi' + \sin^2 \varphi') \tag{4.30}$$

$$I_y = I_\parallel \sin^2 \theta' \cdot \sin^2 \varphi' + I_\perp (\cos^2 \theta' \cdot \sin^2 \varphi' + \cos^2 \varphi') \tag{4.31}$$

And thus,

$$I_x + I_y = I = I_\parallel (1 - \cos^2 \theta') + I_\perp (1 + \cos^2 \theta') \tag{4.32}$$

Here again, I (sum of I_x and I_y) is the intensity measurable at one time without a polarizer. By substituting **Equation 4.20** and **4.21** for $I_{//}$ and $I_\perp$ of ED in **Equation 4.32**.

$$I = \frac{I_\pi}{2} (1 + \langle \cos^2 \theta \rangle + \cos^2 \theta' - 3 \langle \cos^2 \theta \rangle \cdot \cos^2 \theta')$$
$$+ \frac{I_\sigma}{2} (3 - \langle \cos^2 \theta \rangle - \cos^2 \theta' + 3 \langle \cos^2 \theta \rangle \cdot \cos^2 \theta') \tag{4.33}$$

Similar to the previous cases, a ratio of the intensity of two distinct peaks in one spectra ($\mathbf{k} = \mathbf{I_1/I_2}$) provides the following equation for $\langle \cos^2 \theta \rangle$ and $\cos^2 \theta'$,

$$\cos^2 \theta' + \langle \cos^2 \theta \rangle - 3 \langle \cos^2 \theta \rangle \cdot \cos^2 \theta' = \frac{k(I_{2\pi} + 3I_{2\sigma}) - (I_{1\pi} + 3I_{1\sigma})}{(I_{1\pi} - I_{1\sigma}) - k(I_{2\pi} - I_{2\sigma})} \tag{4.34}$$

In the same way for MD,

$$I = \frac{I_\pi}{2} (3 - \langle \cos^2 \theta \rangle + \cos^2 \theta' - 3 \langle \cos^2 \theta \rangle \cdot \cos^2 \theta')$$
$$+ \frac{I_\sigma}{2} (1 + \langle \cos^2 \theta \rangle - \cos^2 \theta' + 3 \langle \cos^2 \theta \rangle \cdot \cos^2 \theta') \tag{4.35}$$

$$\cos^2 \theta' - \langle \cos^2 \theta \rangle + 3 \langle \cos^2 \theta \rangle \cdot \cos^2 \theta' = \frac{k(I_{2\sigma} + 3I_{2\pi}) - (I_{1\sigma} + 3I_{1\pi})}{(I_{1\sigma} - I_{1\pi}) - k(I_{2\sigma} - I_{2\pi})} \tag{4.36}$$

The two simultaneous equations from ED and MD (**Equation 4.34** and **4.36**) enables to calculate the two unknown values of $\langle\cos^2\theta\rangle$ and $\cos^2\theta'$. Then the value of $\cos^2\varphi'$ can be calculated using **Equation 4.30** or **4.31** (which correspond to measurements performed with an analyzer). Finally the mirror images can be eliminated as the same way noted for the case of a single nanorod. It should be emphasized that the existence of both ED and MD transition bands is a crucial advantage for the orientation analysis of unknown S and $\vec{n}$. The different nature of π, σ, and α emission polarization between ED and MD levels, which is a unique characteristic of rare-earth luminescence, allows the complete analysis of the orientation state of bulk samples.

4.3.2. Experimental analysis: "Measuring the orientation"

In this section, the theoretically derived method of orientation analysis is examined experimentally. Two different sample types are studied: (1) isotropic LaPO$_4$:Eu nanorod suspension oriented under electric field and (2) a single LaPO$_4$:Eu nanorod.

Isotropic rod suspension under electric field

In Chapter 3, the orientation of LaPO$_4$ nanorods under electric field was described focusing on their birefringent property that can be modulated under varied electric field strength. In these experiments, controllable optical retardation was the intended property which was at the same time the indicator of the degree of orientation. To determine the value of S, however, it was essential to know the cell thickness to calculate birefringence (Δn) and its maximum value (Δn_{sat}) that can only be estimated by fitting many experimental points with **Equation 3.3**. Moreover, it gives only the in-plane contribution of the orientation while polarized PL study enables access to the 3D orientation analysis without a need to measure other parameters. To check its validity, the above electro-optical measurement was indeed conducted with the Eu doped LaPO$_4$ nanorods to conduct both measurements (birefringence & PL) together and compare the results.

Figure 4.1.a is a plot of the emission spectra of the isotropic nanorod suspension without applying the external electric field (black line). As the rod orientation in the isotropic phase is random this spectra is identical in any polarization angle. And the form of this spectra should be the same with the sum of three orthogonal (σ, π, α) emission components of a single nanorod or a perfectly oriented nanorods (S $\approx$ 1) as described in **Equation 4.2** and **4.3**. The red line in the same figure is an equivalent sum of σ, π and α spectra (See **Figure 4.1**) normalized to the black line. Their good match in both the MD and ED transition bands supports the above derived theoretical calculation, and a precise measurement of the orientation state of oriented samples is expectable.
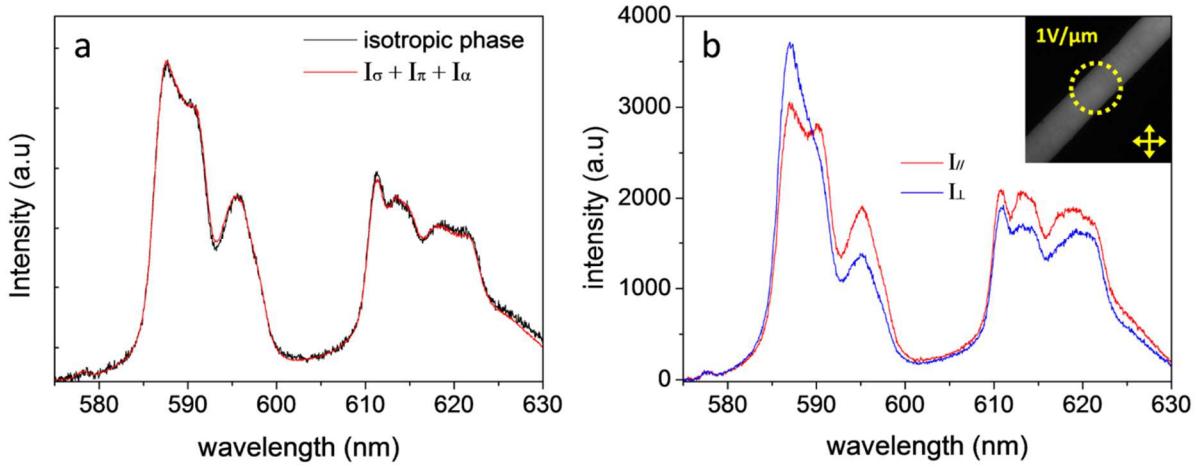
Figure 4.10. (a) PL emission spectra of the isotropic LaPO$_4$:Eu nanorods suspension (black line) and a plot of the equivalent sum of σ, π, and α polarized spectra shown in Figure 4.8 (red line). The intensities of the two spectra are normalized. (b) Polarized PL emission spectra of the same sample in the handmade IPS partially oriented under electric field (1V/µm). The inset is a light transmission micrograph between crossed polarizers (giving the sample birefringence) corresponding to **Figure 3.8**, in which the yellow dotted circle indicates the region of PL emission measurement.

When the electric field is applied, the emission spectra observed with a polarizer split into different forms according to the angle of the polarizer to the direction of the electric field as shown in **Figure 4.10.b**. The inset in this figure shows the birefringence generated due to the rod orientation between the electrode gap under the applied electric field of 1V/µm (It is the same sample of the birefringence measurement using a handmade cell demonstrated in Chapter 3). The polarized PL emission light was collected on the region of yellow dotted circle by using an optical fiber. With these polarized spectra taken on the two orthogonal directions the order parameter can be calculated using **Equation 4.20**, **4.21** for ED and **4.25, 4.26** for MD. Each spectra ($I_{//}$, $I_{\perp}$) were fitted with the reference spectra (I_σ, I_π) separately on the whole range of MD (580~600nm) and ED (605~630nm) to find out the coefficients (A_σ, B_π) for the relation,

$$I_{\parallel,\perp} = A \cdot I_\sigma + B \cdot I_\pi \qquad (4.37)$$

Figure 4.11 shows the fitting result. The blue spectra in **Figure 4.11.a** and the red spectra in **Figure 4.11.b** are the same spectra of ($I_{//}$, $I_{\perp}$) shown in **Figure 4.10.b**, and the green curves in each diagram are the fitted result summing the grey curves indicating $A \cdot I_\sigma$ and $B \cdot I_\pi$. Accordingly, four combination of (A_σ, B_π) values are obtained from each transition mode of each spectra as noted in the table in **Figure 4.11.c**, where the calculated values of $\langle \cos^2 \theta \rangle$ and S are noted together.
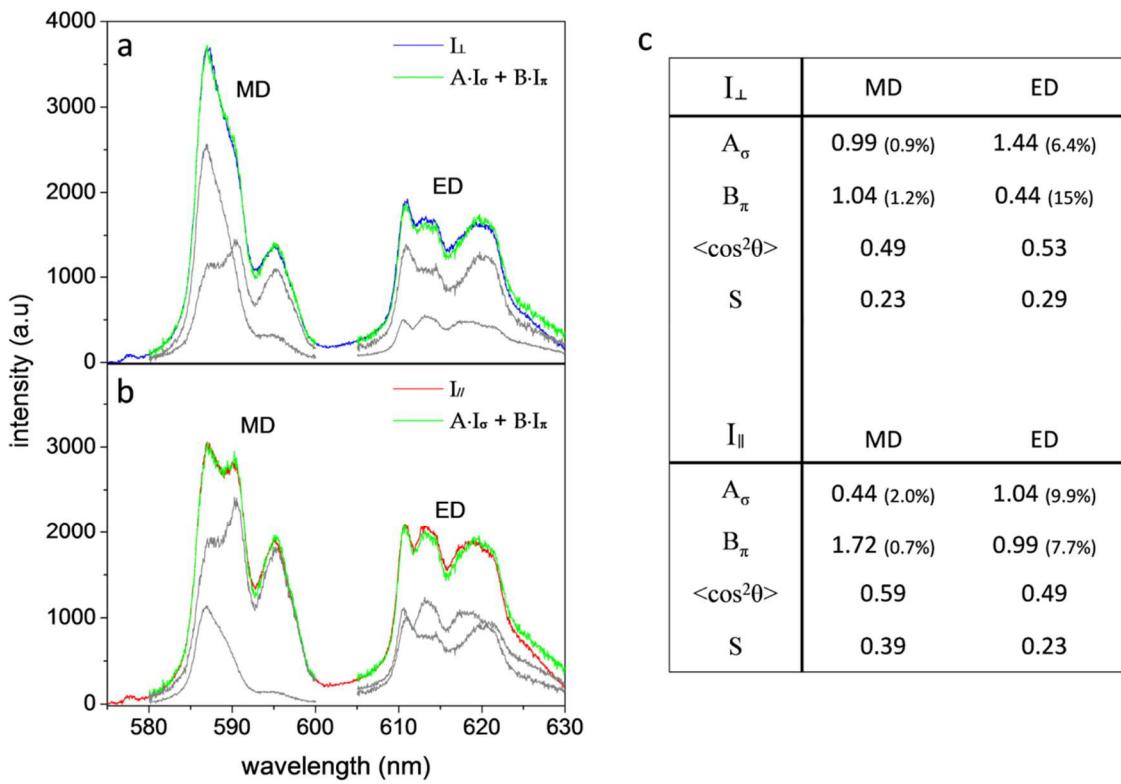
Figure 4.11. (a-b) Polarized emission spectra ($I_{//}$, $I_\perp$) from the IPS cell (blue and red line) and their fitted curve (green lines) as a sum according to **Equation 4.37** of grey lines that are weighted curves of the reference spectra (I_σ, I_π) with the coefficients (A_σ, B_π). (c) Fitted values of the coefficients A_σ and B_π (the values in the parenthesis are the 2-sigma uncertitudes) and the calculated values of $\langle \cos^2 \theta \rangle$ and S.

The obtained values of $\langle \cos^2 \theta \rangle$ and S are not the same for different fittings. Considering the uncertainty values on the ED band that are roughly one-order-of-magnitude larger than those on the MD band, the results on the MD band would be more reliable. The large uncertainty on the ED band seems owing to the non-identical cell geometry between the handmade IPS cell and the homeotropic cell used for collecting the reference spectra. The PL emission response toward the spectrometer might be altered, and the spectral mismatch becomes larger at longer wavelength where there is an ED band. The uncertainty values on the MD band are satisfactory as it is visualized by the good match of the fitted curves. Nevertheless, the calculated values of $\langle \cos^2 \theta \rangle$ and S on the MD band are still very different between $I_{//}$ (S = 0.39) and $I_\perp$ spectra (S = 0.23) and higher with $I_{//}$ spectra. This is not an error or the inaccuracy of the presented method as an orientation analysis tool. In fact, the rod orientation in the IPS cell does not have a perfect cylindrical symmetry as assumed for the theoretical calculation of $I_{//}$ and $I_\perp$ because of the cell thickness that is comparable with the electrode gap distance. As schematized in **Figure 3.3**, the nanorods apart from the bottom plate – electrode surface – would have a significant out-of-plane contribution along the electric field lines. Therefore the S value obtained from $I_{//}$ spectra on the MD band should be

higher than that from $I_\perp$ spectra because the out-of-plane deviation is not reflected on the π-spectra ($I_\pi = I_\alpha$) in case of MD band. This should be contrary on the ED band as $I_\sigma = I_\alpha$ for electric dipoles. And it is confirmed by the S value higher with $I_\perp$ spectra (S = 0.29) than with $I_{//}$ spectra (S = 0.23) regardless of their uncertainty. Such a discrepancy between the calculated S values on different polarization angle thus provides additional information about how much the orientation is distorted from the cylindrical symmetry. The S = 0.39 calculated from the MD band of the $I_{//}$ spectra can be compared with that estimated by fitting the birefringence measurement data shown in **Figure 3.9** noting that both implies the in-plane contribution of the rod orientation. S estimated from birefringence data is 0.36 (as Δn = 0.00127 when applying 1V/µm and Δn_{sat} = 0.00355), which is close to 0.39 obtained from polarized PL analysis.

Single nanorod

This experimental work was conducted using the instrument at Van't Hoff institute for molecular sciences – Amsterdam university, in collaboration with the group of Prof. Fred Brouwer under financial support of LaserLab Europe.

The theoretical background explaining the polarized PL emission of europium with the selection rule is solid. As it originates from the intrinsic anisotropic crystalline structure, the polarization effect observed with the oriented bulk systems is not a collective effect and believed to be the same for a single nanorod. Therefore it would be promising to utilized a single $LaPO_4$:Eu nanorod as an orientation indicating marker. Single particle or single molecule fluorescent markers have widely been used especially in the field of biological science for detecting sub-micrometer scale objects such as proteins, enzymes, or DNAs. Sensing the orientation or rotating motion of these objects are often interesting and has been succeeded only by an indirect way.[151-152] Many advantageous polarized emission properties based on the crystal-field splitting of rare-earth luminescence would be fruitful for future researches on complex bio-molecular structures and motions. As a basis for this, the polarized PL emission of single $LaPO_4$:Eu nanorods is demonstrated here confirming that their polarization nature is the same with that of oriented bulk systems.

The single particle experiment requires a high power excitation source and a high-resolution scanning confocal microscopy system equipped with sensitive photo-detector and spectrometer. Single wavelength (394nm) high power laser light was generated by a Chameleon Laser (Coherent Inc.) and a second harmonic generator (A.P.E) as a PL excitation source. And the confocal system was equipped with an inverted microscope (Olympus IX71), single photon avalanche diodes (SPAD – Perkin Elmer), and a Peltier-cooled spectrometer (Spectra-Pro150 – Acton Research Corp.). The detailed scheme of the confocal set-up is shown in **Appendix 3**.

Visualization of single particle emission was approached by two steps: (1) detecting the positions of nanorods sparsely deposited with random orientation on a substrate by 2D scanning with SPADs and (2) collecting the polarized emission spectra on the found spots with the spectrometer. **Figure 4.12.a** shows the scanned map (5µm × 5µm) of $LaPO_4$:Eu

nanorods in this way. One can see there exist several positions with an emission signal distinct to the background response with a spot size close to one micrometer. Therefore, the confocal resolution on the measurement plane is about 1µm and the size of the nanorod in each spot is smaller than this. The relatively big spot (#1) seems to be an aggregate and the others to be single particles or just a bundle of a coupe of nanorods together which would not show the collective anisotropic effect even if it exists on bulk oriented samples. The emission spectra collected with a fixed polarizer angle on each numbered spot is shown in **Figure 4.12.b**. The background signal obtained on a position without nanorods (BL) was subtracted from each emission spectra as a baseline. These polarized spectra clearly show different forms similar to those obtained from bulk samples (**Figure 4.4**). The nanorod in the spot #2 seems to be oriented almost parallel to the polarizer as its emission spectral form (red line) resembles π-spectra shown in **Figure 4.8.a**. And the nanorod orientation in the spot #4 would be closer to the perpendicular position as the blue line is alike with the σ-spectra. It should be noted that the total emission intensity from each spot is different to each other which should be depending on the size of the single particle or the bundles, however, their orientation could be easily characterized by their emission spectral forms regardless of the total intensity.
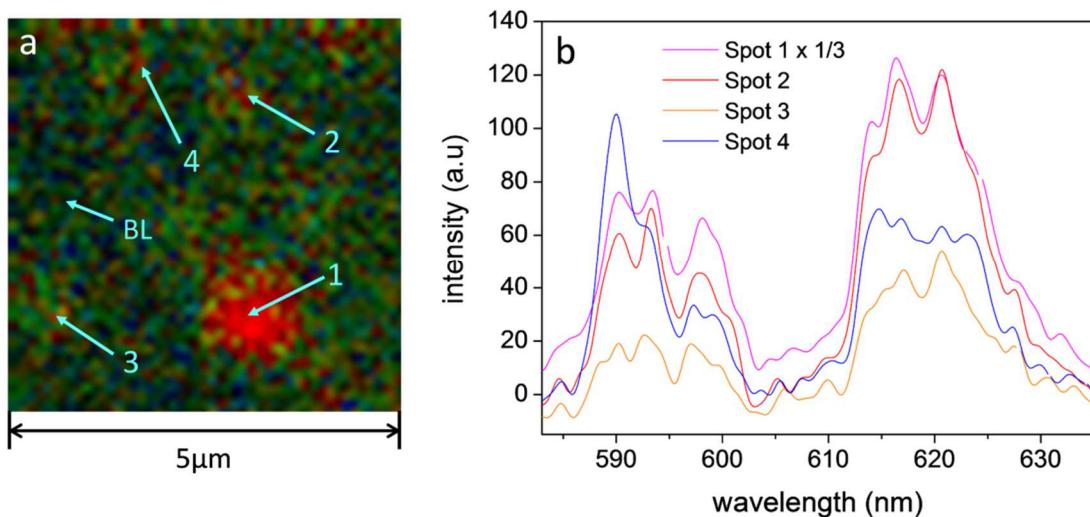
Figure 4.12. (a) Confocal scanning map of a single-particle grade sample (size: 5µm × 5µm). The spots numbered and indicated by arrows are where the nanorods are detected. The spot notted as BL is where the background emission spectra was collected as a spectral baseline (b) The baseline subtracted and smoothed (5-point FFT) emission spectra obtained with a fixed polarizer angle on each numbered spots in (a). The pink line corresponding to the big spot (#1) was plot with a 1/3 intensity.

To confirm if the orientation of a single nanorod really matches with the estimation from its polarized emission spectra, similar experiment was carefully repeated on a sample substrate with a gold micro-grill structure fabricated by a lithographic method. This grill with a square hole size of 30µm × 30µm enables to find the relative position of the spots where nanorods

are detected by confocal scanning. **Figure 4.13.a-c** shows the scanning procedure zooming into a small region until single nanoparticles can be detected. The single particle spots scanned by confocal microscopy could be observed again by SEM tracking the same position on the grill. The exact orientation of the nanorod can thus be verified with the SEM picture. **Figure 4.13.d-e** displays respectively a SEM image of a single nanorod with a length of 250nm visualized in this way and its polarized emission spectra in two orthogonal angles of the polarizer, -45° and 45° relative to the horizontal line in the SEM image. As the nanorod is angled 35° in the SEM image, the angle between the nanorod and the polarizer is 80° and 10° respectively. The spectral forms similar to the σ- and π-spectra in **Figure 4.8.a** are anticipated for these angles and so they are in **Figure 4.13.e**. The quantitative analysis by the spectral fitting is not presented here because of the noise and the spectral distortion that have to be carefully treated (This work is currently ongoing). Anyway the PL emission spectra of a single nanorod are clearly shown to be polarized in the same way observed with the oriented bulk samples.
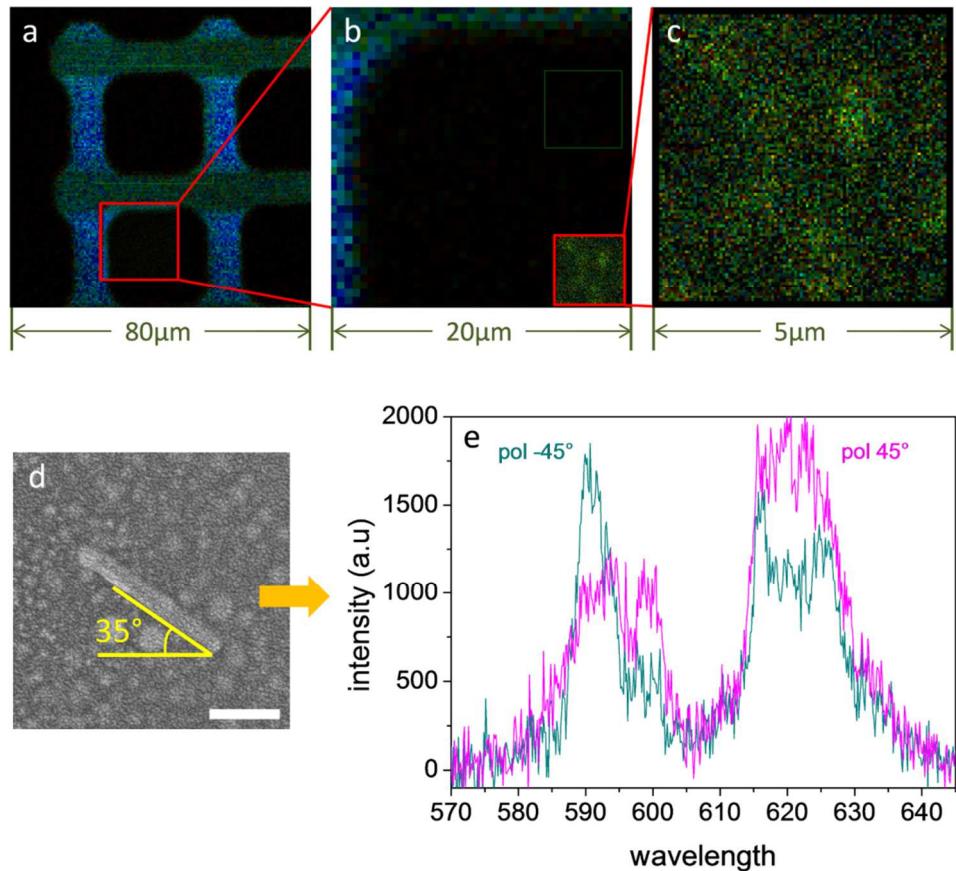
Figure 4.13. (a-c) Confocal scanning images in different magnification scales displaying how to find a single particle spot on a known position. (d) SEM image of a single LaPO$_4$:Eu nanorod traced in the same way after the confocal microscopy. The round particles beside are the residual gold particles after the lithography process. The rod axis is angled 35° to the horizontal axis and the scale bar indicates 100nm. (e) PL emission spectra collected from the nanorod shown in (d) with a polarizer angled -45° and 45° to the same horizontal axis in (d).

4.4. Application for microfluidics

With the arising research and development of today on microfluidic devices, there is a huge demand for new methods to investigate characteristics of flow in the microscopic scale. Yet, there exist very few and inconvenient experimental tools for profiling the basic flow parameters such as flow velocity or shear stress.[153] Particle imaging velocimetry (PIV) is one, and may be a sole, conventionally used technique, which is based on tracking many fluorescent microparticles floating in the flowing medium. PIV is a well-developed powerful technique[154-155], but it requires a heavy and time consuming data processing for tracking the positions of many particles captured on a stack of photographs taken by high-speed camera. The more focusing on the smaller scale and the more complex the flow is, the more noisy and difficult to analyze the PIV results become. Moreover, it is often used to catch a snapshot of a flow profile but not appropriate for a continuous long term observation because of the huge amount of data. Therefore a more simple, precise, and swift new method is aspired for various microfluidics researches. One particular demand in this field is to measure directly and precisely the three-dimensional shear-field of a geometrically complex flow, which is hardly accessed by PIV or other techniques looking at the *velocity* but *not shear*.[153] Observing microscopic shear-profile in the curved flow, near the wall, or of a viscous medium is essential for understanding many interesting phenomena such as surface reaction, capillary blood flow, coagulation, cleaning and mixing and so on. In this final section we investigate how the outstanding anisotropic optical properties – polarized PL emission and large birefringence – of the LaPO$_4$:Eu nanorod suspension can provide a fruitful solution for such demands.

4.4.1. Maxwell effect and stress-optical law

The coincidence of the geometrical anisotropy and the polarized PL emission property in the crystalline LaPO$_4$:Eu nanorod has been the connecting link of the anisotropic optical response with the particle orientation dynamics such as LC behavior and shear-induced nanorod alignment. As discussed in chapter 3 for making rod-aligned thin film structure, anisotropic objects composing or dispersed in a flowing medium have a strong tendency to orient along the direction of shear generating temporary birefringence. The correlation between the hydrodynamic parameter (shear stress) and the induced optical anisotropy (birefringence) was first described by Clerk Maxwell, as it is so called 'Maxwell effect'. Then Raman and Krishnan provided its solid interpretation applying the Boltzmann thermal diffusion as an opposing force of the hydrodynamic orientation.[76, 156-157] Based on this theory applicable to all sorts of pure liquids and colloidal suspensions, stress-optical analysis – a method to study rheological properties of liquids conveniently by optical measurement – was developed as one of the principal analysis tools in rheology.[77, 158-160] The detail of the theory and the exemplary experimental studies are very well described in the review of Scheraga *et al*.[159] The key concept of the theory is that the orientational order parameter (S) is an increasing function of a ratio of the shear rate ($\dot{\gamma}$) and the rotary diffusion constant (Θ) that is indicated by the parameter $\alpha = \dot{\gamma} / \Theta$. For prolate ellipsoids Θ is given as,

$$\Theta = \frac{3k_bT}{16\pi\eta_0 a^3}\left(-1 + 2ln\frac{2a}{b}\right) \qquad (4.38)$$

where η_0 is the solvent viscosity, a and b are the semi-axes of the ellipsoids. For small $\boldsymbol{\alpha} < 1.5$, a solution of the orientation distribution function[159] can be approximated leading a simple proportionality between S and $\boldsymbol{\alpha}$ as,

$$S = \frac{\boldsymbol{\alpha}R}{15} = \frac{\dot{\gamma}R}{15\Theta} \quad ; \quad R = \frac{p^2 - 1}{p^2 + 1} \quad ; \quad p = \frac{a}{b} \qquad (4.39)$$

One can see in **Equation 4.38** that the a^3 in the denominator decreases a lot when the size of the particle increases. Thus the orientation of colloidal particles such as LaPO₄ nanorods that are a couple of orders of magnitude bigger than pure liquid molecules would be less disturbed by the thermal diffusion and more efficiently oriented with a large value of $\boldsymbol{\alpha} > 1.5$ with a moderate $\dot{\gamma}$. In this case, the approximation in **Equation 4.39** is no more valid and a complete numerical solution of the distribution function is required. **Figure 4.14** shows a plot of this solution showing the gap between a small and large aspect ratios (p).[161]
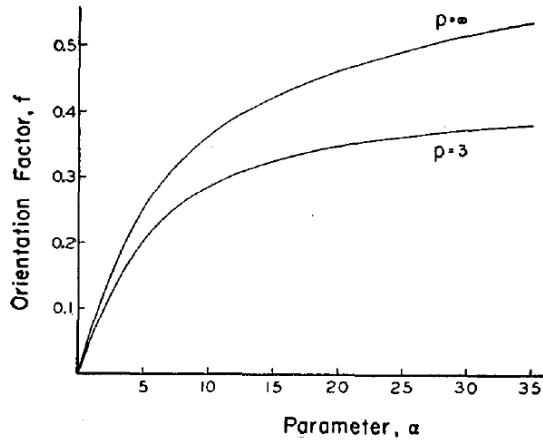
Figure 4.14. A plot of orientational order parameter, S (noted in the figure as orientation factor, *f*), according to the parameter $\boldsymbol{\alpha}$ with its dependence on the aspect ratio *p*. *Figure taken from the reference paper[161]*

As the birefringence of the system is directly proportional to S, the ordinary axis can be substituted by one for *Δn*. And the value of $\boldsymbol{\alpha}$ consisting of the information of flow parameters such as $\dot{\gamma}$ and η_0 can be obtained by measuring birefringence.

Considering such a clear description of the correlation between the shear and birefringence of flowing media, one can expect to apply this stress-optical law for measuring the unknown shear in microfluidic channels. Nonetheless, there have been some obvious limits. When using conventional molecular liquids that show very low birefringence, a long light pathway typically over centimeters is required to obtain a sufficient amount of optical retardation.[162] Also, basically it only allows two-dimensional analysis as birefringence is an integrated signal of the retardation of the light passing throughout the sample.[162-163] Liquid crystalline (LC) polymers exhibiting large birefringence have sometimes been used for microfluidic analysis.[164] But it seems that their own very complex and non-Newtonian flow behavior is already hard to interpret[82, 85, 87, 165] as also discussed in Chapter 3.

Colloidal suspensions of LaPO$_4$:Eu nanorods offer a new possibility. As shown for the electro-optical analysis, even a colloidal suspension with a low density (Φ < 2%) exhibits significant optical retardation inside a thin gap (60µm) of the IPS cell which is comparable to the scale of the typical microfluidic channels. Such a dilute suspension would maintain the basic flow properties of the solvent. As these nanorods are dispersible in water, ethylene glycol, and presumably in many other solvents, stress-optical analysis in standard experimental conditions of the microscopic flow becomes available. Above all things, the polarized PL emission of the nanorods enables the analysis of the three-dimensional (3D) shear-field as the emission can be collected from a given point source in a 3D space. The value of $\dot{\gamma}$ and its direction at each point spot can be determined by the stress-optical law from the value of S and the direction of $\vec{n}$ obtained with the polarized emission signal. Scanning many point spots in the interested region of flow would finally provide a 3D map of a shear-field. A validity of this concept is experimentally demonstrated below.

4.4.2. Measuring birefringence and polarized photoluminescence under flow

The microfluidics study shown here was conducted in collaboration with the group of Charles Baroud at Laboratoire d'hydrodynamique de l'Ecole Polytechnique (Ladhyx).

Basic experimental tools with a simple microfluidic channel and a syringe pump was used on our principal polarization microscopy set-up (See **Appendix 3**). The channel has a straight rectangular geometry with a width (*w*) of 110µm and a height (*h*) of 100µm. An isotropic phase LaPO$_4$:Eu nanorod suspension in ethylene glycol (EG) diluted (Φ = 1.5%) from the same sample lot for the above demonstrated PL measurements was used. By varying the flow rate (Q) of this suspension in the channel, birefringence and polarized PL emission were observed together. The measurement region for both was a small spot with a diameter of ~100µm (similar to the channel width) on the center of the channel

Figure 4.15 shows the result data. The polarized spectra for a given Q are plotted in each diagram with an inset polarization micrograph displaying the channel brightened by birefringence generated during the flow through it. Q was varied gradually in a log-scale range from 10 to 3333µL/min for (a) to (f) that correspond to the shear rate ($\dot{\gamma}$) of 0.9 to 300s^{-1} as $\dot{\gamma}$ = 6Q/wh^2 in a rectangular channel. For the calculation of S from the polarized PL

spectra, the MD band emission perpendicular to the flow direction ($I_\perp$) was taken because fitting on it allows a smallest error due to the high contrast between the sublevel peaks. The values of the normalized coefficients (A_σ, B_π) obtained by the fitting with the reference spectra (I_σ, I_π) are noted together with their plots in each diagram.
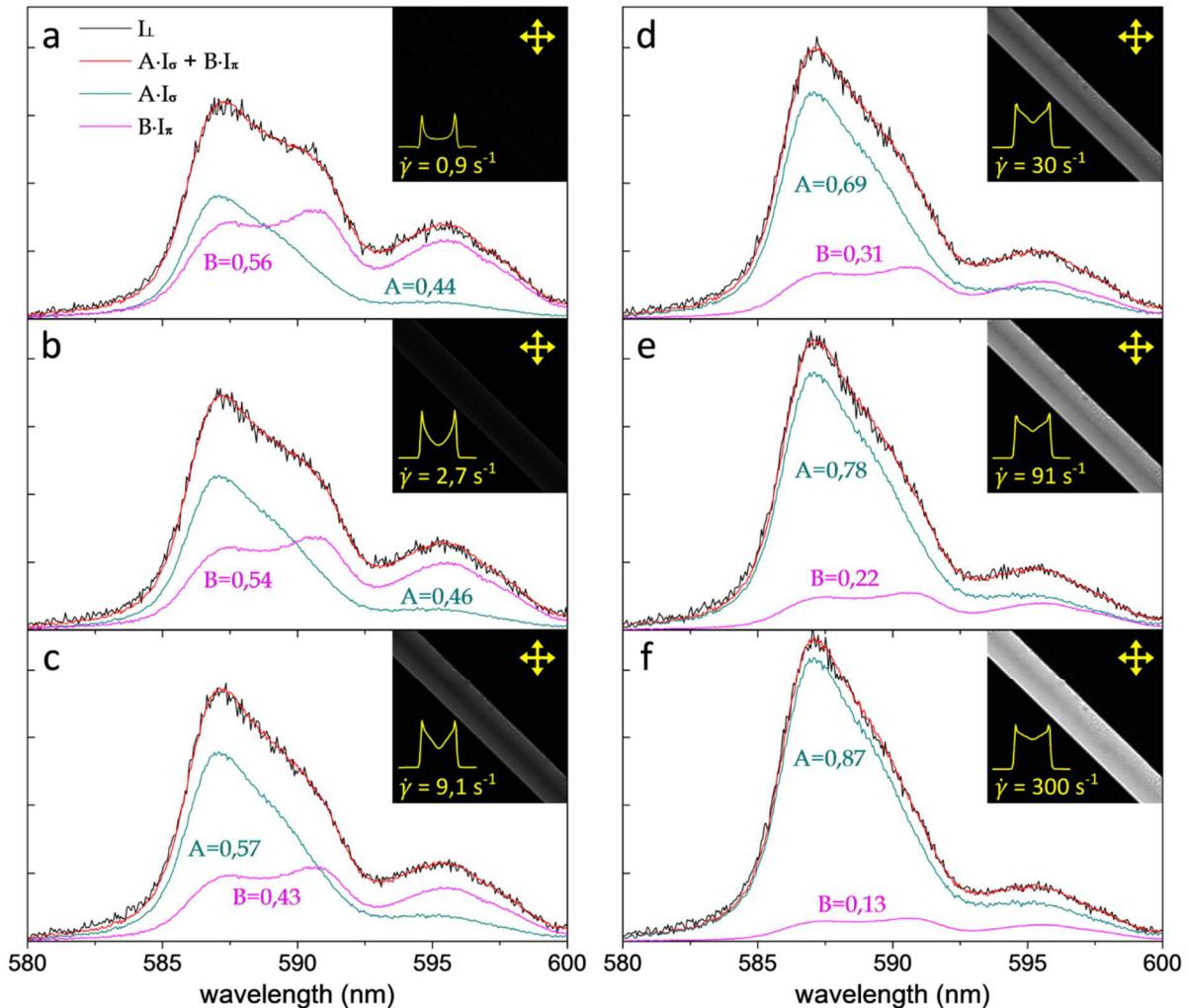
Figure 4.15. Polarized PL emission spectra of LaPO$_4$:Eu nanorod suspension in ethylene glycol flowing through a microfluidic channel (*width* = 110µm, *height* = 100µm) taken with a polarizer perpendicular to the flow direction ($I_\perp$) and its fitting data with the reference σ- and α-spectra (I_σ, I_π) Each of six diagrams (a to f) corresponds to a different flow rate (Q) that was varied on the log-scale from 10 to 3333µL/min. The inset in each diagram is a polarization micrograph of the channel generating birefringence due to the rod orientation under shear. The shear rate values corresponding to Q and the normalized retardation intensity profile across the channel are noted together.

The $I_\perp$ spectra (black line) in **Figure 4.15.a** ($\dot{\gamma}$ = 0.9s^{-1}) has a form very close to that of an isotropic phase shown in **Figure 4.10.a**. And it is changing gradually to the form close to I_σ when increasing the flow rate from (a) to (f). This indicates the LaPO$_4$ nanorods are

temporarily oriented according to the flow with the increase of S when increasing $\dot{\gamma}$. Fitting these spectra with the reference spectra ($\mathbf{I_\sigma}$, $\mathbf{I_\pi}$) according to **Equation 4.37** gives the ratio between A_σ and B_π from which the S values can be calculated by **Equation 4.25**. The very good match of the fitted spectra (red line) with the $\mathbf{I_\perp}$ spectra reflects the reliability of the fitting result. And the high value of A_σ at high $\dot{\gamma}$ evidences that S reaches high not far from 1 and so shear-field is a driving force of orientation as efficient as electric field. Meanwhile, the inset micrographs in the same figure also show the increase of birefringence when increasing $\dot{\gamma}$ as predicted by the stress-optical law. The amount of optical retardation (δ) is considerably high (δ = 80nm when $\dot{\gamma}$ = 91s^{-1}) and sufficient for a precise measurement only throughout the small height (h = 100μm) of the microfluidic channel. Therefore, stress-optical analysis is now available in microfluidic systems by using two distinct optical responses: birefringence and polarized PL emission.

Figure 4.16 – the same diagrams with the *x*-axes in linear scale-(**a**) and log scale-(**b**) – shows these two parallel data together. The green circular points indicate the S values (right *y*-axis) obtained from the polarized PL emission and the pink triangular points indicate δ (left *y*-axis) both according to $\dot{\gamma}$ (bottom *x*-axis). As expected with the direct proportionality between $\varDelta n$ and S, they show a good match of the increasing and saturating tendency cross-checking the reliability of each other. And these data are fitted well with the theoretical plot by the stress-optical law (blue line according to $\boldsymbol{\alpha}$ corresponding to the top *x*-axis) which was taken from the numerical calculation for p = 25 from the reference paper[161]. The rotary diffusion constant (Θ) for this fitting is 1s^{-1}, thus the scale of $\dot{\gamma}$ and $\boldsymbol{\alpha}$ on the bottom and top *x*-axis are identical. The Θ value for the sample suspension can be calculated by **Equation 4.38**. The approximated value obtained with the average dimensions of the nanorods and the suspension viscosity is 8.3s^{-1}. And it is in the same order of magnitude with the estimation by the fitting (1s^{-1}). This should be a good match considering the high sensitivity of Θ on the particle size ($\Theta \propto 1/a^3$) supporting the validity of the stress optical law for the inorganic colloidal nanorod suspension. Indeed, the theory for Θ assumes there is no interparticle interaction. In the real system, however, nanorods are highly charged so that there exists a strong repulsive force among each other, which was the driving force of the LC behavior at a density lower than the Onsager's theoretical prediction for non-interacting hard rods (See Chapter 2). This repulsive interaction positive for the rod orientation seems to be the main reason for the empirical value of Θ = 1s^{-1} somewhat lower than the theoretical value (8.3s^{-1}). The significant deviation of the experimental point where $\dot{\gamma}$ = 300s^{-1} (**Figure 4.16.b**) can also be explained in the same context. Although the theoretical system is very hard to obtain S close to 1 even with a very high $\dot{\gamma}$, the spontaneous orientation tendency of LaPO$_4$ nanorods may assist to reach higher S.
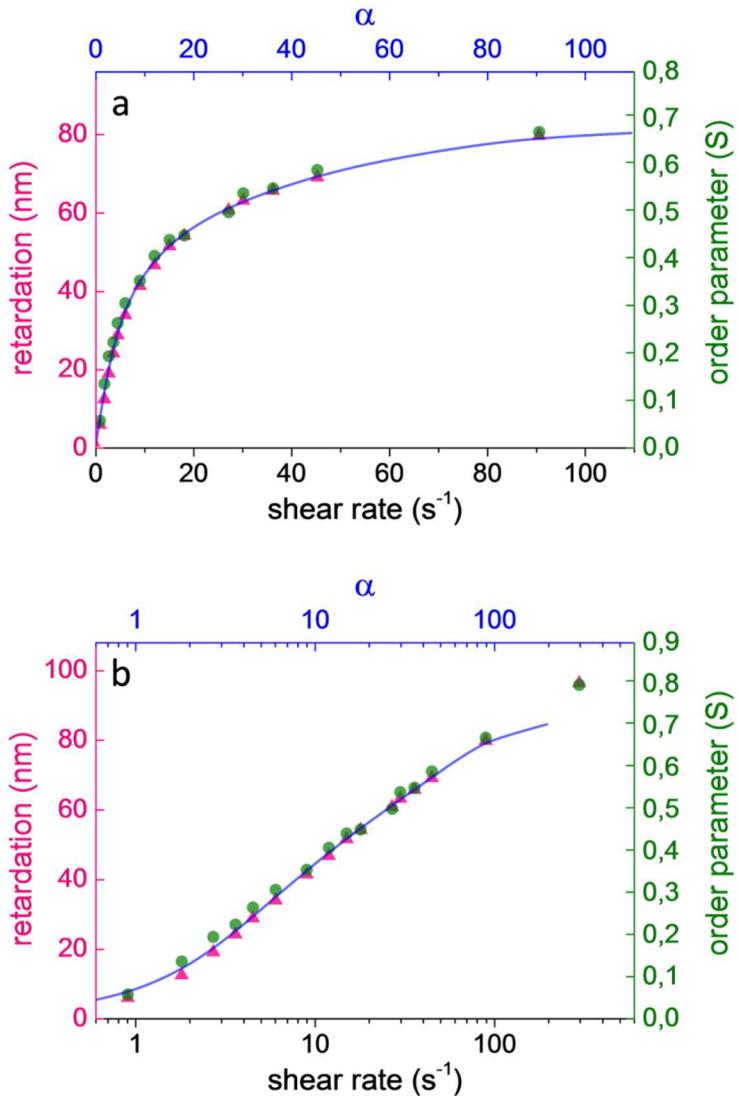
Figure 4.16. Optical retardation (pink triangles) and the order parameter (green circles) according to the shear rate corresponding to **Figure 4.15**. The blue line is a theoretical plot of S according to α fitted to the data by adjusting the value of Θ as 1s^{-1}. (a) and (b) shows the same data in linear and log-scale x-axis respectively.

From the data shown in **Figure 4.15** and **Figure 4.16**, it is verified that both the birefringence and polarized PL emission results enable the reliable estimation of $\dot{\gamma}$ that follows the stress-optical law. According to the needs, shear stress, flow rates, and viscosity can be calculated from the obtained $\dot{\gamma}$. Though the presented analysis averaged the optical responses on the whole width of the channel regardless of the flow profile inside, the same study at a smaller scale is possible if the measurement spot size is reduced. The yellow plots in the insets in **Figure 4.15** are the normalized retardation intensity profiles across the channel, and they display the shear-field profile on the plane parallel to the channel substrate. The profile at very low shear ($\dot{\gamma}$ = 0.9s^{-1}) is flat in the middle of the channel and the intensity increases rapidly near the wall. The profile becomes parabolic when $\dot{\gamma}$ = 2.7s^{-1}, and it finally becomes wedge shape when $\dot{\gamma}$ is further increased ($\dot{\gamma} \geq$ 9.1s^{-1}). Thus it can be said that the flow profile

is changed when $\dot{\gamma}$ is varied. And it is surmised that a non-Newtonian behavior appears at very low $\dot{\gamma}$ due to the interactions among nanorods that becomes significant for the flow property at rest or at a very slow movement. Unfortunately, it is hard to quantitatively analyze these birefringence profiles to obtain the shear profiles because they are indeed affected by the shear applied by the bottom and top walls parallel to the measurement plane. As stated earlier, birefringence measurement only allows 2D analysis which is only possible with a high *h/w* aspect ratio channel. Despite this apparent limit, birefringence is still very useful because it is visible in real-time allowing a time-resolved observation of the approximate profiles and the averaged shear rates without a complicated data treatment. Simply taking photographs such as the inset figures in **Figure 4.15** is enough to extract the general information on the whole channel area in the image at a given moment. Besides, a concrete 3D analysis is possible with the polarized PL property by means of conventional laser scanning confocal microscopy. When the laser excitation source is concentrated on a tiny confocal spot inside the flow and the polarized emission from the same spot is read, the shear vector at that point can be calculated. Scanning many spots in this way on the 3D space would enable to draw a 3D shear-field map. This experimental work is currently on going in collaboration with the Fred Brouwer group at Amsterdam university together with the single particle measurement using their confocal instrument.

4.5. Conclusion

Polarized luminescence in general aspect has been a global intensity variation of a broad single emission peak that is sensitive to the excitation polarization. Such effect has been observed from most types of phosphors, however, it was found that there is a striking difference on the polarization of the europium ions doped in the $LaPO_4$ nanorods. Each sharp peak corresponding to the degenerate transition sublevels is polarized in different sense due to the crystal-field splitting. Also, this polarization is independent on the excitation polarization because of the non-radiative relaxation process between the final state of the excitation transition and the initial state of the recombination transition. Observation and control of such a unique aspect of the rare earth PL polarization became available thanks to the novel method to control the orientation of $LaPO_4$:Eu nanorods in bulk colloidal suspensions by utilizing the spontaneous LC behavior, shear-directed assembly, and the external electric field. Theoretical study on the polarized emission propagation revealed that comparing the relative intensity variation of different peaks, i.e., fitting the spectra, provide the information on the orientation state – the director ($\vec{n}$) and the order parameter (S) – of either single particles or partially oriented bulk samples regardless of the total intensity change. This becomes a robust advantage allowing a precise orientation measurement of the unknown samples. An application to the analysis of microfluidic systems is suggested opening a new way to visualize three dimensional shear profiles in complex flow. Experimental studies in-depth on microfluidics and single particle PL are now ongoing.

※ Experimental detail ※

Synthesis of LaPO₄ nanorods doped with Eu & Ce:Tb

Doped nanorods were made simply by mixing the equimolar Eu^{3+}, Ce^{3+}, and Tb^{3+} ion precursor solutions with the La^{3+} precursor solution with the intended ratio before initiating the precipitation reaction. Trinitrate salt – $Ln(NO_3)_3$ – were used for all lanthanides to do not change the solution properties. The other procedure is the same with the standard method of nanorod synthesis noted in Chapter 2.

Excitation sources

Three different excitation sources were used in this study. For the measurement of colloidal suspensions under UV excitation without polarization analysis (**Figure 4.2**), the Xenon lamp equipped in the commercial spectrofluorometer (FluoroMax-4, Horiba) was used to obtain intense UV light at 260nm. For the measurement of bulk aligned samples (rod aligned film, nematic phases, elctro-optical cells, and microfluidic channels) on the polarization microscope, an intense source near 394nm ($^7F_0$-$^5L_6$ line) was required because typical optical lenses in the microscope system is not transparent under UV light. Instead, an InGaN LED performing a peak wavelength of 395nm with a narrow half width ($\Delta\lambda$ = 14nm) and the optical output power of 100mW (SMB1W-395, Roithner Laser Technik) was selected. This LED chip was placed at the epi-illuminator position of the microscope (See **Appendix 1**) with a collimator lens to irradiate the focal point of the samples through the objective. For the single particle measurement by the laser scanning confocal microscopy (Fred Brouwer group), high power monochromatic laser was used (Chameleon Laser, Coherent Inc. & Second harmonic generator, A.P.E.). The laser light adjusted exactly at 394nm was guided to the confocal microscope objective (See **Appendix 3**) and concentrated on a small focal point with a diameter less than 1μm. The laser power entering to the microscope objective was controlled in the range of 0 ~ 50mW and the beam width was about 5mm.

Polarized emission detection

As for the excitation sources, emission detectors were also different in different set-ups. The emission from bulk suspension under UV excitation was detected with the spectrometer equipped in the same commercial spectrofluorometer. For the principal measurements on the polarizing microscope, a liquid nitrogen-cooled spectrometer (SpectraPro-300i, ARC) was used with the high spectral resolution grating (1200g/mm) centered at 603nm on the middle of the MD and ED peaks. The emission signals were guided toward the spectrometer by a multimode optical fiber ($\emptyset$ = 600μm, M29L05-ThorLabs /$\emptyset$ = 600μm, Oceanoptics). The acquisition time was adjusted to get sufficiently intense signals over noise according to the excitation intensity and the sample density. But of course it was fixed for the measurement on the same samples when varying other parameters. The typical acquisition time was about

a couple of minutes. For the confocal microscopy of single particles, a Peltier-cooled spectrometer (SpectraPro150, A.R.C) was used also connected to the confocal box by an optical fiber. A critical part of the measurement was the sensitivity of the spectrometer gratings to the polarization angle. Thus for all the measurement on the polarization microscope, a linear polarizer was always fixed and the sample was turned to modify the orientation angle relative to the polarizer angle as the sample stage could be precisely centered and turned with 0.1° angular precision. In case of confocal microscopy where the sample should be fixed, a circular polarizer (linear polarizer assembled with a quarter-wave plate) was used so that the circularly polarized outgoing spectra could be detected by the spectrometer independent of the polarizer angle. All the polarizers used in this study were polaroid® films (HN series), and the fluctuating baseline due to these polarizers were always subtracted in the end from the recorded emission spectra.

Sample preparation

Aligned films of doped $LaPO_4$ nanorods were prepared in the same way described in Chapter 3. Sheared nematic sample was prepared simply by injecting the suspension into a commercial homeotropic switching cells (Instec Inc). The capillary flow of the viscous nematic suspension inside the thin gap automatically applied a large shear to obtain a high order of in-plane orientation. Electro-optical measurement by handmade IPS cells was also conducted in the same way noted in Chapter 3. Single particle sample was prepared on thin quartz cover slips (100µm-thick, UQG optics) to minimize the background emission under high-power laser irradiation. Gold grills were fabricated on the quartz slip through typical photolithography process with the help of Joseph Lautru (Ingénieur d'études – Institute d'Alembert, ENS Cachan). The slip with gold grills was carefully cleaned by sonication in the surfactant solution (Helamnex) in deionized water for more than 1 hour and in pure deionized water for 30 minutes. Then it was passed into the UV-ozone treatment for 1 hour. $LaPO_4{:}Eu$ nanorods diluted to $\Phi = 5{\cdot}10^{-4}$ % was spin-coated on the cleaned slip (2500rpm / 2min). Microfluidic channels were fabricated using the equipment of the microfluidics group of Charles Baroud at Laboratoire d'hydrodynamique de l'Ecole Polytechnique (Ladhyx). A standard glass syringe (100µL, Hamilton) and syringe pump (KDS) were used for the injection.

Conclusion

This thesis study began with the consideration on exploiting the intrinsic anisotropic properties of minerals that have often been left out unless a macroscopically grown single crystal was used. Reviewing the past researches on mineral liquid crystals, we explored a way to achieve it by using a bulk system composed of nanocrystals. A carefully designed colloidal liquid crystal system composed of $LaPO_4$ enabled to exhibit two remarkable intrinsic optical anisotropies that are birefringence and polarized photo-luminescence.

The theoretical and experimental studies in this work were not ended at the stage of academic discussions but were progressed towards the practical device applications. Optical Kerr cells and thin film waveplates, constructed from colloidal suspensions of $LaPO_4$ nanorods are qualified to complement or to replace the existing devices, and expected to provide access to some novel applications. Such a good performance could be obtained through the careful observation, deliberate theoretical consideration, and the elaboration of the material synthesis prior to the application study. It is clear that all the advantageous optical and liquid crystalline characteristics emerged from the outstanding colloidal stability achieved by the initial stage of the project on the synthesis optimization and the use of ethylene glycol as a dispersion medium.

It is true that a large part of this work was devoted to the application studies. However, it should not be regarded as a simple intent to develop some specific device materials to replace the existing ones such as organic liquid crystals. The emphasis should be put on the original ideas and concepts that are generalizable for the various synthetic or natural nanocrystalline compounds to make use of their distinct anisotropic physical properties. The $LaPO_4$ system is just an example that verifies the validity of the developed methodologies: (1) colloidal dispersion by transferring the nanorods into a non-aqueous medium, (2) directed-assembly by using thixotropic rod gels, (3) combination of intrinsic and structural anisotropy together, and (4) utilizing the anisotropic optical properties as an analytic tool for the orientation measurement.

Finally, we should emphasize on the original idea of using the newly discovered polarized photoluminescence as an orientation-indicating marker or a new stress optical analysis tool, which may have a great impact on some research fields such as bio-optics and microfluidics. The fundamental theoretical and experimental validity of the idea was confirmed in the final chapter, but other more detailed and interesting experimental works are still undergoing and are not reported here.

※ The scientific publications issued during this thesis work are listed below.

Journal articles

J Kim, J Peretti, K Lahlil, J-P Boilot, T Gacoin, "Optically anisotropic thin films by shear-oriented assembly of colloidal nanorods" *Adv. Mater.* 25, 3295-3300 (2013)

J Kim, A de la Cotte, R Deloncle, S Archambeau, C Biver, J-P Cano, K Lahlil, J-P Boilot, E Grelet, T Gacoin, "$LaPO_4$ mineral liquid crystalline suspensions with outstanding colloidal stability for electro-optical applications" *Adv. Funct. Mater.* 22, 4949–4956 (2012)

Oral presentations

J Kim, J Peretti, K Lahlil, J-P Boilot, T Gacoin, "Large area directed assembly of colloidal nanorods into optically anisotropic thin films" *MRS Spring Meeting San Francisco March 2013*

J Kim, J Peretti, K Lahlil, J-P Boilot, T Gacoin, "Inorganic thin film waveplates by shear-directed assembly of colloidal nanorods" *MRS Spring Meeting San Francisco March 2013*

J Kim, A de la Cotte, R Deloncle, S Archambeau, C Biver, J-P Cano, K Lahlil, J-P Boilot, E Grelet, T Gacoin, "Liquid crystalline behaviour of colloidal $LaPO_4$ nanorod suspensions" *ACS Fall Meeting Philadelphia August 2012*

Patent

(2012D10002 FR 1257185) "Procédé de fabrication d'une couche mince solide minérale transparente et biréfringente et composant optique à couche mince solide minérale transparente et biréfringente"

Appendix

A.1. Polarization optical microscope set-up

In most cases, the bulk nanorods samples were observed using the polarization optical microscope system shown in the figure below. The simultaneous measurement of the birefringence and the polarized photoluminescence was enabled by using a modified geometry of the commercial optical microscope system (Olympus BX51WI). For the birefringence measurement, the diascopic illumination light propagates through the polarizer – sample – objective – Berek compensator – analyzer in order, and is then captured by the CCD camera (DTA 1600A). For the polarized photoluminescence measurement, the excitation light from the LED (SMB1W-395nm) illuminator is guided toward the sample through the episcopic pathway with a dichroic mirror. Then, the emission light from the sample propagating through the dichroic mirror (>460nm) and the analyzer is reflected by a beam splitter and collected by an optical fiber into the liquid nitrogen cooled spectrometer (ARS SpectraPro 300i). The oscilloscope and the voltage amplifier connected to a function generator are also shown. A more detailed anatomy of the same microscope system is demonstrated at *http://www.olympusmicro.com/primer/techniques/fluorescence/bx51fluorescence.html*.
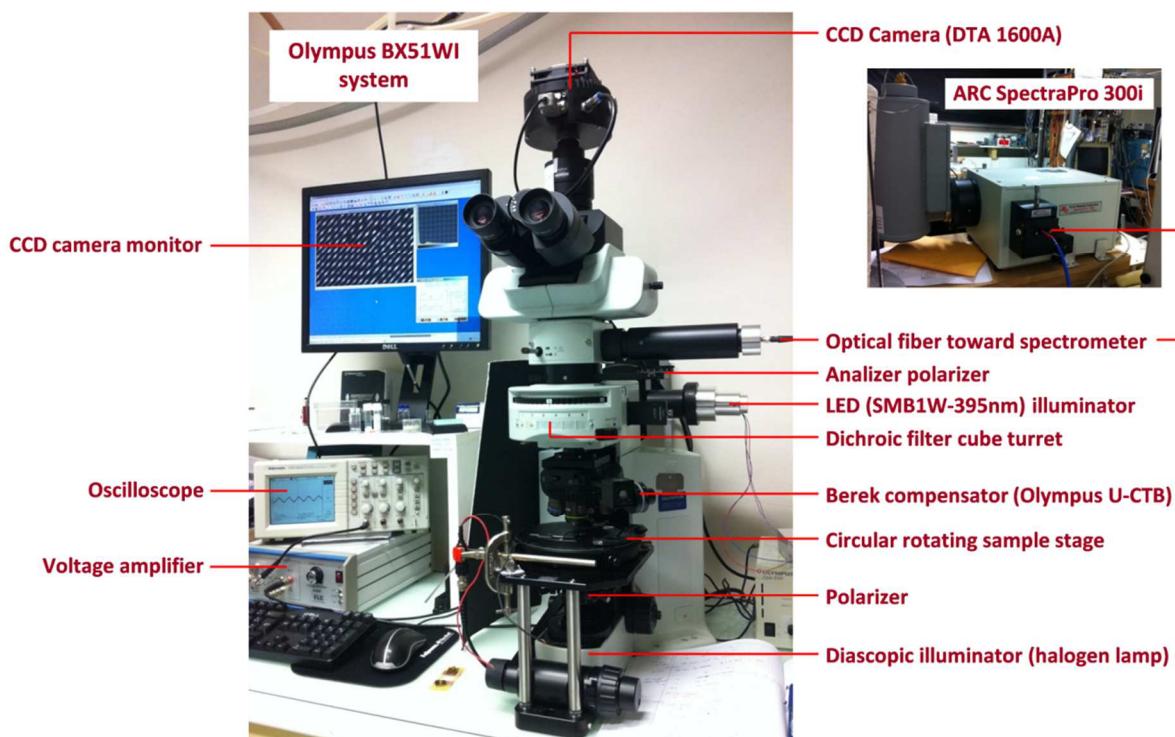
A.2. Berek compensator

The Berek compensator is an optical device that is capable of quantitatively determining the wavelength retardation of a birefringent material. Provided the thickness of the sample can be measured, a Berek compensator can be utilized to ascertain the birefringence value. The compensator operates by measuring the rotation angle of a calcite or magnesium fluoride optical plate cut perpendicular to the optical microscope axis.
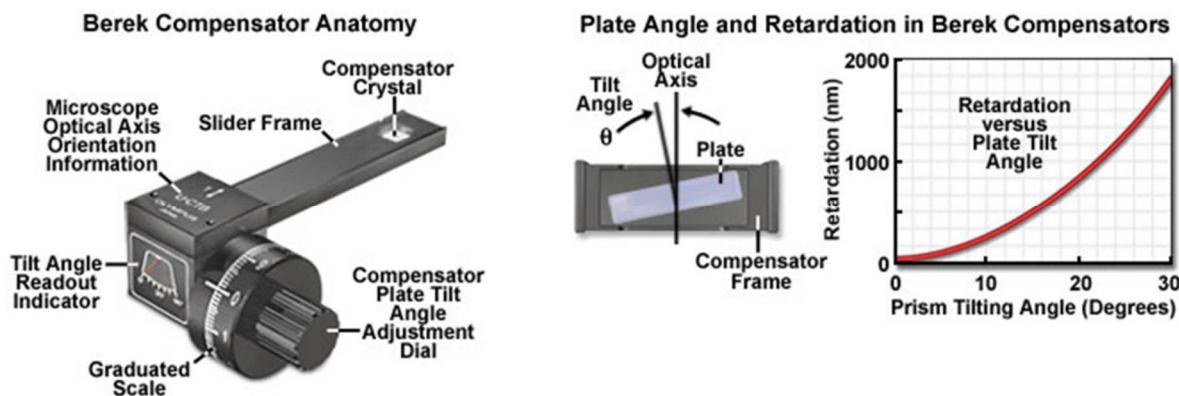

In a Berek compensator adjusted for zero retardation, the single birefringent uniaxial crystalline plate is oriented with the extraordinary optical axis perpendicular to the surface of the crystal and parallel to the microscope optical axis. Polarized light passing through the specimen encounters the compensator at normal incidence (zero degrees) and propagates through the compensator with a velocity that is independent upon the direction of polarization. As the compensator plate tilt adjustment dial is rotated with respect to the direction of incident polarized light (and microscope optical axis), the incident plane coincides with the refractive index plane of the extraordinary axis and alters the velocity of light passing through the crystal. In general, the polarized wavefront is retarded by a measurable quantity that is dependent upon the angle of tilt and the wavelength of illumination. Simultaneously, light polarized perpendicular to the incident plane continues to propagate through the compensator plate along the ordinary axis and with a velocity that remains independent upon the tilt angle. As a net result, polarized light exiting the specimen and passing through a tilted Berek compensator is retarded by an additional amount by the compensator and accumulates a relative phase shift (dependent upon the tilt angle), which can be measured with the device. The degree of optical path difference introduced by a Berek compensator is determined by the thickness of the birefringent plate, the wavelength of illumination, the refractive index difference between the ordinary and extraordinary axes of the compensator crystal, and the tilt angle. Most manufacturers compound all of these quantities into a constant that is utilized to calibrate the retardation vernier scale.

※ The above information was taken from:

   http://www.olympusmicro.com/primer/techniques/polarized/berekcompensator.html

A.3. Laser scanning confocal microscopy set-up

As noted in the section 4.3.2 the polarized photoluminescence emission measurement of single nanorods was conducted by using a laser scanning confocal microscope at Van't Hoff institute for molecular sciences – Amsterdam university. The schematic figure below represents the arrangement of the system. It is basically composed of three parts: a microscope, an excitation laser light source, and a confocal box equipped with detectors. The microscope is an inverted type (Olympus IX71) equipped with an oil immersion, 100x, 1.4 NA objective (UPlanSApo), mounted on a piezo-scanning stage (Physik Instrument GmbH). The excitation light source is Ti:Sapphire laser (Chameleon ULTRA-2, Coherent). Combination of the laser with a second harmonic generator (SHG) enables to modify the original laser light (tuned at 788nm) to a 394nm laser light for an efficient excitation of Eu:LaPO$_4$ crystalline nanorods. The emission light filtered by a polarizer is detected by both a single photon avalanche diodes (SPAD) and a peltier-cooled spectrometer (ARC SpectrPro 150) inside the confocal box.
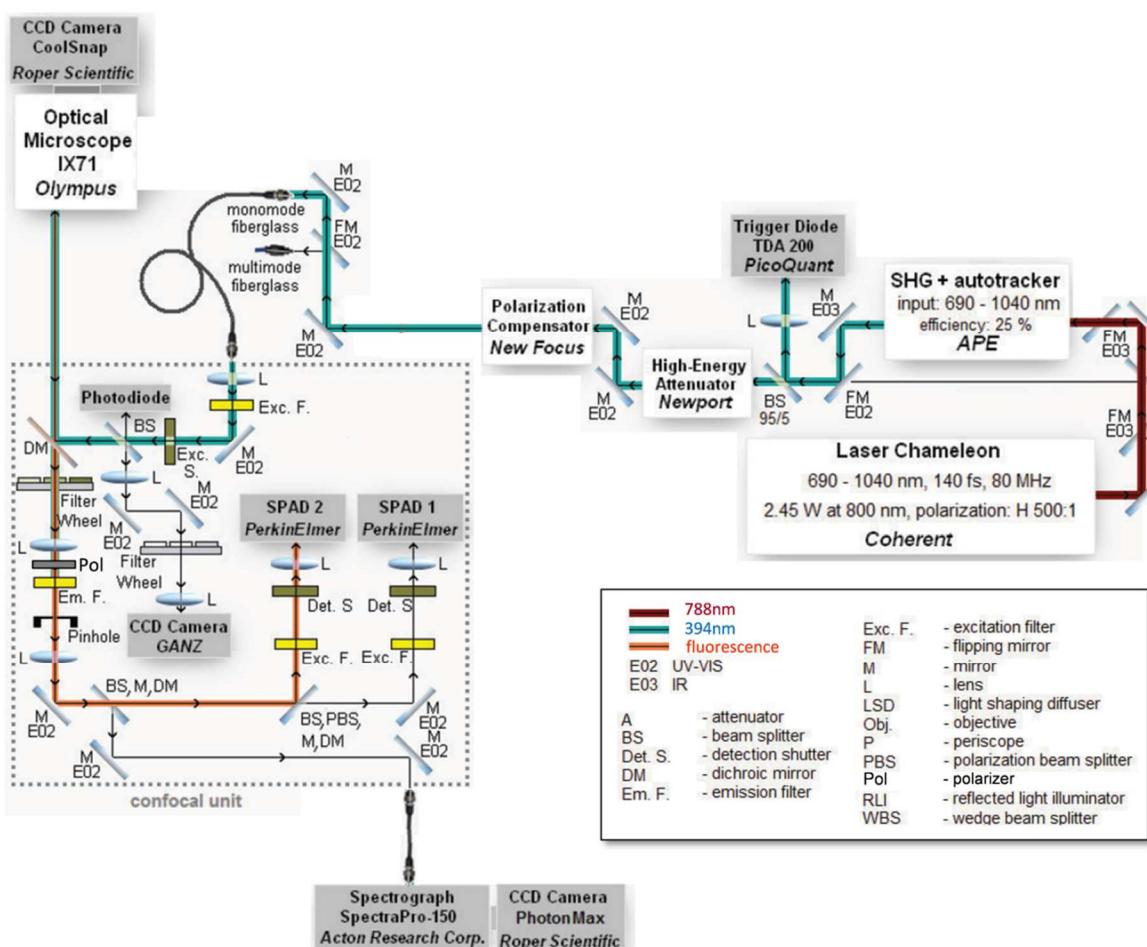
※ The above information was taken and modified from the thesis of Joanna Sierkierzycka, a previous PhD student of Prof. Fred Brouwer.

References

[1]   H. Zocher, *Zeitschrift für anorganische und allgemeine Chemie* **1925**, *147*, 91-110.
[2]   L. Onsager, *Annals of the New York Academy of Sciences* **1949**, *51*, 627-659.
[3]   J. C. P. Gabriel, P. Davidson, in *Colloid Chemistry 1, Vol. 226*, Springer-Verlag Berlin, Berlin, **2003**, pp. 119-172.
[4]   P. Davidson, J.-C. P. Gabriel, *Current Opinion in Colloid & Interface Science* **2005**, *9*, 377-383.
[5]   A. Dessombz, D. Chiche, P. Davidson, P. Panine, C. Chanéac, J.-P. Jolivet, *Journal of the American Chemical Society* **2007**, *129*, 5904-5909.
[6]   A. Dessombz, C. R. Pasquier, P. Davidson, C. Chanèac, *The Journal of Physical Chemistry C* **2010**, *114*, 19799-19802.
[7]   P. A. Buining, H. N. W. Lekkerkerker, *The Journal of Physical Chemistry* **1993**, *97*, 11510-11516.
[8]   M. P. B. van Bruggen, H. N. W. Lekkerkerker, *Langmuir* **2002**, *18*, 7141-7145.
[9]   B. J. Lemaire, P. Davidson, Ferr, eacute, J., J. P. Jamet, P. Panine, I. Dozov, J. P. Jolivet, *Physical Review Letters* **2002**, *88*, 125507.
[10]   B. J. Lemaire, P. Davidson, J. Ferré, J. P. Jamet, D. Petermann, P. Panine, I. Dozov, J. P. Jolivet, *The European Physical Journal E: Soft Matter and Biological Physics* **2004**, *13*, 291-308.
[11]   B. J. Lemaire, P. Davidson, P. Panine, J. P. Jolivet, *Physical Review Letters* **2004**, *93*, 267801.
[12]   G. Vroege, D. Thies-Weesie, A. Petukhov, B. Lemaire, P. Davidson, *Advanced Materials* **2006**, *18*, 2565-2568.
[13]   L.-s. Li, J. Walda, L. Manna, A. P. Alivisatos, *Nano Letters* **2002**, *2*, 557-560.
[14]   L. S. Li, A. Alivisatos, *Advanced Materials* **2003**, *15*, 408-411.
[15]   L.-s. Li, M. Marjanska, G. H. J. Park, A. Pines, A. P. Alivisatos, *The Journal of Chemical Physics* **2004**, *120*, 1149-1152.
[16]   D. v. d. Beek, H. N. W. Lekkerkerker, *EPL (Europhysics Letters)* **2003**, *61*, 702.
[17]   M. C. D. Mourad, J. Wijnhoven, D. D. Van 'T Zand, D. Van der Beek, H. N. W. Lekkerkerker, *Philos. Trans. R. Soc. A-Math. Phys. Eng. Sci.* **2006**, *364*, 2807-2816.
[18]   A. A. Verhoeff, R. P. Brand, H. N. W. Lekkerkerker, *Mol. Phys.* **2011**, *109*, 1363-1371.
[19]   S. Abend, G. Lagaly, *Applied Clay Science* **2000**, *16*, 201-227.
[20]   J.-C. P. Gabriel, C. Sanchez, P. Davidson, *The Journal of Physical Chemistry* **1996**, *100*, 11139-11143.
[21]   P. C. Hiemenz, *Journal of Chemical Education* **1972**, *49*, 164-170.
[22]   Z. Emanuela, *Journal of Physics: Condensed Matter* **2007**, *19*, 323101.
[23]   M. Y. Lin, H. M. Lindsay, D. A. Weitz, R. C. Ball, R. Klein, P. Meakin, *Nature* **1989**, *339*, 360-362.
[24]   A. Mohraz, D. B. Moler, R. M. Ziff, M. J. Solomon, *Physical Review Letters* **2004**, *92*, 155503.
[25]   M. J. Solomon, P. T. Spicer, *Soft Matter* **2010**, *6*, 1391-1400.
[26]   A. P. Philipse, *Langmuir* **1996**, *12*, 1127-1133.
[27]   A. P. Philipse, A. M. Wierenga, *Langmuir* **1998**, *14*, 49-54.
[28]   P. Davidson, *Comptes Rendus Chimie* **2009**, *13*, 142-153.
[29]   F. Camerel, J. C. P. Gabriel, P. Batail, P. Panine, P. Davidson, *Langmuir* **2003**, *19*, 10028-10035.
[30]   R. H. Somani, B. S. Hsiao, A. Nogales, S. Srinivas, A. H. Tsou, I. Sics, F. J. Balta-Calleja, T. A. Ezquerra, *Macromolecules* **2000**, *33*, 9385-9394.
[31]   P. D. Cozzoli, A. Kornowski, H. Weller, *Journal of the American Chemical Society* **2003**, *125*, 14539-14548.
[32]   J. Joo, S. G. Kwon, T. Yu, M. Cho, J. Lee, J. Yoon, T. Hyeon, *The Journal of Physical Chemistry B* **2005**, *109*, 15297-15302.
[33]   B. Koo, J. Park, Y. Kim, S.-H. Choi, Y.-E. Sung, T. Hyeon, *The Journal of Physical Chemistry B* **2006**, *110*, 24318-24323.

[34]   A. P. Alivisatos, *Science* **1996**, *271*, 933-937.

[35]   R. Hikmet, P. Chin, D. Talapin, H. Weller, *Advanced Materials* **2005**, *17*, 1436-1439.

[36]   G. Oster, *Journal of general Physiology* **1950**, *33*, 445-473.

[37]   J. D. Bernal, I. Fankuchen, *The Journal of General Physiology* **1941**, *25*, 111-146.

[38]   X. Wen, R. B. Meyer, D. L. D. Caspar, *Physical Review Letters* **1989**, *63*, 2760.

[39]   J. C. P. Gabriel, P. Davidson, *Advanced Materials* **2000**, *12*, 9-20.

[40]   P. Davidson, P. Batail, J. C. P. Gabriel, J. Livage, C. Sanchez, C. Bourgaux, *Progress in Polymer Science* **1997**, *22*, 913-936.

[41]   L. J. Michot, I. Bihannic, S. Maddi, S. r. S. Funari, C. Baravian, P. Levitz, P. Davidson, *Proceedings of the National Academy of Sciences* **2006**, *103*, 16101-16104.

[42]   M. C. D. Mourad, D. V. Byelov, A. V. Petukhov, D. A. Matthijs de Winter, A. J. Verkleij, H. N. W. Lekkerkerker, *The Journal of Physical Chemistry B* **2009**, *113*, 11604-11613.

[43]   F. M. van der Kooij, K. Kassapidou, H. N. W. Lekkerkerker, *Nature* **2000**, *406*, 868-871.

[44]   D. M. E. Thies-Weesie, J. P. de Hoog, M. H. Hernandez Mendiola, A. V. Petukhov, G. J. Vroege, *Chemistry of Materials* **2007**, *19*, 5538-5546.

[45]   P. A. Buining, A. P. Philipse, H. N. W. Lekkerkerker, *Langmuir* **1994**, *10*, 2106-2114.

[46]   S. C. Shen, Q. Chen, P. S. Chow, G. H. Tan, X. T. Zeng, Z. Wang, R. B. H. Tan, *The Journal of Physical Chemistry C* **2006**, *111*, 700-707.

[47]   A. Wierenga, A. P. Philipse, H. N. W. Lekkerkerker, D. V. Boger, *Langmuir* **1998**, *14*, 55-65.

[48]   M. N. Tahir, P. Theato, P. Oberle, G. Melnyk, S. Faiss, U. Kolb, A. Janshoff, M. Stepputat, W. Tremel, *Langmuir* **2006**, *22*, 5209-5212.

[49]   M. B. Sigman, B. A. Korgel, *Journal of the American Chemical Society* **2005**, *127*, 10089-10095.

[50]   J. W. Anthony, *The Americal Mineralogist* **1957**, *42*, 1957.

[51]   H. Meyssamy, K. Riwotzki, A. Kornowski, S. Naused, M. Haase, *Advanced Materials* **1999**, *11*, 840-844.

[52]   G. Phaomei, R. S. Ningthoujam, W. R. Singh, N. S. Singh, M. N. Luwang, R. Tewari, R. K. Vatsa, *Optical Materials*, *32*, 616-622.

[53]   Y.-P. Fang, A.-W. Xu, R.-Q. Song, H.-X. Zhang, L.-P. You, J. C. Yu, H.-Q. Liu, *Journal of the American Chemical Society* **2003**, *125*, 16025-16034.

[54]   V. Buissette, D. Giaume, T. Gacoin, J.-P. Boilot, *Journal of Materials Chemistry* **2006**, *16*, 529-539.

[55]   W. Bu, L. Zhang, Z. Hua, H. Chen, J. Shi, *Crystal Growth & Design* **2007**, *7*, 2305-2309.

[56]   X. Wang, M. Gao, *Journal of Materials Chemistry* **2006**, *16*, 1360-1365.

[57]   Z. A. Peng, X. Peng, *Journal of the American Chemical Society* **2001**, *123*, 1389-1395.

[58]   S. H. Yu, B. Liu, M. S. Mo, J. H. Huang, X. M. Liu, Y. T. Qian, *Advanced Functional Materials* **2003**, *13*, 639-647.

[59]   M.-G. Ma, J.-F. Zhu, S.-W. Cao, F. Chen, R.-C. Sun, *Journal of Alloys and Compounds* **2010**, *492*, 559-563.

[60]   M. Yang, H. You, G. Jia, Y. Huang, Y. Song, Y. Zheng, K. Liu, L. Zhang, *Journal of Crystal Growth* **2009**, *311*, 4753-4758.

[61]   A. Mohraz, M. J. Solomon, *Journal of Colloid and Interface Science* **2006**, *300*, 155-162.

[62]   S. Meuer, P. Oberle, P. Theato, W. Tremel, R. Zentel, *Advanced Materials* **2007**, *19*, 2073-2078.

[63]   P. Yang, Z. Quan, C. Li, Z. Hou, W. Wang, J. Lin, *Journal of Solid State Chemistry* **2009**, *182*, 1045-1054.

[64]   A. Mpandou, B. Siffert, *Colloids and Surfaces* **1987**, *24*, 159-172.

[65]   G. J. Vroege, H. N. W. Lekkerkerker, *Rep. Prog. Phys.* **1992**, *55*, 1241-1309.

[66]   Z. X. Zhang, J. S. van Duijneveldt, *J. Chem. Phys.* **2006**, *124*, 7.

[67]   E. Grelet, *Physical Review Letters* **2008**, *100*, 168301.

[68]   I. Dozov, E. Paineau, P. Davidson, K. Antonova, C. Baravian, I. Bihannic, L. J. Michot, *The Journal of Physical Chemistry B* **2011**, *115*, 7751-7765.

[69]   P. Weinberger, *Philosophical Magazine Letters* **2008**, *88*, 897-907.

127

[70]   S.-W. Choi, S.-I. Yamamoto, Y. Haseba, H. Higuchi, H. Kikuchi, *Applied Physics Letters* **2008**, *92*, 043119-043113.

[71]   D. A. Dunmur, A. E. Tomes, *Molecular Crystals and Liquid Crystals* **1981**, *76*, 231-240.

[72]   L. Rao, Z. Ge, S. Gauza, K.-M. Chen, S.-T. Wu, *Molecular Crystals and Liquid Crystals* **2010**, *527*, 30/[186]-142/[198].

[73]   J. Yan, H.-C. Cheng, S. Gauza, Y. Li, M. Jiao, L. Rao, S.-T. Wu, *Applied Physics Letters* **2010**, *96*, 071105-071103.

[74]   K. Hongladarom, W. R. Burghardt, S. G. Baek, S. Cementwala, J. J. Magda, *Macromolecules* **1993**, *26*, 772-784.

[75]   S. Chandrasekhar, N. V. Madhusudana, *J. Phys. Colloques* **1969**, *30*, C4-24-C24-27.

[76]   A. M. Taylor, *Transactions of the Faraday Society* **1936**, *32*, 307-310.

[77]   W. Philippoff, *Nature* **1956**, *178*, 811-812.

[78]   B. D. Wall, S. R. Diegelmann, S. Zhang, T. J. Dawidczyk, W. L. Wilson, H. E. Katz, H.-Q. Mao, J. D. Tovar, *Advanced Materials* **2011**, *23*, 5009-5014.

[79]   B. Sun, H. Sirringhaus, *Journal of the American Chemical Society* **2006**, *128*, 16231-16237.

[80]   M. Mittal, R. K. Niles, E. M. Furst, *Nanoscale* **2010**, *2*, 2237-2243.

[81]   S. Zhang, P. W. Majewski, G. Keskar, L. D. Pfefferle, C. O. Osuji, *Langmuir* **2011**, *27*, 11616-11621.

[82]   Y. Takeuchi, F. Yamamoto, S. Yamakawa, *Polym. J.* **1984**, *16*, 579-582.

[83]   G. Schmidt, S. Müller, P. Lindner, C. Schmidt, W. Richtering, *The Journal of Physical Chemistry B* **1998**, *102*, 507-513.

[84]   H. Siebert, I. Quijada-Garrido, J. Vermant, L. Noirez, W. R. Burghardt, C. Schmidt, *Macromolecular Chemistry and Physics* **2007**, *208*, 2161-2172.

[85]   G. Marrucci, P. L. Maffettone, *Macromolecules* **1989**, *22*, 4076-4082.

[86]   G. Marrucci, *Macromolecules* **1991**, *24*, 4176-4182.

[87]   W. R. Burghardt, *Macromolecular Chemistry and Physics* **1998**, *199*, 471-488.

[88]   R. G. Larson, D. W. Mead, *Liquid Crystals* **1992**, *12*, 751-768.

[89]   J. A. Müller, R. S. Stein, H. H. Winter, *Rheologica Acta* **1996**, *35*, 160-167.

[90]   M. P. Lettinga, Z. Dogic, H. Wang, J. Vermant, *Langmuir* **2005**, *21*, 8048-8057.

[91]   M. Ripoll, P. Holmqvist, R. G. Winkler, G. Gompper, J. K. G. Dhont, M. P. Lettinga, *Physical Review Letters* **2008**, *101*, 168302.

[92]   H. A. Barnes, *Journal of Non-Newtonian Fluid Mechanics* **1997**, *70*, 1-33.

[93]   S. Abend, G. Lagaly, *Applied Clay Science* **2000**, *16*, 201-227.

[94]   G. Gorachand, *Optics Communications* **1999**, *163*, 95-102.

[95]   H. Kikuta, Y. Ohira, K. Iwata, *Appl. Opt.* **1997**, *36*, 1566-1572.

[96]   F. Xu, R. C. Tyan, P. C. Sun, Y. Fainman, C. C. Cheng, A. Scherer, *Opt. Lett.* **1995**, *20*, 2457-2459.

[97]   H. Kikuta, H. Toyota, W. Yu, *Optical Review* **2003**, *10*, 63-73.

[98]   T. Motohiro, Y. Taga, *Appl. Opt.* **1989**, *28*, 2466-2482.

[99]   O. L. Muskens, S. L. Diedenhofen, M. H. M. van Weert, M. T. Borgström, E. P. A. M. Bakkers, J. G. Rivas, *Advanced Functional Materials* **2008**, *18*, 1039-1046.

[100]   I. Hodgkinson, Q. h. Wu, *Appl. Opt.* **1999**, *38*, 3621-3625.

[101]   A. C. van Popta, J. Cheng, J. C. Sit, M. J. Brett, *Journal of Applied Physics* **2007**, *102*, 013517-013517.

[102]   H. Miyata, Y. Kawashima, M. Itoh, M. Watanabe, *Chemistry of Materials* **2005**, *17*, 5323-5327.

[103]   H. Miyata, Y. Fukushima, K. Okamoto, M. Takahashi, M. Watanabe, W. Kubo, A. Komoto, S. Kitamura, Y. Kanno, K. Kuroda, *Journal of the American Chemical Society*, *133*, 13539-13544.

[104]   O. Wiener, *Abh. Sachs. Ges. Wiss* **1912**, *32*, 509.

[105]   W. L. Bragg, A. B. Pippard, *Acta Crystallographica* **1953**, *6*, 865-867.

[106]   E. W. Taylor, W. Cramer, *Biophysical Journal* **1963**, *3*, 143-154.

[107]   R. Oldenbourg, T. Ruiz, *Biophysical Journal* **1989**, *56*, 195-205.

[108]   V. Twersky, *J. Opt. Soc. Am.* **1975**, *65*, 239-245.

[109]   E. C. Stoner, *Philosophical Magazine Series 7* **1945**, *36*, 803-821.

[110] E. M. L. L. D. Landau, and L. P. Pitaevskii *Electrodynamics of Continuous Media* Pergamon Oxford, **1984**.

[111] P. H. nninen, T. Ala-Kleme, H. Hèarmèa, *Lanthanide Luminescence: Photophysical, Analytical and Biological Aspects*, Springer Berlin Heidelberg, **2011**.

[112] M. Haase, K. Riwotzki, H. Meyssamy, A. Kornowski, *Journal of Alloys and Compounds* **2000**, *303–304*, 191-197.

[113] K. Kömpe, H. Borchert, J. Storz, A. Lobo, S. Adam, T. Möller, M. Haase, *Angewandte Chemie International Edition* **2003**, *42*, 5513-5516.

[114] L. Yu, H. Song, S. Lu, Z. Liu, L. Yang, X. Kong, *The Journal of Physical Chemistry B* **2004**, *108*, 16697-16702.

[115] S. S. Brown, H.-J. Im, A. J. Rondinone, S. Dai, *Journal of Colloid and Interface Science* **2005**, *292*, 127-132.

[116] Z. Huo, C. Chen, D. Chu, H. Li, Y. Li, *Chemistry – A European Journal* **2007**, *13*, 7708-7714.

[117] Z. Fu, W. Bu, *Solid State Sciences* **2008**, *10*, 1062-1067.

[118] Y. Zhang, H. Guan, *Materials Research Bulletin* **2005**, *40*, 1536-1543.

[119] J. A. Diaz-GuillÃ©n, A. F. Fuentes, S. Gallini, M. T. Colomer, *Journal of Alloys and Compounds* **2007**, *427*, 87-93.

[120] K. G.-W. Binnemans, C., *Journal of rare earths* **1996**, *14*, 173-180.

[121] J. Dexpert-Ghys, R. Mauricot, M. D. Faucher, *Journal of Luminescence* **1996**, *69*, 203-215.

[122] R. Y. Wang, *Journal of Luminescence* **2004**, *106*, 211-217.

[123] C. Brecher, H. Samelson, A. Lempicki, R. Riley, T. Peters, *Physical Review* **1967**, *155*, 178.

[124] C. Gorller-Walrand, I. Hendrickx, L. Fluyt, M. P. Gos, J. D'Olieslager, G. Blasse, *The Journal of Chemical Physics* **1992**, *96*, 5650-5658.

[125] Y. G. Galyametdinov, A. A. Knyazev, V. I. Dzhabarov, T. Cardinaels, K. Driesen, C. Görller-Walrand, K. Binnemans, *Advanced Materials* **2008**, *20*, 252-257.

[126] K. Binnemans, *Journal of Materials Chemistry* **2009**, *19*, 448-453.

[127] K. Driesen, C. Vaes, T. Cardinaels, K. Goossens, C. Goìrller-Walrand, K. Binnemans, *The Journal of Physical Chemistry B* **2009**, *113*, 10575-10579.

[128] H. Lai, A. Bao, Y. Yang, Y. Tao, H. Yang, *Journal of Nanoparticle Research* **2008**, *10*, 1355-1360.

[129] M. Grell, D. D. C. Bradley, *Advanced Materials* **1999**, *11*, 895-905.

[130] L. L. Chapoy, D. B. DuPre, *The Journal of Chemical Physics* **1978**, *69*, 519-524.

[131] A. Montali, C. Bastiaansen, P. Smith, C. Weder, *Nature* **1998**, *392*, 261-264.

[132] Y. Yoshida, N. Tanigaki, K. Yase, S. Hotta, *Advanced Materials* **2000**, *12*, 1587-1591.

[133] C. A. Breen, T. Deng, T. Breiner, E. L. Thomas, T. M. Swager, *Journal of the American Chemical Society* **2003**, *125*, 9942-9943.

[134] J. Wang, M. S. Gudiksen, X. Duan, Y. Cui, C. M. Lieber, *Science* **2001**, *293*, 1455-1457.

[135] H. E. Ruda, A. Shik, *Physical Review B* **2005**, *72*, 115308.

[136] H.-Y. Chen, Y.-C. Yang, H.-W. Lin, S.-C. Chang, S. Gwo, *Opt. Express* **2008**, *16*, 13465-13475.

[137] R. Venugopal, P.-I. Lin, C.-C. Liu, Y.-T. Chen, *Journal of the American Chemical Society* **2005**, *127*, 11262-11268.

[138] S. Acharya, S. Kundu, J. P. Hill, G. J. Richards, K. Ariga, *Advanced Materials* **2009**, *21*, 989-993.

[139] J. Hu, L.-s. Li, W. Yang, L. Manna, L.-w. Wang, A. P. Alivisatos, *Science* **2001**, *292*, 2060-2063.

[140] T. Wang, J. Zhuang, J. Lynch, O. Chen, Z. Wang, X. Wang, D. LaMontagne, H. Wu, Z. Wang, Y. C. Cao, *Science* **2012**, *338*, 358-363.

[141] L. L. Chapoy, D. B. DuPre, *The Journal of Chemical Physics* **1979**, *70*, 2550-2553.

[142] A. Szabo, *The Journal of Chemical Physics* **1980**, *72*, 4620-4626.

[143] H. Yoshida, S. Kobinata, S. Maeda, *Molecular Crystals and Liquid Crystals* **1985**, *131*, 209-216.

[144] E. Wolarz, D. Bauman, *Molecular Crystals and Liquid Crystals* **1991**, *197*, 1-13.

[145] V. S. Ratchkevitch, S. Y. Yakovenko, J. Pelzl, *Liquid Crystals* **1993**, *15*, 591-604.

[146] A. J. Bur, S. C. Roth, C. L. Thomas, *Review of Scientific Instruments* **2000**, *71*, 1516-1523.

[147] S. Brasselet, V. Le Floc'h, F. Treussart, J.-F. Roch, J. Zyss, E. Botzung-Appert, A. Ibanez, *Physical Review Letters* **2004**, *92*, 207401.

[148]   S. Brasselet, *Adv. Opt. Photon.* **2011**, *3*, 205-271.
[149]   A. Gasecka, P. Tauc, A. Lewit-Bentley, S. Brasselet, *Physical Review Letters* **2012**, *108*, 263901.
[150]   F. Munhoz, H. Rigneault, S. Brasselet, *J. Opt. Soc. Am. B* **2012**, *29*, 1541-1550.
[151]   A. Yildiz, J. N. Forkey, S. A. McKinney, T. Ha, Y. E. Goldman, P. R. Selvin, *Science* **2003**, *300*, 2061-2065.
[152]   J. N. Forkey, M. E. Quinlan, M. A. Shaw, J. E. T. Corrie, Y. E. Goldman, *Nature* **2003**, *422*, 399-404.
[153]   D. Sinton, *Microfluidics and Nanofluidics* **2004**, *1*, 2-21.
[154]   R. Lindken, M. Rossi, Gro, J. Westerweel, *Lab on a Chip* **2009**, *9*, 2551-2567.
[155]   S. Lee, S. Kim, *Microfluidics and Nanofluidics* **2009**, *6*, 577-588.
[156]   K. S. K. C. V. RAMAN, *Nature* **1927**, 726-727.
[157]   A. B. Rao, *Proc. Indian Acad. Sci. (Math. Sci.)* **1937**, *5*, 124-127.
[158]   A. S. Lodge, *Nature* **1955**, *176*, 838-839.
[159]   R. Cerf, H. A. Scheraga, *Chemical Reviews* **1952**, *51*, 185-261.
[160]   W. Philippoff, *Rheologica Acta* **1961**, *1*, 371-375.
[161]   H. A. Scheraga, J. T. Edsall, J. J. O. Gadd, *The Journal of Chemical Physics* **1951**, *19*, 1101-1108.
[162]   E. D. Alcock, C. L. Sadron, *Physics* **1935**, *6*, 92-95.
[163]   H. Pih, *Experimental Mechanics* **1980**, *20*, 437-444.
[164]   M. D. Haw, P. Navard, *Rheologica Acta* **2000**, *39*, 271-279.
[165]   K. Hongladarom, V. M. Ugaz, D. K. Cinader, W. R. Burghardt, J. P. Quintana, B. S. Hsiao, M. D. Dadmun, W. A. Hamilton, P. D. Butler, *Macromolecules* **1996**, *29*, 5346-5355.